

Towards breast cancer radiotherapy on the MRI-linac

Tristan C.F. van Heijst

Towards breast cancer radiotherapy on the MRI-linac
PhD thesis, Utrecht University, The Netherlands

© T.C.F. van Heijst, Utrecht, 2016

All rights reserved. No part of this publication may be reproduced, distributed, or transmitted in any form or by any means, including photocopying, recording, or other electronic or mechanical methods, without the prior written permission of the publisher, except in the case of brief quotations embodied in critical reviews and certain other noncommercial uses permitted by copyright law.

The research described in this thesis was performed at University Medical Center Utrecht, The Netherlands. Financial support was provided by Elekta B.V., Philips Healthcare, and Stichting Pink Ribbon.



Cover: Aurora borealis, by Christiaan van Heijst.
Photograph taken above the Arctic Ocean, north of Alaska.
Lay-out: Simon De Rudder
Printing: BOXPress, Vianen
ISBN: 978-90-393-6712-4
Copyright: IOP Publishing (chapters 2 and 3), British Institute of Radiology (chapter 4)

Towards breast cancer radiotherapy on the MRI-linac

**Naar radiotherapie van borstkanker op de MRI-versneller
(met een samenvatting in het Nederlands)**

Proefschrift

ter verkrijging van de graad van doctor aan de Universiteit Utrecht op
gezag van de rector magnificus, prof.dr. G.J. van der Zwaan, ingevolge
het besluit van het college voor promoties in het openbaar te verdedigen
op donderdag 12 januari 2017 des middags te 12.45 uur

door

Tristan Constantijn Franciscus van Heijst

geboren 23 december 1987 te Nieuwegein

Promotor: Prof.dr. J.J.W. Lagendijk

Copromotoren: Dr. B. van Asselen
Dr. H.J.G.D. van den Bongard

“Luminous beings are we. Not this crude matter.”

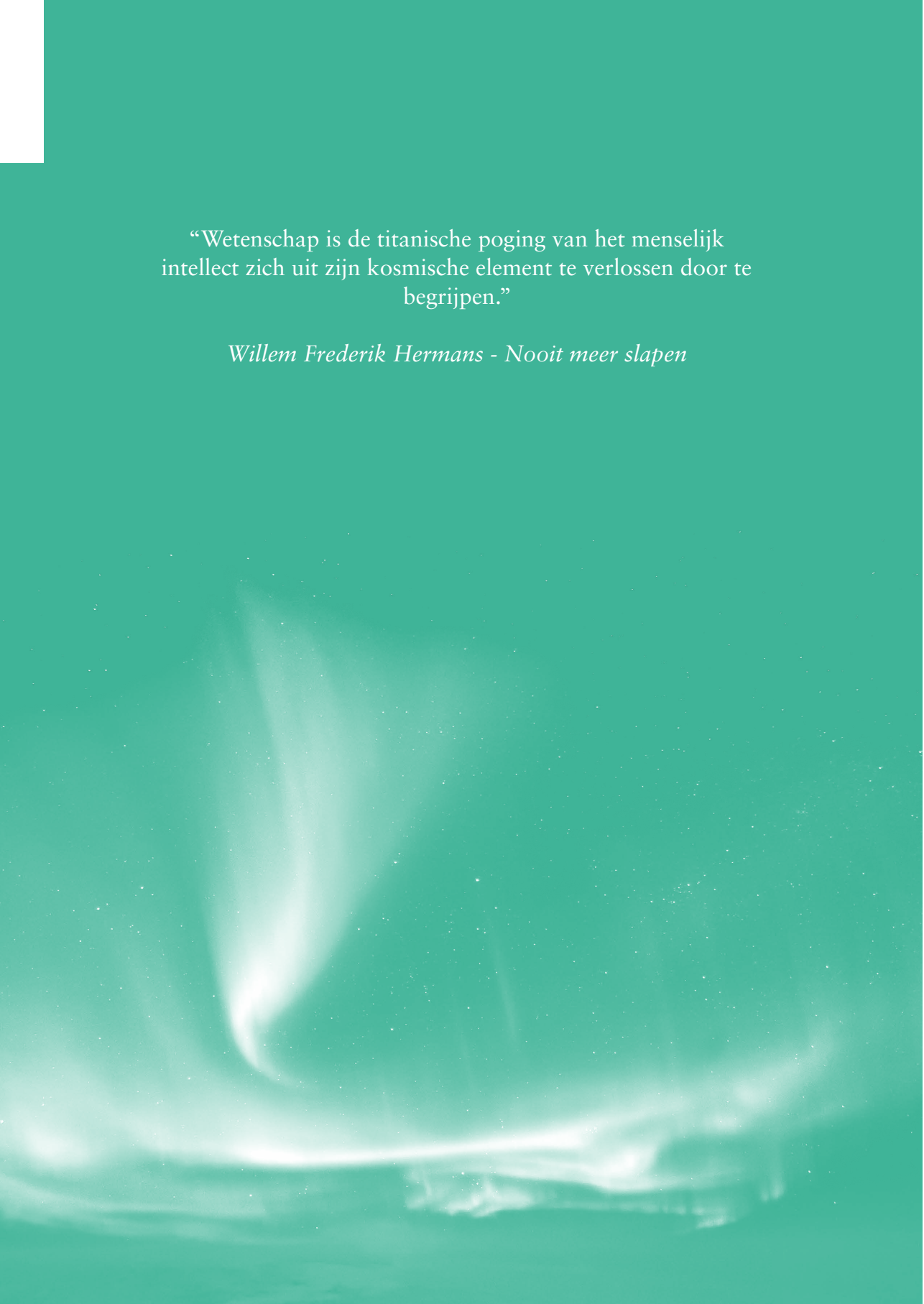
Yoda

Contents

Chapter 1	
General introduction	9
Chapter 2	
MR-guided breast radiotherapy: feasibility and magnetic-field effects on skin dose	35
Chapter 3	
Quantification of intra-fraction motion in breast radiotherapy using supine MRI	59
Chapter 4	
MRI sequences for detection of individual lymph nodes in regional breast radiotherapy planning	87
Chapter 5	
Supine MRI of individual axillary lymph nodes before and after sentinel-node biopsy	113
Chapter 6	
MRI-guided single-fraction boost delivery on individual axillary lymph nodes	135
Chapter 7	
Summary and general discussion	161
Addenda	179

“Wetenschap is de titanische poging van het menselijk
intellect zich uit zijn kosmische element te verlossen door te
begrijpen.”

Willem Frederik Hermans - Nooit meer slapen



Chapter 1

General introduction

External beam radiation therapy

Cancer treatment by radiotherapy

The goal of radiation therapy, or radiotherapy (RT), is eradication of malignant cancer cells, with a minimum amount of damage to normal tissue. Standard therapy is external-beam RT by MV photon beams on a linear accelerator (linac), delivering a specific dose to the tumour in the patient. Photons penetrate the tissue and interact in a number of processes, consisting predominantly of the photoelectric effect, Compton scattering, and electron-positron pair production [1]. These interactions can lead to damage to the DNA, which, if irreparable, leads to cell kill. While most healthy cells have mechanisms to repair certain radiation damage, recovery is often hampered in tumorous cells. Therefore, RT treatments are usually performed in a fractionated manner, which allows for normal tissue to recover in between fractions, while the tumorous tissue cannot restore in time [2]. This should ensure adequate tumour control probability (TCP), i.e. no survival of viable tumour cells after the RT treatment. Although sufficient prescription and fractionation schedules may achieve high TCP, the risk of RT-induced toxicity, i.e. side effects due to dose to normal tissue, should be minimized. An accurate definition of the target volume in relationship to surrounding healthy structures is essential [3]. However, due to the uncertainties in tumour definition and positioning in the current RT workflow, conventional fraction dose is limited. In order to achieve higher TCP, dose should be delivered to tumorous tissue more accurately, thus killing tumour cells more effectively, while sparing normal tissue. In general, a higher concentration of tumour cells requires a higher RT dose, while a lower RT dose may suffice for lower tumour cell density. Moreover, heterogeneity in the intrinsic sensitivity of tumour cells to radiation influences TCP [4]. The ideal scenario is a *dose painting by numbers* strategy, where dose is specifically tailored for regions of tissue with various tumour cell concentrations.

Current radiotherapy practice

In preparation for RT, the patient is scanned by computed tomography (CT) in treatment position. For the definition of the target and surrounding structures, other imaging modalities are commonly used and co-registered

with CT. These can include positron emission tomography (PET), and magnetic resonance imaging (MRI) scans. The radiation oncologist delineates target volumes and organs-at-risk (OARs) on the planning CT scan [3]. The macroscopically visible gross tumour volume (GTV) is defined first, which is expanded to create the clinical target volume (CTV). The CTV extension ensures inclusion of microscopic invasion. The GTV-CTV definition can be viewed as a first approximation to a *dose painted* scenario, where dose to the CTV is lower than to the GTV, due to lower concentration of tumour cells.

During delivery of dose, geometric inaccuracies and uncertainties can lead to both systematic and random errors [5]. In order to account for these, the CTV is extended by another margin to create the planning target volume (PTV). The choice of the CTV-PTV margin is dependent on tumour site, motion during RT treatment, motion between fractions, and positioning uncertainties. Some of these uncertainties can be reduced by use of fixation methods.

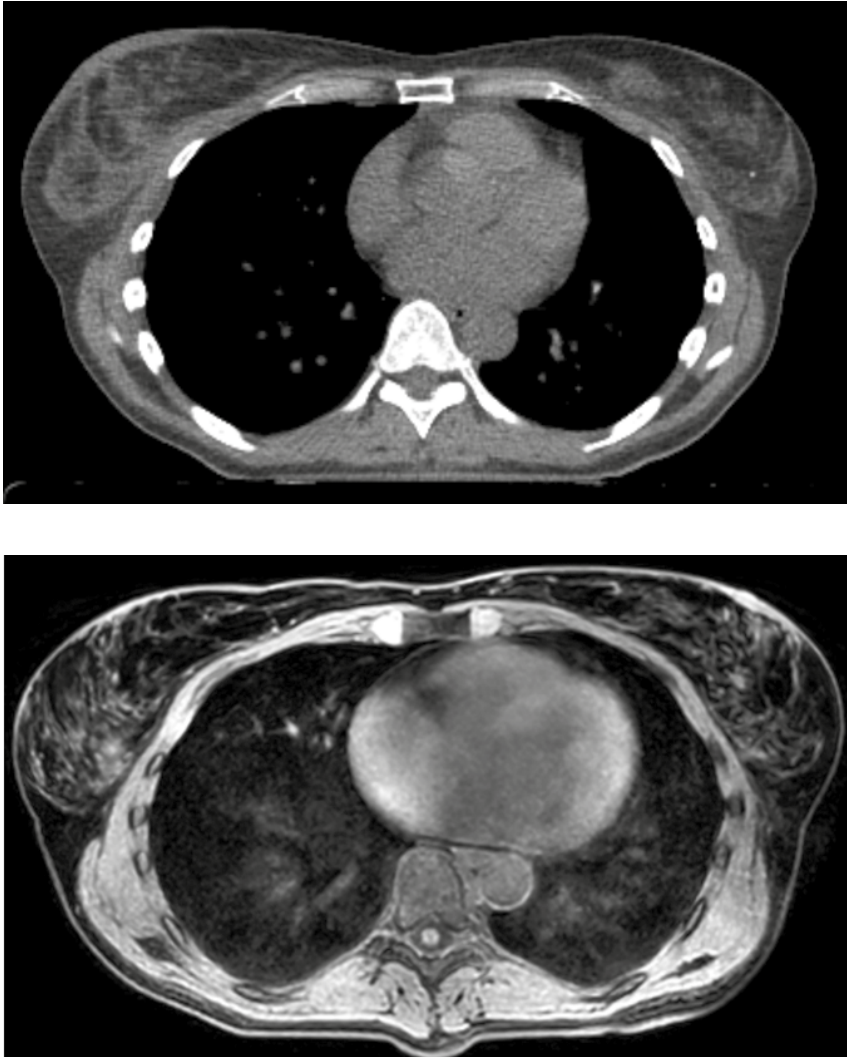
After contouring, an RT treatment plan is generated and simulated based on the volumes as delineated on the CT. The RT plan is optimized to make sure the desired dose is delivered to the target volumes, while dose to OARs is within clinical tolerances. The optimized treatment plan is transferred to be delivered on the linac. In clinical practice, the patient is positioned based on skin markers before each fraction such that the anatomy on the planning CT scan is imitated as best as possible. The position is then verified with on-line imaging methods, such as electronic portal imaging (EPID) and cone-beam CT (CBCT).

Towards dose differentiation

Target volumes are expanded by margins to account for uncertainties and geometrical inaccuracies in current RT practice. If these uncertainties could be reduced, this enables a reduction of margins [6]. As a consequence, the dose to normal tissue is decreased, while the fraction dose to the tumour could be increased. Moreover, with a more accurate definition of tumorous and normal tissue than currently achievable, target volumes may be reduced, and therefore the total treated volume is smaller. Additionally, functional information on higher and lower tumour cell concentrations in the target could enable a dose differentiated RT prescription. These aspects are crucial towards more advanced RT strategies, with potentially higher TCP and lower RT-induced toxicity. Due to the many possibilities it has to offer, MRI plays an important role in this development.

Magnetic resonance imaging

In current RT planning, a major drawback is poor contrast of soft tissues on CT. For better target definition, MRI, having superior soft-tissue contrast, is increasingly used to aid in the delineation process (figure 1). MRI is a versatile modality that uses magnetic fields and radiofrequency pulses to form images of the patient anatomy. By manipulation of the many imaging parameters, MRI can provide a multitude of contrasts that reflect various endogenous tissue characteristics. It can be performed to acquire 3-dimensional (3D) and 2D scans, in arbitrary orientations, and can provide both anatomical and functional information. Furthermore, in contrast to CT, MRI does not require ionizing radiation, which facilitates its repeated use without radiation safety concerns. The added value of various MRI techniques in RT planning has been extensively demonstrated for a wide range of tumour sites [7–16]. For example, for gynaecological, rectal, and prostate tumours, it has been demonstrated that MRI-based GTV delineations are smaller than on CT [7,17–20].



● *Figure 1 Transverse images acquired by CT (top) and MRI (bottom), in the same breast-cancer patient. Scanning was performed in supine treatment position. MRI has superior soft-tissue contrast compared to CT.*

The MRI-linac: on-line MRI-guided radiotherapy

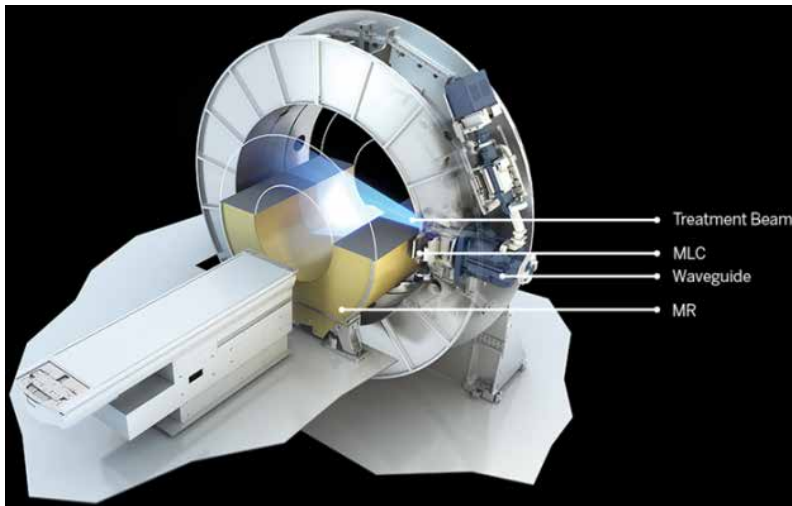
Several MRI/RT hybrid modalities are in development that enable *on-line* MRI acquisition, i.e. while the patient is on the table [21–24]. One such design is the MRI-linac (MRL), developed at the Department of Radiation Oncology in University Medical Center (UMC) Utrecht, The Netherlands, in collaboration with Elekta and Philips. The MRL combines a fully integrated 1.5 T MRI scanner (Philips, Best, The Netherlands) with a 7 MV photon linac (Elekta AB, Stockholm, Sweden), which is mounted on a ring-shaped gantry (figure 2) [21,25,26].

The MRL offers on-line diagnostic quality MRI acquisition, providing functional and anatomical information, with superior soft-tissue contrast to CT. Since the RT-planning CT is acquired before start of the irradiation, it essentially serves as a snapshot of the anatomy. Meanwhile, the anatomy can change, both before start, and during RT treatment. On conventional linacs, invasive marker-based methods are used for position verification with EPID or CBCT, but these have limited soft-tissue contrast and are unable to handle anatomical deformations. With on-line MRI guidance, newly updated anatomical information is readily available, in high spatial resolution, without the need for invasive markers. On the MRL, updated target definition in relation to the surrounding anatomical structures can therefore lead to reduction in uncertainty margins.

Another advantage of MRI guidance is the possibility to acquire MRI in high temporal resolution [27–31]. Using fast imaging, the MRL can provide direct feedback for the RT treatment, *while* the RT delivery beam is on. Real-time information on anatomical position and motion can be used to adjust the beam delivery accordingly, for example by gating or tracking. With gating, the radiation beam is switched off as soon as the target moves out of a predefined window [32,33]. During tracking, the beam shape is changed according to the tumour motion that is detected in a fast feedback loop [34–36].

Compared to a pre-beam target definition, a dynamic target definition can minimize the impact of motion during RT delivery, leading to higher

precision. Relative to CT-based approaches, MRI guidance may enable decreased PTV margins resulting in new RT approaches, with dose escalation to the tumour cells and lowering dose to normal tissue. This may result in higher TCP and decreased RT-induced toxicity. RT on the MRL is under investigation for a wide number tumour sites, including spinal bone metastasis, pancreas, rectum, prostate, kidney, lung, and breast. Treatment in the MRL of patients diagnosed with breast cancer is the focus of this thesis.

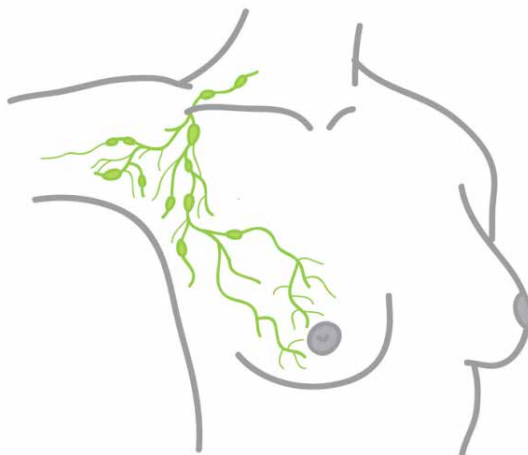


● *Figure 2 Schematic design of the MRL (top), and the actual MRL constructed at UMC Utrecht (bottom). The MRL integrates a 1.5 T MRI scanner and a 7 MV photon linac, which is mounted on a ring-shaped rotating gantry.*

Breast radiotherapy

Breast cancer is the most common type of malignancy among women in the developed world. In the Netherlands, approximately one in eight women are diagnosed with breast cancer at some point during their life [37]. Since the introduction of screening programs, the majority of breast-cancer patients are diagnosed with early-stage breast cancer and/or ductal carcinoma *in situ* (DCIS – pre-stage of breast cancer) [38,39]. Most patients are treated locally, i.e. on the ipsilateral breast, with or without adjuvant systemic therapy. Local treatment consists of surgery, i.e. excision of the tumour with a margin (lumpectomy) or whole breast (mastectomy), usually followed by RT [40].

Breast-cancer cells can metastasize to regional lymph nodes (LNs), which are mainly located in the axilla and lower neck (figure 3). Regional treatment, i.e. treatment of the LNs, can be indicated, and is determined by the axillary nodal status [41]. Clinical axillary staging is performed before surgery, using diagnostic imaging. In clinically node-negative patients, a sentinel-node biopsy (SNB) is conventionally performed during breast-conserving surgery (BCS). In SNB, one or more sentinel node(s) (SNs) are excised for histopathological examination. Depending on clinical and/or histopathological staging, regional treatment can consist of axillary



● *Figure 3 Schematic depiction of the anatomical location of regional lymph nodes. They are primarily located in the axilla and lower neck. Thanks: A.C. Farinha Bolhaqueiro.*

surgery and/or RT. Breast-cancer patients are a group that can benefit from MRI guidance in the MRL, for both local and regional treatments.

Breast-conserving therapy

Standard local treatment for early-stage breast-cancer and DCIS patients is breast-conserving therapy (BCT), which consists of BCS followed by RT of the whole breast. During BCS, the tumour is excised including a margin around it. Following BCS, adjuvant RT is performed in order to eradicate microscopic disease that can still be present in the breast. Conventional fractionated RT by whole-breast irradiation (WBI) is 25×2 Gy, for a total of 50 Gy. An additional boost can be delivered to the tumour bed to improve local control [42].

Target delineation is performed after BCS on RT-planning CT scans, with possible co-registration of other (preoperative) imaging scans. In case of a boost on the tumour bed, the surgeon can leave radio-opaque wires or clips to mark the tumour bed location after excision of the tumour. These are identified on the CT and serve as an aid for delineation. However, generally, it is difficult to establish the original tumour location in relation to the excision cavity walls, especially if no seroma formation is visible. This leads to high delineation variability among radiation oncologists [43–48].

Dose in WBI is generally delivered by 3-dimensional conformal RT (3DCRT) or intensity-modulated RT (IMRT) by the use of two tangential fields. The beam angles are chosen such that the beam edges inside the patient are aligned. WBI after BCS is shown to be an effective treatment, with a substantial benefit with respect to local recurrence and breast-cancer associated mortality [49]. However, WBI is associated with a number of acute and late complications, including pneumonitis, skin morbidity, cardiac events, oedema, and can lead to impaired cosmesis. Moreover, the long fractionation schedules, implemented over the course of several weeks, can be a substantial burden for patients. For this reason, hypofractionated schemes, i.e. RT in fewer fractions, have been initiated [50]. For example, WBI of 16×2.66 Gy is now common in the Netherlands. Hypofractionated WBI has comparable outcomes to conventional fractionated RT schedules [51,52].

Accelerated partial-breast irradiation

In order to reduce toxicity associated with WBI, and to further extend the concept of hypofractionation, alternative local RT approaches have been initialized. It has been shown that up to 88% of local recurrences are situated in close proximity to the original tumour location in patients who had undergone BCT [53,54]. Therefore, accelerated partial-breast irradiation (APBI) strategies have been initiated that aim to solely irradiate breast tissue surrounding the tumour bed, in hypofractionated schedules¹ (figure 4). Commonly used in APBI is a fractionation of 10 x 3.85 Gy [55]. Since most local recurrences are in the vicinity of the tumour location, adequate delivery of RT is crucial for APBI. Analogously to the WBI boost definition, postoperative target delineation for APBI is associated with high uncertainty [44,45,56,57]. A better strategy may be to perform APBI preoperatively, where the tumour *in situ* is visualized. No postoperative effects will thus be visible. Treatment volumes in preoperative APBI are substantially smaller than in postoperative APBI, and target delineation among radiation oncologists is consistent [58,59]. First results from a clinical APBI trial, delivering 10 x 4 Gy to the tumour preoperatively, show low complication rates and good cosmetic outcome [60]. Using preoperative MRI the tumour in relation to normal tissue is well defined. Therefore, preoperative APBI with higher fraction dose may be feasible. A phase-1 trial was recently initiated to investigate this concept, delivering a single 15 Gy, 18 Gy, or 21 Gy dose to the tumour [61–63]. First clinical results show favourable outcome and toxicity. At UMC Utrecht the *ABLATIVE* trial (NCT02316561) is ongoing which investigates the feasibility of an MRI-guided single-dose ablative dose as a minimally invasive *radiosurgical* alternative to BCT [64].

Treatment of lymph nodes

Until recently, in case of tumour-positive SN(s), or clinically tumour-positive LNs, standard treatment was axillary lymph node dissection (ALND). During ALND, a large number of LNs is usually removed.

¹ Other APBI techniques have also been developed: brachytherapy after lumpectomy, and external breast RT, performed intra-operatively, i.e. immediately following lumpectomy, during the surgery.



● *Figure 4 Delineations on a postoperative RT-planning CT in supine treatment position for both WBI and APBI. The target volume for WBI is the entire ipsilateral breast (green), whereas the target volumes for APBI (purple) are generated as extensions around the tumour bed (red). The other indicated structures are the heart (yellow), and body contour (orange).*

Although ALND is associated with excellent regional control, it causes morbidity in 60% of patients [65,66]. Associated side effects include arm oedema, shoulder pain and shoulder function restriction. In an attempt to achieve lower patient burden, alternative regional treatment approaches have been investigated in several clinical trials. These included the Z011 trial by the American College of Surgeons Oncology Group (ACOSOG), the International Breast Cancer Study Group (IBCSG) 23–01 trial, and the *After Mapping of the Axilla: Radiotherapy or Surgery?* (AMAROS) trial by the European Organization for Research and Treatment of Cancer (EORTC) [67–70]. Following the results of these large randomized trials, ALND is increasingly omitted, or replaced by regional RT, in patients with tumour-positive SN(s). Regional RT can also be indicated after ALND (in case of >3 tumour-positive LNs) on the periclavicular regions [71].

Regional RT comprises irradiation of the LNs in the axilla, with or without the supraclavicular area, and can include internal mammary LNs. Axillary RT is mostly delivered simultaneously with local RT (i.e. WBI or chest wall RT after mastectomy), usually by one or two additional beams, and in the same fractionation as the local RT. Regional target delineation is performed on RT-planning CT, by use of contouring guidelines, which are

mainly based on vessel structures and musculature [72–75], since direct LN visualization of CT is limited. Anatomical locations of LNs, as well as the number of LNs, can vary greatly between patients [76]. Consequently, CT-based targets in axillary RT are relatively large, resulting in large high-dose volumes in normal tissue, such as muscles, the brachial plexus, lungs, heart, and connective tissue. Complications associated with regional RT include arm oedema, decreased arm mobility, brachial plexopathy, and radiation pneumonitis [77]. A more accurate target definition, possibly enabled by MRI guidance, could reduce toxicity associated with regional RT. Moreover, if direct visualization of LNs is achieved, this opens possibilities for new regional RT techniques. This could include the delivery of a precise single-fraction high dose to individual LNs.

Breast radiotherapy on the MRI-linac

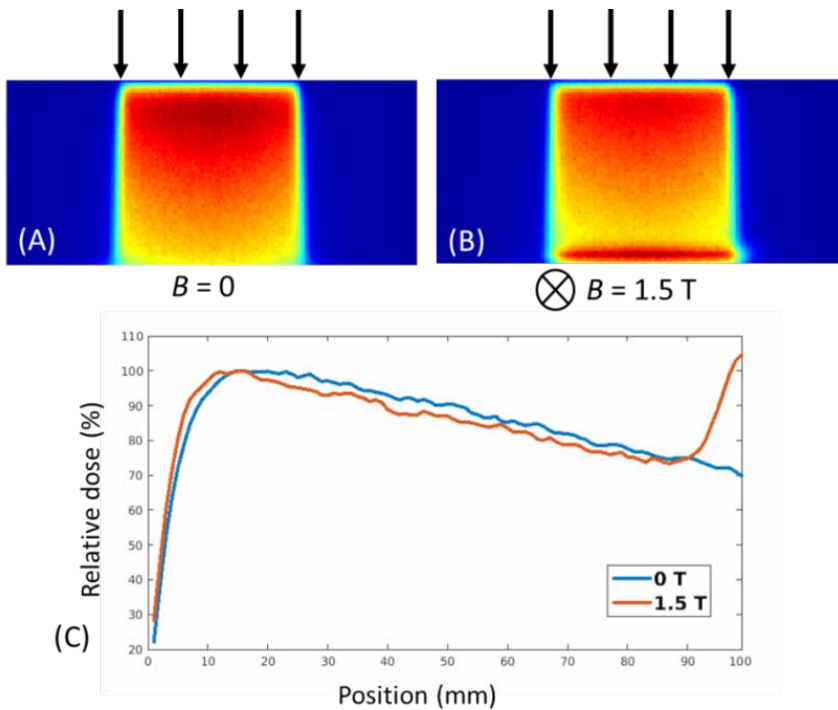
On-line MRI guidance can be a powerful tool for current local and regional RT treatments and may enable more sophisticated approaches. The added value of the MRL will mainly be visualization of the target in high contrast to surrounding anatomy. This may be crucial for safe and effective delivery of APBI techniques. Moreover, no additional (fiducial) markers will be needed, which are now used on conventional linacs for target visualization. These are inherently invasive, leading to patient burden, and marker-based methods are generally unable to handle anatomical deformations. Since target localization in WBI is possible with other imaging techniques, the potential added value for WBI in the MRL is that with on-line MRI guidance the definition of the boost volume during treatment is more accurate [56,78,79]. For APBI, the target definition is crucial. Especially in APBI performed preoperatively this can lead to new approaches since the tumour can be visualized on-line, *in situ*. With accurate target localization, fraction dose can be increased on the tumour, while surrounding tissue is spared. Furthermore, no additional treatment margins in the delivery of RT dose might be required on the MRL. In regional RT, compared to standard regional RT, more advanced RT strategies may be possible that target individual LNs. This allows dose escalation on tumour-positive LNs, and possibly omission of the need for axillary surgery.

For implementation of both standard and new RT techniques on the MRL, several aspects have to be taken into account. The dosimetry in the

MRL is different from a conventional linac, due to the 1.5 T magnetic field. Whether this has an influence on breast RT treatments is therefore a question of relevance. Another aspect to be investigated is the influence of motion on breast-RT treatments, given longer fraction durations and smaller targets. For the MRL, this may require an on-line MRI verification or adaptation strategy. Finally, conventional MRI techniques are used in diagnostic settings for tumour and LN identification, and are not optimized for RT planning on the MRL. For both local RT and regional RT, an optimization is therefore required when moving towards MRI guidance. Here we describe these aspects in more detail.

Dosimetric effects due to the magnetic field

Due to the presence of the magnetic field, dosimetry inside the MRL will change. In the MRL, photon beams deliver radiation perpendicular to the 1.5-T magnetic field. While photons are uncharged, secondary electrons carry electric charge. The Lorentz force acts perpendicularly to the electron's velocity vector direction, leading to a circular or helical electron path. As a consequence, the dose distribution will be affected. The impact on the dosimetry is mostly observed at interfaces between high and low density mediums [80], which for breast RT treatments is typically the skin. An electron exiting the skin will, under influence of the Lorentz force, be bent back towards the skin surface, where it will deposit its energy. This effect is referred to as the electron return effect (ERE), which can lead to significant dose increase at the surface (figure 5). The impact of the ERE is dependent on the orientation of the entry and exit side of the beam, relative to the tissue-air surface [81]. In WBI and axillary RT, target volumes are large and superficial, which means that extensive areas of skin are involved. Conversely, in APBI, target volumes are smaller and generally located deeper. Potential elevated skin dose may be a drawback, so the actual influence of the ERE on standard and new breast RT techniques in the MRL should be investigated.



● *Figure 5* Dose distributions simulated for a $10 \times 10 \text{ cm}^2$ 7 MV photon beam in a water phantom, at zero magnetic field (A), and at 1.5 T magnetic-field strength (B). Dose-depth curves through the central axis are depicted in (C). The beam enters the phantom in the direction of the arrows. The ERE is apparent on the exit side of the beam at 1.5 T. Thanks: M. Liefing.

Intra-fraction motion

Motion during dose delivery can affect accuracy of RT on the MRL. In order to minimize the impact of motion, an on-line MRI verification method should be developed. Two types of motion can be distinguished: inter-fraction and intra-fraction motion, i.e. movement between RT fractions and movement during RT delivery. Inter-fraction motion is associated with daily set-up variations and can be accounted for by daily pre-beam MRI acquisition. The RT plan is then adapted to the anatomy of the day. Motion during RT delivery is for breast-cancer patients mainly induced by respiration, and whole-body displacements, which are both typically on different time-scales. With target volumes becoming smaller, geometric miss of the target is more likely. A higher dose per fraction will lead to longer fraction durations, thereby further increasing the relevance

of intra-fraction motion. The extent of intra-fraction motion in breast RT should therefore be investigated to enable adaptive strategies on the MRL. Previous studies on WBI suggest that movement is generally limited to a maximum average of 5 mm during treatment, with large maximum deviations across patients [82]. Motion information was obtained with CBCT or EPID, with either lack of temporal or spatial resolution, and over limited time. On the MRL, MRI can be used to ascertain the impact of intra-fraction motion for breast RT. With MRI, the local motion of the targets in high spatial and temporal resolution can be characterized. Impact of both respiration and patient shifts could thus be inferred.

MRI-guided RT: local and regional

Diagnostic breast MRI techniques include T1w, T2w, dynamic contrast-enhanced MRI (DCE-MRI), and diffusion-weighted imaging (DWI) sequences, conventionally acquired at 1.5 T or 3 T field strengths. MRI for breast has high sensitivity for tumour detection and good correlation with microscopic tumour size [83,84]. MRI is also used for imaging of axillary LNs. Common techniques for axillary staging include DCE-MRI, T2w/T2*w methods, and DWI [85]. LN staging is based on LN size, relative T2 values, morphology, contrast agent uptake, or a combination of those factors. Since both sensitivity and specificity are relatively low, other methods are under investigation, including T2*w ultra-small paramagnetic iron oxide (USPIO)-enhanced techniques.

MRI for RT planning is not aimed at staging, but at achieving excellent target definition, and therefore MRI needs to be optimized for use in the MRL. Some aspects are inherent to the design of the MRL, such as the 1.5 T magnetic field strength, and the use of a flat patient table, in contrast to a more convex table in a conventional MR scanner. Furthermore, diagnostic MRI for breast is acquired in prone position, while in the MRL treatment position for breast RT is almost always supine, with both arms in abduction. Thus, the patient anatomy will be different, and other MRI receive coils will be used. Moreover, both geometric accuracy of the scans and a high isotropic resolution are important for dose calculations. As mentioned previously, MRI has a high added value in preoperative target delineation. This was shown in the *MAMRICT* (NTR3198) patient study, performed at our department [86]. For this study, a breast MR imaging protocol

in supine treatment position was developed. For the aforementioned *ABLATIVE* study, we have further optimized supine breast MRI for RT planning. Analogously, new MRI methods for regional RT planning have to be investigated, optimized, and assessed.

Aim and outline

The aim of this thesis is to explore the technical feasibility of local and regional breast-cancer RT treatments on the MRL.

Due to the static magnetic field in the MRL, the dosimetry is changed compared to a conventional linac. The ERE may induce a higher skin dose when breast-cancer patients are treated in the MRL, due to large and superficial target volumes. This effect will be studied in **chapter 2** for three breast RT approaches, including two WBI and an APBI technique.

The role of intra-fraction motion becomes more important, as geometric miss of the target becomes more likely. Using MRI techniques, local motion of target volumes can be imaged in high temporal and high spatial resolution. In **chapter 3**, intra-fraction motion of target volumes, including the tumour (bed) and whole breast, is characterized by using MRI on two temporal scales.

Due to limited visibility of individual LNs on CT, anatomical boundaries are commonly used for conventional target delineation in regional RT. MRI has the potential to visualize individual axillary LNs explicitly. In **chapter 4**, we describe MRI methods which were optimized in healthy volunteers, in view of regional RT planning.

Both anatomy and posture endurance for undergoing MRI in supine treatment position in patients can differ from healthy volunteers; axillary surgery can further affect both anatomy and posture endurance for undergoing MRI. **Chapter 5** describes the feasibility and reproducibility of MRI of axillary LNs. This was performed, before and after SNB in 23 low-risk breast-cancer or DCIS patients, in the *MILANO* (NL50046.041.14) patient study.

With the availability of dedicated MRI techniques, individual LNs could be irradiated in the MRL with high precision. We investigated the dosimetric feasibility of delivering a single-fraction high dose (boost) in the MRL to individual LNs, additional to conventional WBI and regional RT. Four boost locations in five patients from the *MILANO* patient study are selected to receive an RT boost up to ablative dose. Clinical constraints are evaluated on total dose plans, including for the brachial plexus and chest wall. The study is described in **chapter 6**.

The most important results are summarized and put into context in **chapter 7**.

References

- [1] Khan FM. *The Physics of Radiation Therapy - Fourth Edition*. Lippincott Williams & Wilkins, a Wolter Kluwer business; 2010.
- [2] Gordon Steel G. *Basic Clinical Radiobiology*. 3rd ed. Arnold; 2002.
- [3] Burnet NG, Thomas SJ, Burton KE, Jefferies SJ. Defining the tumour and target volumes for radiotherapy. *Cancer Imaging* 2004;4:153–61. doi:10.1102/1470-7330.2004.0054.
- [4] Wiklund K, Toma-Dasu I, Lind BK. Impact of dose and sensitivity heterogeneity on TCP. *Comput Math Methods Med* 2014;2014:182935. doi:10.1155/2014/182935.
- [5] van Herk M. Errors and margins in radiotherapy. *Semin Radiat Oncol* 2004;14:52–64. doi:10.1053/j.semradonc.2003.10.003.
- [6] van Herk M, Remeijer P, Rasch C, Lebesque J V. The probability of correct target dosage: dose-population histograms for deriving treatment margins in radiotherapy. *Int J Radiat Oncol* 2000;47:1121–35. doi:10.1016/S0360-3016(00)00518-6.
- [7] Schmidt MA, Payne GS. Radiotherapy planning using MRI. *Phys Med Biol* 2015;60:R323–61. doi:10.1088/0031-9155/60/22/R323.
- [8] Schmitz AC, Pengel KE, Loo CE, van den Bosch M a a J, Wesseling J, Gertenbach M, et al. Pre-treatment imaging and pathology characteristics of invasive breast cancers of limited extent: potential relevance for MRI-guided localized therapy. *Radiother Oncol* 2012;104:11–8. doi:10.1016/j.radonc.2012.04.014.
- [9] Alderliesten T, Loo C, Paape A, Muller S, Rutgers E, Peeters M-JV, et al. On the feasibility of MRI-guided navigation to demarcate breast cancer for breast-conserving surgery. *Med Phys* 2010;37:2617–26. doi:10.1118/1.3429048.
- [10] Commandeur F, Simon A, Mathieu R, Nassef M, Ospina JD, Rolland Y, et al. MRI to CT prostate registration for improved targeting in cancer external beam radiotherapy. *IEEE J Biomed Heal Informatics* 2016. doi:10.1109/JBHI.2016.2581881.
- [11] Gurney-Champion OJ, Lens E, van der Horst A, Houweling AC, Klaassen R, van Hooff JE, et al. Visibility and artifacts of gold fiducial markers used for image guided radiation therapy of pancreatic cancer on MRI. *Med Phys* 2015;42:2638–47. doi:10.1118/1.4918753.
- [12] Heerkens HD, van Vulpen M, van den Berg CAT, Tijssen RHN, Crijns SPM, Molenaar IQ, et al. MRI-based tumor motion characterization and gating schemes for radiation therapy of pancreatic cancer. *Radiother Oncol* 2014;111:252–7. doi:10.1016/j.radonc.2014.03.002.
- [13] Burbach JPM, Kleijnen J-PJ, Reerink O, Seravalli E, Philippens MEP, Schakel T, et al. Inter-observer agreement of MRI-based tumor delineation for preoperative radiotherapy boost in locally advanced rectal cancer. *Radiother Oncol* 2016;118:399–407. doi:10.1016/j.radonc.2015.10.030.
- [14] Kleijnen J-PJE, van Asselen B, Burbach JPM, Intven M, Philippens MEP, Reerink O, et al. Evolution of motion uncertainty in rectal cancer: implications for adaptive radiotherapy. *Phys Med Biol* 2016;61:1–11. doi:10.1088/0031-9155/61/1/1.
- [15] McPartlin AJ, Li XA, Kershaw LE, Heide U, Kerkmeijer L, Lawton C, et al. MRI-guided prostate adaptive radiotherapy - A systematic review. *Radiother Oncol* 2016;119:371–80. doi:10.1016/j.radonc.2016.04.014.
- [16] Van Der Heide UA, Korporaal JG, Groenendaal G, Franken S, Van Vulpen M. Functional MRI for tumor delineation in prostate radiation therapy. *Imaging Med* 2011;3:219–31. doi:10.2217/IIM.11.10.

- [17] Smith RP, Bloch P, Harris EE, McDonough J, Sarkar A, Kassaei A, et al. Analysis of interfraction and intrafraction variation during tangential breast irradiation with an electronic portal imaging device. *Int J Radiat Oncol Biol Phys* 2005;62:373–8. doi:10.1016/j.ijrobp.2004.10.022.
- [18] Rasch C, Barillot I, Remeijer P, Touw A, van Herk M, Lebesque J V. Definition of the prostate in CT and MRI: a multi-observer study. *Int J Radiat Oncol* 1999;43:57–66. doi:10.1016/S0360-3016(98)00351-4.
- [19] Dimopoulos JCA, Petrow P, Tanderup K, Petric P, Berger D, Kirisits C, et al. Recommendations from Gynaecological (GYN) GEC-ESTRO Working Group (IV): Basic principles and parameters for MR imaging within the frame of image based adaptive cervix cancer brachytherapy. *Radiother Oncol* 2012;103:113–22. doi:10.1016/j.radonc.2011.12.024.
- [20] Viswanathan AN, Dimopoulos J, Kirisits C, Berger D, Pötter R. Computed Tomography Versus Magnetic Resonance Imaging-Based Contouring in Cervical Cancer Brachytherapy: Results of a Prospective Trial and Preliminary Guidelines for Standardized Contours. *Int J Radiat Oncol* 2007;68:491–8. doi:10.1016/j.ijrobp.2006.12.021.
- [21] Lagendijk JJW, Raaymakers BW, van Vulpen M. The magnetic resonance imaging-linac system. *Semin Radiat Oncol* 2014;24:207–9. doi:10.1016/j.semradonc.2014.02.009.
- [22] Mutic S, Dempsey JF. The ViewRay system: magnetic resonance-guided and controlled radiotherapy. *Semin Radiat Oncol* 2014;24:196–9. doi:10.1016/j.semradonc.2014.02.008.
- [23] Fallone BG. The rotating biplanar linac-magnetic resonance imaging system. *Semin Radiat Oncol* 2014;24:200–2. doi:10.1016/j.semradonc.2014.02.011.
- [24] Keall PJ, Barton M, Crozier S, Australian MRI-Linac Program, including contributors from Ingham Institute, Illawarra Cancer Care Centre, Liverpool Hospital, Stanford University, Universities of Newcastle, Queensland, Sydney, Western Sydney, and Wollongong. The Australian magnetic resonance imaging-linac program. *Semin Radiat Oncol* 2014;24:203–6. doi:10.1016/j.semradonc.2014.02.015.
- [25] Lagendijk JJW, Raaymakers BW, Raaijmakers AJE, Overweg J, Brown KJ, Kerkhof EM, et al. MRI/linac integration. *Radiother Oncol* 2008;86:25–9. doi:10.1016/j.radonc.2007.10.034.
- [26] Lagendijk JJW, van Vulpen M, Raaymakers BW. The development of the MRI linac system for online MRI-guided radiotherapy: a clinical update. *J Intern Med* 2016;280:203–8. doi:10.1111/joim.12516.
- [27] Akino Y, Oh R-J, Masai N, Shiomi H, Inoue T. Evaluation of potential internal target volume of liver tumors using cine-MRI. *Med Phys* 2014;41:111704. doi:10.1118/1.4896821.
- [28] Sawant A, Keall P, Pauly KB, Alley M, Vasawala S, Loo BW, et al. Investigating the feasibility of rapid MRI for image-guided motion management in lung cancer radiotherapy. *Biomed Res Int* 2014;2014:485067. doi:10.1155/2014/485067.
- [29] Bieri O, Scheffler K. Fundamentals of balanced steady state free precession MRI. *J Magn Reson Imaging* 2013;38:2–11. doi:10.1002/jmri.24163.
- [30] Tsao J, Kozerke S, Boesiger P, Pruessmann KP. Optimizing spatiotemporal sampling for k-t BLAST and k-t SENSE: application to high-resolution real-time cardiac steady-state free precession. *Magn Reson Med* 2005;53:1372–82. doi:10.1002/mrm.20483.
- [31] Glitzner M, de Senneville BD, Lagendijk JJW, Raaymakers BW, Crijns SPM. On-line 3D motion estimation using low resolution MRI. *Phys Med Biol* 2015;60:N301–10. doi:10.1088/0031-9155/60/16/N301.
- [32] Kubo HD, Hill BC. Respiration gated radiotherapy treatment: a technical study. *Phys Med Biol* 1996;41:83–91. doi:10.1088/0031-9155/41/1/007.

- [33] Crijns SPM, Kok JGM, Lagendijk JJW, Raaymakers BW. Towards MRI-guided linear accelerator control: gating on an MRI accelerator. *Phys Med Biol* 2011;56:4815–25. doi:10.1088/0031-9155/56/15/012.
- [34] Glitzner M, Crijns SPM, de Senneville BD, Lagendijk JJW, Raaymakers BW. On the suitability of Elekta's Agility 160 MLC for tracked radiation delivery: closed-loop machine performance. *Phys Med Biol* 2015;60:2005–17. doi:10.1088/0031-9155/60/5/2005.
- [35] Crijns SPM, Raaymakers BW, Lagendijk JJW. Proof of concept of MRI-guided tracked radiation delivery: tracking one-dimensional motion. *Phys Med Biol* 2012;57:7863–72. doi:10.1088/0031-9155/57/23/7863.
- [36] Bjerre T, Crijns S, af Rosenschöld PM, Aznar M, Specht L, Larsen R, et al. Three-dimensional MRI-linac intra-fraction guidance using multiple orthogonal cine-MRI planes. *Phys Med Biol* 2013;58:4943–50. doi:10.1088/0031-9155/58/14/4943.
- [37] Breast cancer in The Netherlands: Incidence, prevalence, survival, mortality and risk. Accessed Sept 2016 n.d. www.cijfersoverkanker.nl.
- [38] Verbeek ALM, Broeders MJM, Otto SJ, Frachebou J, Otten JDMH, Holland R, et al. [Effects of the population screening into breast cancer]. *Ned Tijdschr Geneesk* 2013;157:A5218.
- [39] Bluekens AMJ, Holland R, Karssemeijer N, Broeders MJM, den Heeten GJ. Comparison of digital screening mammography and screen-film mammography in the early detection of clinically relevant cancers: a multicenter study. *Radiology* 2012;265:707–14. doi:10.1148/radiol.12111461.
- [40] EBCTCG (Early Breast Cancer Trialists' Collaborative Group). Effect of radiotherapy after mastectomy and axillary surgery on 10-year recurrence and 20-year breast cancer mortality: meta-analysis of individual patient data for 8135 women in 22 randomised trials. *Lancet* 2014. doi:10.1016/S0140-6736(14)60488-8.
- [41] Samphao S, Eremin JM, El-Sheemy M, Eremin O. Management of the axilla in women with breast cancer: current clinical practice and a new selective targeted approach. *Ann Surg Oncol* 2008;15:1282–96. doi:10.1245/s10434-008-9863-8.
- [42] Bartelink H, Maingon P, Poortmans P, Weltens C, Fourquet A, Jager J, et al. Whole-breast irradiation with or without a boost for patients treated with breast-conserving surgery for early breast cancer: 20-year follow-up of a randomised phase 3 trial. *Lancet Oncol* 2015;16:47–56. doi:10.1016/S1470-2045(14)71156-8.
- [43] Whipp EC, Halliwell M. Magnetic resonance imaging appearances in the postoperative breast: the clinical target volume-tumor and its relationship to the chest wall. *Int J Radiat Oncol Biol Phys* 2008;72:49–57. doi:10.1016/j.ijrobp.2007.12.021.
- [44] Struikmans H, Wárlám-Rodenhuis C, Stam T, Stapper G, Tersteeg RJHA, Bol GH, et al. Interobserver variability of clinical target volume delineation of glandular breast tissue and of boost volume in tangential breast irradiation. *Radiother Oncol* 2005;76:293–9. doi:10.1016/j.radonc.2005.03.029.
- [45] Landis DM, Luo W, Song J, Bellon JR, Punglia RS, Wong JS, et al. Variability among breast radiation oncologists in delineation of the postsurgical lumpectomy cavity. *Int J Radiat Oncol Biol Phys* 2007;67:1299–308. doi:10.1016/j.ijrobp.2006.11.026.
- [46] Kirby AM, Yarnold JR, Evans PM, Morgan V a, Schmidt M a, Scurr ED, et al. Tumor bed delineation for partial breast and breast boost radiotherapy planned in the prone position: what does MRI add to X-ray CT localization of titanium clips placed in the excision cavity wall? *Int J Radiat Oncol Biol Phys* 2009;74:1276–82. doi:10.1016/j.ijrobp.2009.02.028.

- [47] Giezen M, Kouwenhoven E, Scholten AN, Coerkamp EG, Heijnenbrok M, Jansen WPA, et al. Magnetic resonance imaging-versus computed tomography-based target volume delineation of the glandular breast tissue (clinical target volume breast) in breast-conserving therapy: An exploratory study. *Int J Radiat Oncol Biol Phys* 2011;81:804–11.
- [48] den Hartogh MD, van Asselen B, Monnikhof EM, van den Bosch M a J, van Vulpen M, van Diest PJ, et al. Excised and irradiated volumes in relation to the tumor size in breast-conserving therapy. *Breast Cancer Res Treat* 2011;129:857–65. doi:10.1007/s10549-011-1696-7.
- [49] Early Breast Cancer Trialists' Collaborative Group (EBCTCG), Darby S, McGale P, Correa C, Taylor C, Arriagada R, et al. Effect of radiotherapy after breast-conserving surgery on 10-year recurrence and 15-year breast cancer death: meta-analysis of individual patient data for 10,801 women in 17 randomised trials. *Lancet (London, England)* 2011;378:1707–16. doi:10.1016/S0140-6736(11)61629-2.
- [50] Min C, Connolly E, Chen T, Jozsef G, Formenti SC. Hypofractionated radiation therapy for early stage breast cancer: outcomes, toxicities, and cost analysis. *Breast J* 2014;20:267–73. doi:10.1111/tbj.12254.
- [51] Haviland JS, Owen JR, Dewar JA, Agrawal RK, Barrett J, Barrett-Lee PJ, et al. The UK Standardisation of Breast Radiotherapy (START) trials of radiotherapy hypofractionation for treatment of early breast cancer: 10-year follow-up results of two randomised controlled trials. *Lancet Oncol* 2013;14:1086–94. doi:10.1016/S1470-2045(13)70386-3.
- [52] Whelan T, Levine M. More evidence that locoregional radiation therapy improves survival: what should we do? *J Natl Cancer Inst* 2005;97:82–4. doi:10.1093/jnci/djh328.
- [53] Cajucom CC, Tsangaris TN, Nemoto T, Driscoll D, Penetrante RB, Holyoke ED. Results of salvage mastectomy for local recurrence after breast-conserving surgery without radiation therapy. *Cancer* 1993;71:1774–9.
- [54] Huang E, Buchholz TA, Meric F, Krishnamurthy S, Mirza NQ, Ames FC, et al. Classifying local disease recurrences after breast conservation therapy based on location and histology: new primary tumors have more favorable outcomes than true local disease recurrences. *Cancer* 2002;95:2059–67. doi:10.1002/cncr.10952.
- [55] Njeh CF, Saunders MW, Langton CM. Accelerated Partial Breast Irradiation (APBI): A review of available techniques. *Radiat Oncol* 2010;5:90. doi:10.1186/1748-717X-5-90.
- [56] Hurkmans C, Admiraal M, van der Sangen M, Dijkmans I. Significance of breast boost volume changes during radiotherapy in relation to current clinical interobserver variations. *Radiother Oncol* 2009;90:60–5. doi:10.1016/j.radonc.2007.12.001.
- [57] van Mourik AM, Elkhuizen PHM, Minkema D, Duppen JC, van Vliet-Vroegindewij C. Multiinstitutional study on target volume delineation variation in breast radiotherapy in the presence of guidelines. *Radiother Oncol* 2010;94:286–91. doi:10.1016/j.radonc.2010.01.009.
- [58] den Hartogh MD, Philippens MEP, van Dam IE, Kleynen CE, Tersteeg RJHA, Pijnappel RM, et al. MRI and CT imaging for preoperative target volume delineation in breast-conserving therapy. *Radiat Oncol* 2014;9:63. doi:10.1186/1748-717X-9-63.
- [59] van der Leij F, Elkhuizen PHM, Janssen TM, Poortmans P, van der Sangen M, Scholten AN, et al. Target volume delineation in external beam partial breast irradiation: Less inter-observer variation with preoperative- compared to postoperative delineation. *Radiother Oncol* 2013;110:467–70. doi:10.1016/j.radonc.2013.10.033.
- [60] van der Leij F, Bosma SCJ, van de Vijver MJ, Wesseling J, Vreeswijk S, Rivera S, et al. First results of the preoperative accelerated partial breast irradiation (PAPBI) trial. *Radiother Oncol* 2015. doi:10.1016/j.radonc.2015.02.002.

- [61] Blitzblau RC, Arya R, Yoo S, Baker JA, Chang Z, Palta M, et al. A phase 1 trial of preoperative partial breast radiation therapy: Patient selection, target delineation, and dose delivery. *Pract Radiat Oncol* 2015. doi:10.1016/j.prro.2015.02.002.
- [62] Palta M, Yoo S, Adamson JD, Prosnitz LR, Horton JK. Preoperative single fraction partial breast radiotherapy for early-stage breast cancer. *Int J Radiat Oncol Biol Phys* 2012;82:37–42. doi:10.1016/j.ijrobp.2010.09.041.
- [63] Horton JK, Blitzblau RC, Yoo S, Georgiade GS, Geradts J, Baker J a, et al. Preoperative Single-Fraction Partial Breast Radiation Therapy: A Novel Phase 1 Dose-Escalation Protocol and Exploration of Breast Cancer Radiation Response. *Int J Radiat Oncol* 2013;87:S229. doi:http://dx.doi.org/10.1016/j.ijrobp.2013.06.594.
- [64] Charaghvandi RK, den Hartogh MD, van Ommen A-MLN, de Vries WJH, Scholten V, Moerland MA, et al. MRI-guided single fraction ablative radiotherapy for early-stage breast cancer: a brachytherapy versus volumetric modulated arc therapy dosimetry study. *Radiother Oncol* 2015;117:477–82. doi:10.1016/j.radonc.2015.09.023.
- [65] Ivens D, Hoe AL, Podd TJ, Hamilton CR, Taylor I, Royle GT. Assessment of morbidity from complete axillary dissection. *Br J Cancer* 1992;66:136–8.
- [66] Kakuda JT, Stuntz M, Trivedi V, Klein SR, Vargas HI. Objective assessment of axillary morbidity in breast cancer treatment. *Am Surg* 1999;65:995–8.
- [67] Donker M, van Tienhoven G, Straver ME, Meijnen P, van de Velde CJH, Mansel RE, et al. Radiotherapy or surgery of the axilla after a positive sentinel node in breast cancer (EORTC 10981-22023 AMAROS): a randomised, multicentre, open-label, phase 3 non-inferiority trial. *Lancet Oncol* 2014;15:1303–10. doi:10.1016/S1470-2045(14)70460-7.
- [68] Giuliano AE, McCall L, Beitsch P, Whitworth PW, Blumencranz P, Leitch AM, et al. Locoregional recurrence after sentinel lymph node dissection with or without axillary dissection in patients with sentinel lymph node metastases: the American College of Surgeons Oncology Group Z0011 randomized trial. *Ann Surg* 2010;252:426–32; discussion 432–3. doi:10.1097/SLA.0b013e3181f08f32.
- [69] Galimberti V, Cole BF, Zurrada S, Viale G, Luini A, Veronesi P, et al. Axillary dissection versus no axillary dissection in patients with sentinel-node micrometastases (IBCSG 23-01): a phase 3 randomised controlled trial. *Lancet Oncol* 2013;14:297–305. doi:10.1016/S1470-2045(13)70035-4.
- [70] Giuliano AE, Ballman K, McCall L, Beitsch P, Whitworth PW, Blumencranz P, et al. Locoregional Recurrence After Sentinel Lymph Node Dissection With or Without Axillary Dissection in Patients With Sentinel Lymph Node Metastases. *Ann Surg* 2016;1. doi:10.1097/SLA.0000000000001863.
- [71] Guenzi M, Blandino G, Vidili MG, Aloï D, Configliacco E, Verzanini E, et al. Hypofractionated irradiation of infra-supraclavicular lymph nodes after axillary dissection in patients with breast cancer post-conservative surgery: impact on late toxicity. *Radiat Oncol* 2015;10:177. doi:10.1186/s13014-015-0480-y.
- [72] Offersen B V, Boersma LJ, Kirkove C, Hol S, Aznar MC, Biete Sola A, et al. ESTRO consensus guideline on target volume delineation for elective radiation therapy of early stage breast cancer. *Radiother Oncol* 2015;114:3–10. doi:10.1016/j.radonc.2014.11.030.
- [73] Nielsen MH, Berg M, Pedersen AN, Andersen K, Glavicic V, Jakobsen EH, et al. Delineation of target volumes and organs at risk in adjuvant radiotherapy of early breast cancer: national guidelines and contouring atlas by the Danish Breast Cancer Cooperative Group. *Acta Oncol* 2013;52:703–10. doi:10.3109/0284186X.2013.765064.
- [74] Verhoeven K, Weltens C, Remouchamps V, Mahjoubi K, Veldeman L, Lengele B, et al. Vessel based delineation guidelines for the elective lymph node regions in breast cancer radiation therapy - PROCAB guidelines. *Radiother Oncol* 2015;114:11–6. doi:10.1016/j.radonc.2014.11.008.

- [75] Gentile MS, Usman AA, Neuschler EI, Sathiaselvan V, Hayes JP, Small W. Contouring Guidelines for the Axillary Lymph Nodes for the Delivery of Radiation Therapy in Breast Cancer: Evaluation of the RTOG Breast Cancer Atlas. *Int J Radiat Oncol* 2015;93:257–65. doi:10.1016/j.ijrobp.2015.07.002.
- [76] Dijkema IM, Hofman P, Raaijmakers CPJ, Lagendijk JJ, Battermann JJ, Hillen B. Loco-regional conformal radiotherapy of the breast: delineation of the regional lymph node clinical target volumes in treatment position. *Radiother Oncol* 2004;71:287–95. doi:10.1016/j.radonc.2004.02.017.
- [77] Donker M, Straver ME, van Tienhoven G, van de Velde CJH, Mansel RE, Litière S, et al. Comparison of the sentinel node procedure between patients with multifocal and unifocal breast cancer in the EORTC 10981-22023 AMAROS Trial: Identification rate and nodal outcome. *Eur J Cancer* 2013;2093–100. doi:10.1016/j.ejca.2013.02.017.
- [78] Boersma LJ, Janssen T, Elkhuizen PHM, Poortmans P, Van Der Sangen M, Scholten AN, et al. Reducing interobserver variation of boost-CTV delineation in breast conserving radiation therapy using a pre-operative CT and delineation guidelines. *Radiother Oncol* 2012;103:178–82. doi:10.1016/j.radonc.2011.12.021.
- [79] Alderliesten T, den Hollander S, Yang T-IJ, Elkhuizen PHM, van Mourik AM, Hurkmans C, et al. Dosimetric impact of post-operative seroma reduction during radiotherapy after breast-conserving surgery. *Radiother Oncol* 2011;100:265–70. doi:10.1016/j.radonc.2011.03.008.
- [80] Raaijmakers AJE, Raaymakers BW, Lagendijk JJW. Integrating a MRI scanner with a 6 MV radiotherapy accelerator: dose increase at tissue-air interfaces in a lateral magnetic field due to returning electrons. *Phys Med Biol* 2005;50:1363–76. doi:10.1088/0031-9155/50/7/002.
- [81] Raaijmakers AJE, Raaymakers BW, van der Meer S, Lagendijk JJW. Integrating a MRI scanner with a 6 MV radiotherapy accelerator: impact of the surface orientation on the entrance and exit dose due to the transverse magnetic field. *Phys Med Biol* 2007;52:929–39. doi:10.1088/0031-9155/52/4/005.
- [82] Michalski A, Atyeo J, Cox J, Rinks M. Inter- and intra-fraction motion during radiation therapy to the whole breast in the supine position: a systematic review. *J Med Imaging Radiat Oncol* 2012;56:499–509. doi:10.1111/j.1754-9485.2012.02434.x.
- [83] Schmitz AC, Pengel KE, Loo CE, van den Bosch MAAJ, Wesseling J, Gertenbach M, et al. Pre-treatment imaging and pathology characteristics of invasive breast cancers of limited extent: potential relevance for MRI-guided localized therapy. *Radiother Oncol* 2012;104:11–8. doi:10.1016/j.radonc.2012.04.014.
- [84] Schmitz AC, van den Bosch MAAJ, Loo CE, Mali WPTM, Bartelink H, Gertenbach M, et al. Precise correlation between MRI and histopathology - exploring treatment margins for MRI-guided localized breast cancer therapy. *Radiother Oncol* 2010;97:225–32. doi:10.1016/j.radonc.2010.07.025.
- [85] Kuijjs VJL, Moosdorff M, Schipper RJ, Beets-Tan RGH, Heuts EM, Keymeulen KBMI, et al. The role of MRI in axillary lymph node imaging in breast cancer patients: a systematic review. *Insights Imaging* 2015;6:203–15. doi:10.1007/s13244-015-0404-2.
- [86] den Hartogh MD, Philippens ME, van Dam IE, Kleynen CE, Tersteeg RJ, Pijnappel RM, et al. MRI and CT imaging for preoperative target volume delineation in breast-conserving therapy. *Radiat Oncol* 2014;9:63. doi:10.1186/1748-717X-9-63.



“Never assume.”

Astrid van Weerd



MR-guided breast radiotherapy: feasibility and magnetic-field impact on skin dose

Tristan C. F. van Heijst
Mariska D. den Hartogh
Jan J. W. Lagendijk
H. J. G. Desirée van den Bongard
Bram van Asselen

Physics in Medicine and Biology 58 (2013) 6917-5930

Abstract

The UMC Utrecht MRI/linac (MRL) design provides image guidance with high soft-tissue contrast, directly during radiotherapy (RT). Breast cancer patients are a potential group to benefit from better guidance in the MRL. However, due to the electron return effect, the skin dose can be increased in presence of a magnetic field. Since large skin areas are generally involved in breast RT, the purpose of this study is to investigate the effects on the skin dose, for whole-breast irradiation (WBI) and accelerated partial-breast irradiation (APBI). In ten patients with early-stage breast cancer, targets and organs at risk (OARs) were delineated on postoperative CT scans co-registered with MRI. The OARs included the skin, comprising the first 5 mm of ipsilateral-breast tissue, plus extensions. Three intensity-modulated RT (IMRT) techniques were considered (2x WBI, 1x APBI). Individual beam geometries were used for all patients. Specially developed MRL treatment-planning software was used. Acceptable plans were generated for 0 T, 0.35 T, and 1.5 T, using a class solution. The skin dose was augmented in WBI in presence of a magnetic field, which is a potential drawback, whereas in APBI the induced effects were negligible. This opens possibilities for developing MR-guided partial-breast treatments in the MRL.

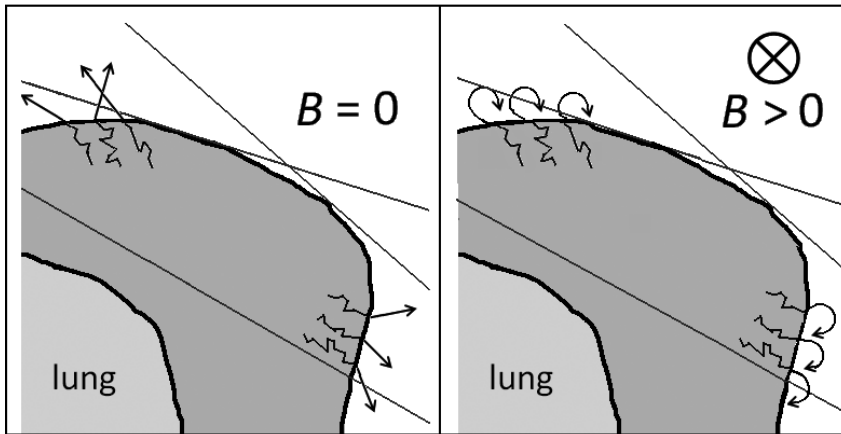
Introduction

Magnetic resonance imaging (MRI) guidance for radiotherapy (RT) has the potential of fast, high soft-tissue contrast visualization of tumours and organs at risk (OARs), directly on the treatment table. At the UMC Utrecht a hybrid MRI/linac (MRL) is constructed which integrates a 1.5 T closed-bore MRI scanner (Philips, Best, The Netherlands) with a linear accelerator (Elekta AB, Stockholm, Sweden), mounted on a ring-shaped gantry [1]. Several other groups are currently working on MR-guided RT in cancer treatment as well [2,3]. MRI combined with RT offers possibilities for introducing high-precision MR-guided treatments for breast cancer patients.

The standard of care for early-stage breast cancer and ductal carcinoma in situ (DCIS) patients is breast-conserving therapy (BCT) which consists of breast-conserving surgery (BCS), followed by whole-breast irradiation (WBI). The dose is generally delivered by intensity-modulated RT (IMRT) using two tangential beams. Furthermore, in low-risk breast cancer patients, accelerated partial-breast irradiation (APBI) studies using IMRT are ongoing [4–8].

In both WBI and APBI, image guidance is currently performed using portal imaging or cone-beam CT [9,10]. Direct visualization of the target volumes is especially important when considering boosts to the target volume, which both modalities do not allow with high tissue-contrast. MR guidance is potentially useful for on-line high-contrast visualization of the tumour bed in postoperative RT, or for tumour detection in a preoperative setting [8,11–14]. However, apart from developing novel targeting techniques, it is of great importance to investigate the induced effects of the magnetic field itself on the dose distribution.

In the MRL a static magnetic field is always present during treatment. Charged particles moving in a magnetic field are acted upon by the Lorentz force, perpendicularly to their velocity direction. As a consequence, secondary electrons emanating from the skin into air can be bent back, resulting in a dose increase at the surface (figure 1). This electron return effect (ERE) is clearly observed at boundaries between layers with large density differences, and can induce a significant increase of skin dose,



● Figure 1 Illustration of the ERE, for left-breast WBI by means of two tangential fields. The edges of the photon beams are depicted by the straight lines. Trajectories of secondary electrons, crossing the skin-air boundary on either exit side of the irradiated breast, are represented by the arrows. The ERE may result in a higher skin dose when comparing the situation of no magnetic field (left) to that of a non-zero magnetic field directed into the plane (right).

as shown by Raaijmakers *et al.* [15]. The magnetic field also results in a shorter build-up distance which may play a role in a higher skin dose.

The ERE depends on the inclinations of the beams to the skin surface, with oblique angles inducing the highest increase [16] and opposing beams compensating for the effect at perpendicular interfaces [15]. In WBI treatments, oblique beam/surface inclinations are ubiquitous and the target volume is superficial and relatively large. This results in a large irradiated area of skin. Treatments by APBI, however, are performed with several fields which do not necessarily all have oblique orientations. Additionally, APBI fields are generally smaller since they target smaller volumes and, moreover, the target volumes are not necessarily superficial. Hence, a smaller region of skin generally receives high dose, so that induced effects of the magnetic field are expected to be less prominent in APBI relative to WBI.

Current cosmetic results for WBI and APBI are good to excellent [7,8,17,18]. Further increase in skin dose could lead to a higher rate and severity of negative side effects of RT. Complications of the skin should be minimized in the treatment of breast cancer; therefore the main objective of this study is to investigate the physical effects of the magnetic field on the skin dose for WBI and for APBI.

Methods and materials

Patients

Ten BCT patients treated at the RT Department of the UMC Utrecht in 2011 or 2012 were enrolled in our treatment-planning study. The median age of the women was 63 years (range: 39 – 72 years). One patient had breast cancer on both sides and for this study both tumours were considered separately. In total, 6 of the tumours were right-sided and 5 were located in the left breast. The majority of the excised tumours were stage T1c (7), while the rest were stage T1b (2) or stage T2 (2). No patients had tumour-positive lymph nodes. The median volume of the ipsilateral breast was 1003 cc (range: 705 – 2373 cc).

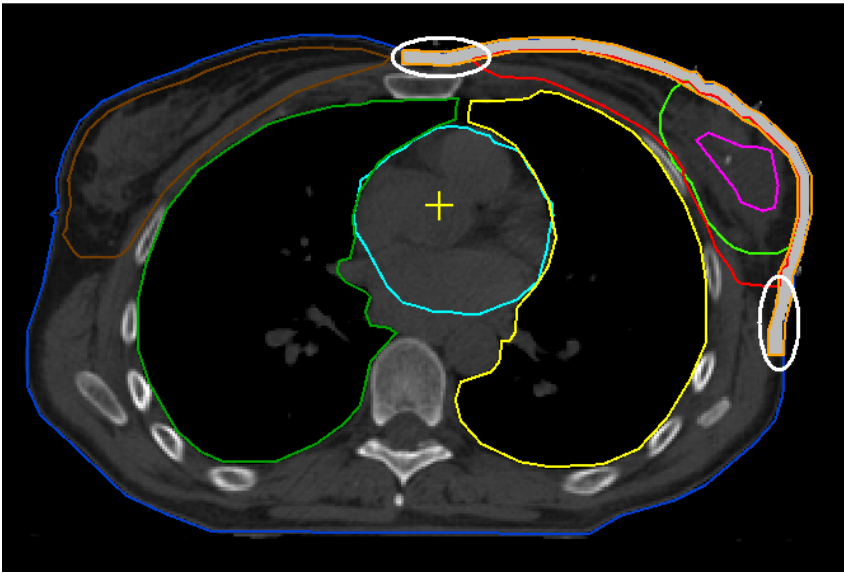
RT techniques

The magnetic-field-induced effects were studied for both WBI and APBI. In WBI a dose of 42.56 Gy was prescribed to the breast, delivered in 16 fractions of 2.66 Gy. The first WBI technique considered was the classical tangential two-field set-up using IMRT (WBI-2). The beam angles in WBI-2 were determined such that the two beam edges inside each patient aligned, which was done for each patient individually. In order to investigate the influence of the magnetic field on multiple beam directions, also a seven-field IMRT technique was used for WBI (WBI-7) in which the beam orientations were chosen individually for each patient. For APBI, target prescription was 10 fractions of 3.85 Gy, to a total dose of 38.5 Gy, according to the 2008 IRMA study protocol of the European Organization for Research and Treatment of Cancer Radiation Oncology Group (EORTC ROG). A seven-field IMRT technique with individually determined beam angles was chosen to for the APBI approach (APBI-7).

Volumes of interest

All patients underwent a planning CT with 3 mm slice thickness, at three weeks (median: 21 days, range: 14 – 50 days) after surgery, in supine RT position. The palpable breast tissue was indicated with a copper wire. For WBI, the clinical target volume for the whole breast (CTV_{WBI}) was delineated according to the Radiotherapy Oncology Group (RTOG) Breast Cancer Contouring Atlas. A 5 mm margin was applied to the CTV_{WBI} to generate the planning target volume (PTV_{WBI}), excluding the first 5 mm under the surface (figure 2). The median PTV_{WBI} was 741 cc (range: 517 – 2028 cc). Delineations of the target volumes in APBI were performed according to the 2008 IRMA study protocol of EORTC ROG. The gross tumour volume (GTV_{APBI}) was contoured using preoperative diagnostic imaging, preoperative MRI in treatment position, surgical clips, and possible postoperative seroma. A 15 mm margin in all directions was applied to the GTV_{APBI} to generate the clinical target volume (CTV_{APBI}), while excluding the chest wall and skin. The PTV_{APBI} was delineated as the CTV_{APBI} with a 5 mm margin, while excluding the skin (figure 2). The median PTV_{APBI} was 148 cc (range: 88 – 248 cc). For both WBI and APBI, the delineated OARs were the heart, lungs, contralateral breast, body (comprising all unspecified tissue) and the skin (figure 2). The skin considered for the analysis of the impact of the ERE was defined to be the first 5 mm under the surface of the ipsilateral breast. It was further extended up to 35 mm in anterior, posterior, medial, and lateral directions relative to the PTV_{WBI} in order to include skin tissue expected to be irradiated in WBI-2 (figure 2). An extension of 15 mm was made in the caudal and cranial directions to include skin tissue receiving scattered dose. The median volume of the skin was 318 cc (range: 256 – 474 cc).

Specially developed MRL treatment planning software (MRLTP) was used to generate IMRT plans while taking into account the presence of a magnetic field. MRLTP is a combination of GPUMCD – which is a Graphics Processing Unit (GPU)-oriented Monte Carlo dose calculation algorithm as described by Hissoiny *et al.* [19] – and the Central Processing Unit (CPU)-based Fast Inverse Dose Optimization (FIDO) as described by Goldman *et al.* [20]. A more detailed description of this system can be found in Bol *et al.* [21]. FIDO has the distinct advantage that the optimization process is executed within a short time frame. The MRL's



● *Figure 2 Transversal slice of a patient CT scan with VOIs delineated: PTV_{WBI} (red contour), GTV_{APB1} (purple), PTV_{APB1} (bright green), ipsilateral lung (yellow), contralateral lung (dark green), heart (sky blue), unspecified tissue (dark blue), contralateral breast (brown), and skin (orange, filled here with light grey). An extension made to the skin is visible here in the medial and lateral directions relative to the PTV_{WBI} , as indicated by the white oval-shaped markings. The location of the isocentre is marked by the crosshair.*

characteristics are incorporated in the MRLTP. The 6 MV photon beam can rotate in full 360 degrees around the patient with maximum field sizes of 24 cm in caudo-cranial direction and 56 cm in anterior-posterior direction. As a consequence, the isocentre is fixed, at 14 cm above the treatment table. The isocentre-source distance is 142.7 cm. With MRLTP, plans can be generated at any magnetic-field strength required. IMRT plans were generated for 0 T and 1.5 T, which is the field strength in the MRL. Also, plans were calculated at the intermediate value of 0.35 T. For each IMRT technique (WBI-2, WBI-7, APBI-7) a class solution of optimization objectives was developed at 0 T, which was then applied for all patients. These sets of objectives were unaltered when applied at higher field strengths. The plans were based on the fully optimized fluence maps with a 5 mm grid resolution and the acquired dose distributions consisted of $2 \times 2 \times 2 \text{ mm}^3$ voxels.

Comparison of plans

For the comparison of the plans, dose volume histograms (DVHs) for all VOIs and corresponding dose parameters were calculated. For the PTV the $D_{95\%}$ - the percentage of the PTV receiving at least 95% of the prescribed dose - to describe PTV coverage, and the $D_{107\%}$, describing the amount of overdose, were calculated. The starting point of the plan comparisons was a similar $D_{95\%}$ and $D_{107\%}$.

Several parameters were compared for the OARs. The mean lung dose (MLD) over two lungs was computed, which was to be a maximum of 7 Gy. For the ipsilateral lung, $V_{10\text{Gy}}$ - the fraction of the volume receiving 10 Gy or more -, $V_{20\text{Gy}}$ and $V_{30\text{Gy}}$ were derived for the WBI plans while for APBI the $V_{5\text{Gy}}$, $V_{10\text{Gy}}$ and $V_{20\text{Gy}}$ were found. Similar parameters were calculated for the heart. Moreover, the $D_{2\text{cc}}$ - maximum dose encompassing 2 cc of the structure - was calculated for the heart as an indication of the maximum dose. The range 30-40 Gy is considered to be relevant for the skin dose, so the mean dose and parameters $V_{35\text{Gy}}$ and $D_{2\text{cc}}$ were calculated for the skin. For the $V_{35\text{Gy}}$, box-whisker plots are derived to determine how the values at different magnetic-field strengths are distributed. Also, the $D_{2\text{cc}}$ of the unspecified tissue (body) and the mean dose of the contralateral breast were acquired, both of which were to be kept low. The statistical significance of differences between all dosimetric parameters was tested by performing a paired student's *t*-test. A value of $p < 0.05$ was considered to represent a statistically significant result.

Additionally, dose-difference maps for all plans were derived, which depict for the same patient the dose differences per voxel relative to the situation at 0 T, i.e. dose values at 0.35 T versus 0 T and at 1.5 T versus 0 T. This allows further analysis of the spatial distribution of any dose differences caused by the magnetic field.

Results

Optimization process

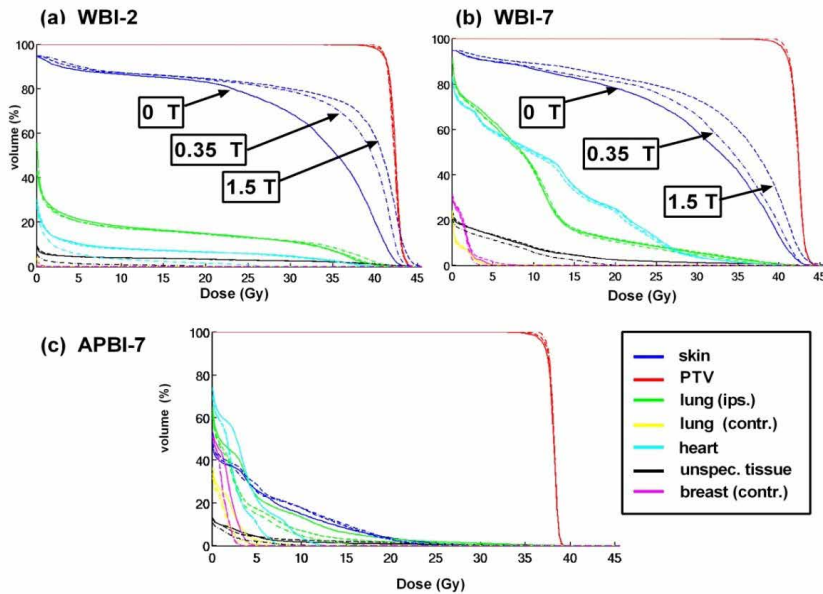
IMRT plans were successfully generated using MRLTP. The time required to calculate the Monte Carlo beamlets varied with size of the PTV, the number of beam angles and the magnetic-field strength (i.e. number of electron steps). For this, a computer with 4 GB RAM, a 2.27 GHz CPU, and a GeForce GX 580 GPU was used. Beamlet calculations for a WBI-2 plan took 15 minutes at 0 T which went up to 25 minutes at 1.5 T, while a typical WBI-7 set-up took 40 minutes for 0 T and up to an hour for a 1.5 T plan. Calculating beamlets for APBI-7 typically took 20 minutes for a 0 T plan, up to 25 minutes for a plan at 1.5 T.

For each of the three RT techniques, a class solution of objectives was employed for the optimization of all plans. Once a suitable template of objective parameters was found for one patient, an automated script was activated to apply it for optimizing the plans of all other patients. Some individual plans required additional optimization. With the use of a 32 GB RAM, 3.40 GHz, eight-core CPU, the optimization time of FIDO for a WBI-2 plan or an APBI-7 plan was typically in the order of a few seconds, while a WBI-7 plan took only half a minute to optimize.

Induced effects for WBI-2

At the three different magnetic-field strengths 0 T, 0.35 T and 1.5 T, similar target coverage is achieved. Furthermore, no target overdose is observed (table 1).

Relative to the situation at 0 T, the mean skin dose in WBI-2 is raised by 9.5% ($p < 0.01$) and 12.5% ($p < 0.01$) at 0.35 T and 1.5 T, respectively (table 1). This dose increase is clearly visible in a typical DVH and dose-difference maps as shown in figure 3(a) and figure 4(a,b), respectively. It can also be observed in figure 4(a,b) that the increase in skin dose is especially manifested at the most superficial voxels of the skin. The most significant change in dose distribution in the skin is found in the range of around 30-40 Gy (figure 3(a)). Further analysis shows that the ERE causes the skin volume receiving more than 35 Gy ($V_{35\text{Gy}}$) at both non-zero



● Figure 3 DVHs at different field strengths, 0 T (full), 0.35 T (dash-dotted), and 1.5 T (dashed), acquired from the plans for one typical patient. For each separate RT technique, (a) WBI-2; (b) WBI-7; (c) APBI-7, the PTV and OARs, including the skin, are shown. See legend for colour specifications. Here, “ips.” = ipsilateral, “contr.” = contralateral, “unspec. tissue” = all unspecified tissue. For WBI, the skin at different magnetic-field strengths is also indicated by arrows with corresponding text boxes. Prescribed dose for WBI and APBI was 42.56 Gy and 38.5 Gy, respectively.

magnetic-field strengths to increase considerably. This can be observed in the box-whisker plot in figure 5(a), where the whiskers of the boxes of $V_{35\text{Gy}}$ at both 0.35 T and 1.5 T do not overlap with those at 0 T, indicating significant differences ($p < 0.01$). Also, the maximum skin dose ($D_{2\text{cc}}$) is slightly raised, with an increase of 2.3 Gy at 1.5 T compared to no magnetic field (table 1).

The mean lung dose (MLD) in WBI-2 is low (~ 3.0 Gy) and unaffected by the magnetic field (table 1). This is also true for the $V_{10\text{Gy}}$ of the ipsilateral lung. However, it receives more high dose at increasing field strength as indicated by the $V_{30\text{Gy}}$ going up by 2.2% ($p < 0.01$) at 1.5 T relative to 0 T. This high-dose volume can also be observed in the dose-difference maps of figure 4(a,b). The heart dose is unaffected by the presence of the magnetic field in WBI-2. Both the $V_{25\text{Gy}}$ and $D_{2\text{cc}}$ of the heart remain constant. This is also true for the contralateral-breast mean dose, which remains very low.

The unspecified tissue receives a higher dose locally as indicated by the D_{2cc} which is on average 1.2 Gy more ($p = 0.02$) at 1.5 T than at 0 T (table 1).

Induced effects for WBI-7

Similar target coverage is achieved for all patients in WBI-7 at all field strengths and, again, no target overdoses are observed (table 1).

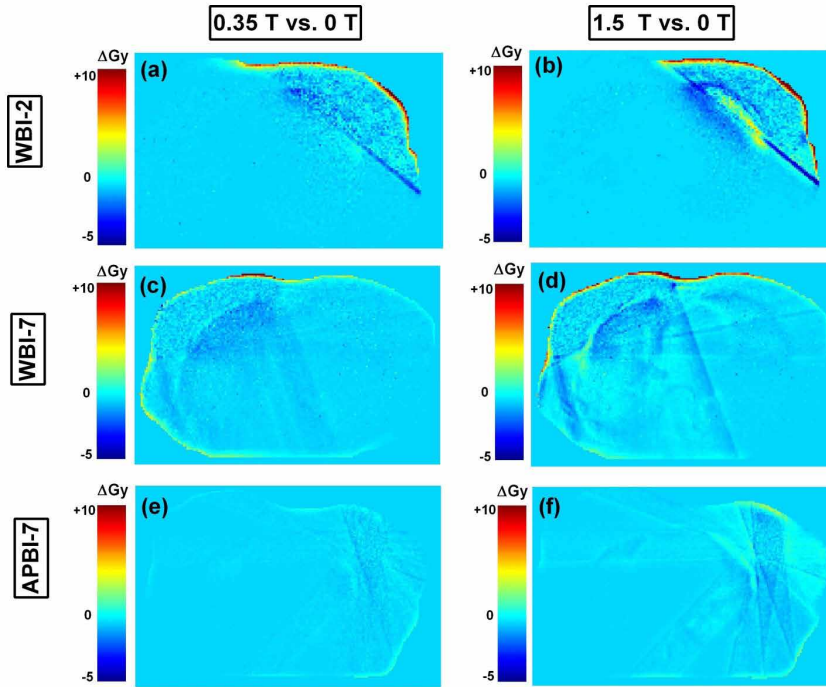
Although the mean skin dose in WBI-7 is lower than in WBI-2, it is raised by the ERE. This augmentation, relative to the 0 T situation, is on average 8.2% ($p < 0.01$) and 6.8% ($p < 0.01$) at 0.35 T and 1.5 T, respectively (table 1). The fact that this increase is less severe than in WBI-2 can be seen in the typical DVH example in figure 3(b) and the dose-difference maps of figure 4(c,d). The principle change in skin dose is in the range of around 30-40 Gy, which was also observed for WBI-2. Indeed, V_{35Gy} is increased considerably ($p < 0.01$) at 0.35 T and at 1.5 T. This can also be seen in the box-whisker plot in figure 5(b), where the interquartile ranges (height of the boxes) of V_{35Gy} , at both 0.35 T and at 1.5 T, do not overlap with those at 0 T, indicating that there is a significant difference between the medians. It nevertheless shows a smaller increase compared to the tangential technique. The D_{2cc} of the skin is similar to that in WBI-2 and is in presence of a magnetic field raised by a similar amount (table 1).

The MLD in WBI-7 is higher than in WBI-2 and is increased with respectively 0.6 Gy and 0.7 Gy at 0.35 T and 1.5 T (table 1). The volumes of the ipsilateral lung receiving at least 10 Gy and 20 Gy, respectively, are larger than in WBI-2 and remain almost constant. However, the V_{30Gy} is smaller relative to WBI-2, and is only enlarged from on average 3.5% ($p = 0.17$) at 0 T to 3.9% ($p = 0.11$) at 1.5 T. Due to the beam orientation in WBI-7, the V_{25Gy} and D_{2cc} for the heart and mean dose of the contralateral breast are higher than for WBI-2, but they remain constant with increasing magnetic-field strengths. Also, the maximum dose indicated by D_{2cc} of the unspecified tissue is increased with on average only 0.2 Gy more ($p = 0.02$) at 1.5 T than at 0 T (table 1). This effect is smaller relative to WBI-2 (figure 4(c,d)).

● *Table 1 Dose parameters calculated for WBI-2 (columns 2-4) and WBI-7 (columns 5-7), at 0 T, 0.35 T, and 1.5 T, respectively, for all breast tumours (n = 11). Prescription was 16 x 2.66 Gy = 42.56 Gy. Values are denoted as: 'mean (standard deviation)'.*

<i>Dose parameter</i>	WBI-2			WBI-7		
	0 T	0.35 T	1.5 T	0 T	0.35 T	1.5 T
PTV						
$D_{95\%}$ (%)	96.5 (0.5)	96.7 (0.7)	96.7 (0.6)	95.9 (0.6)	96.1 (0.7)	96.1 (0.7)
$D_{107\%}$ (%)	0.0 (0.0)	0.0 (0.1)	0.0 (0.1)	0.1 (0.3)	0.1 (0.3)	0.1 (0.2)
Ips. lung						
MLD (Gy)	2.9 (0.9)	3.0 (0.9)	3.0 (0.9)	5.2 (1.1)	5.8 (1.1)	5.9 (1.1)
$V_{10\text{Gy}}$ (%)	16.7 (4.9)	16.2 (4.8)	16.2 (4.7)	36.0 (7.7)	35.5 (7.6)	36.6 (7.8)
$V_{20\text{Gy}}$ (%)	13.6 (4.5)	13.5 (4.5)	13.6 (4.4)	17.3 (7.3)	17.2 (7.0)	17.4 (6.9)
$V_{30\text{Gy}}$ (%)	7.1 (3.7)	8.1 (3.8)	9.3 (3.8)	3.5 (3.1)	3.7 (3.2)	3.9 (3.1)
Heart						
$D_{2\text{cc}}$ (Gy)	20.5 (18.6)	20.2 (18.5)	19.9 (18.5)	28.3 (9.2)	28.3 (9.1)	28.2 (9.0)
$V_{25\text{Gy}}$ (%)	1.5 (2.0)	1.4 (2.0)	1.4 (2.0)	3.4 (4.3)	3.1 (3.9)	3.2 (4.1)
Unspecified tissue						
$D_{2\text{cc}}$ (Gy)	46.0 (2.7)	46.7 (2.7)	47.2 (2.8)	45.0 (2.3)	45.0 (2.4)	45.2 (2.4)
Contr. breast						
Mean (Gy)	0.2 (0.3)	0.2 (0.3)	0.2 (0.3)	3.3 (1.7)	3.1 (1.6)	3.2 (1.7)
Skin						
$D_{2\text{cc}}$ (Gy)	43.3 (0.6)	44.6 (1.0)	45.6 (1.1)	43.3 (0.3)	44.4 (1.4)	45.6 (2.9)
Mean (Gy)	29.5 (1.4)	32.3 (1.6)	33.2 (1.7)	27.9 (1.4)	30.2 (1.7)	29.8 (1.3)

$D_{95\%}$ = fraction of the volume receiving at least 95% of the prescribed dose, or 40.43 Gy;
 $D_{107\%}$ = fraction of the volume receiving at least 107% of the prescribed dose, or 45.54 Gy;
 Ips. lung = ipsilateral lung; MLD = mean lung dose (over both lungs); $V_{X\text{Gy}}$ = fraction of volume receiving at least X Gy; $D_{2\text{cc}}$ = dose received by 2 cc of the structure; Contr. breast = contralateral breast.

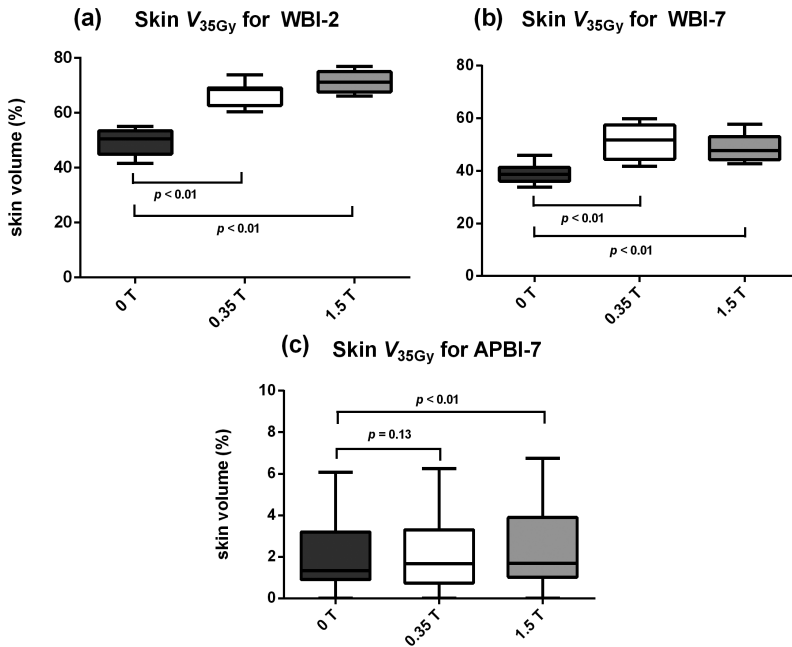


● Figure 4 Maps of dose differences (in Gy) per voxel relative to the situation of no magnetic field. Examples of transversal slices are depicted in each consecutive row for each RT technique on three different patients, while the different magnetic-field strengths are arranged per column, i.e. (a) WBI-2 at 0.35 T vs. 0 T; (b) WBI-2 at 1.5 T vs. 0 T; (c) WBI-7 at 0.35 T vs. 0 T; (d) WBI-7 at 1.5 T vs. 0 T; (e) APBI-7 at 0.35 T vs. 0 T; (f) APBI-7 at 1.5 T vs. 0 T. Voxel size is $2 \times 2 \times 2 \text{ mm}^3$. Differences range from -5 Gy (dark blue) to +10 Gy (dark red).

Induced effects for APBI-7

For the APBI-7 plans, similar dose coverage is achieved for all magnetic-field values. Furthermore, no overdose is observed for the three situations (table 2).

The impact of the ERE on the skin dose is less prominent in APBI than in WBI. The mean skin dose in APBI-7 is low when compared to the WBI techniques and is only slightly raised when a magnetic field is present (table 2). This can also be observed in the typical DVH in figure 3(c) and is also reflected in the dose-difference maps of figure 4(e,f). Since the skin dose is already observed to be low, the $V_{35\text{Gy}}$ for the skin in APBI-7 is low and does not increase considerably (figure 5(c)). This can be clearly seen by the boxes of $V_{35\text{Gy}}$ at 0.35 T and at 1.5 T both largely overlapping with the



● Figure 5 Box-whisker plots of the skin dose parameter V_{35Gy} , as obtained from all plans (11 breast tumours). The box whiskers are represented for (a) WBI-2; (b) WBI-7; (c) APBI-7. They are evaluated for field strengths 0 T (dark grey), 0.35 T (white), and 1.5 T (light grey). The line in each box represents the median; the lower and upper quartiles determine the height of each box – or interquartile range; the minimum and maximum values are represented by the whiskers. The p -values acquired from the student's paired t-test are depicted to indicate significances relative to 0 T.

box at 0 T ($p = 0.13$ and $p < 0.01$, respectively). Although the increase at 1.5 T is significant, it does not reflect a clinically relevant difference since the absolute change is very small. The maximum skin dose (D_{2cc}) is lower when compared to WBI and remains unchanged at non-zero magnetic-field strengths (table 2).

The MLD in APBI-7 is low (~ 2 Gy) and remains almost constant for non-zero field strengths. Furthermore, there are no observed significant differences ($p > 0.05$) in the presence of a magnetic field in the V_{5Gy} and V_{10Gy} of the ipsilateral lung, while also the V_{20Gy} remains unchanged. The V_{5Gy} , V_{10Gy} , and D_{2cc} of the heart in APBI-7 remain constant relative to 0 T at both 0.35 T and 1.5 T ($p > 0.05$ for all parameter differences). The heart V_{25Gy} stays zero in APBI-7 (not given in table 2). Relative to WBI, the mean dose of the contralateral breast remains low, whereas the unspecified

tissue D_{2cc} seems to be raised slightly. The maximum raise is 0.5 Gy at 1.5 T compared to 0 T, however, this is statistically insignificant ($p = 0.17$). Small increases are visible in the dose-difference maps in figure 4(e,f).

● *Table 2 Dose parameters calculated for APBI-7 at 0 T, 0.35 T, and 1.5 T, respectively, for all breast tumours ($n = 11$). Prescription was 10×3.85 Gy = 38.5 Gy. Values are denoted as: 'mean (standard deviation)'.*

Dose parameter	APBI-7		
	0 T	0.35 T	1.5 T
PTV			
$D_{95\%}$ (%)	97.0 (0.5)	97.0 (0.5)	97.0 (0.7)
$D_{107\%}$ (%)	0.0 (0.0)	0.0 (0.0)	0.0 (0.0)
Ips. lung			
MLD (Gy)	2.1 (1.0)	2.0 (1.0)	1.8 (0.8)
V_{3Gy} (%)	25.1 (12.9)	23.1 (12.6)	20.3 (9.6)
V_{10Gy} (%)	10.3 (6.1)	9.8 (7.1)	8.0 (4.5)
V_{20Gy} (%)	2.3 (1.5)	2.3 (1.6)	1.9 (1.3)
Heart			
D_{2cc} (Gy)	6.9 (2.5)	6.2 (2.0)	5.8 (2.5)
V_{3Gy} (%)	8.0 (13.3)	6.2 (10.2)	6.0 (10.9)
V_{10Gy} (%)	0.4 (1.2)	0.0 (0.0)	0.0 (0.0)
Unspecified tissue			
D_{2cc} (Gy)	37.9 (0.5)	38.2 (0.6)	38.4 (0.7)
Contr. breast			
Mean (Gy)	1.1 (0.5)	1.0 (0.4)	1.4 (0.6)
Skin			
D_{2cc} (Gy)	35.5 (4.7)	35.2 (4.9)	35.6 (4.4)
Mean (Gy)	5.2 (2.1)	5.6 (2.4)	5.8 (2.4)

$D_{95\%}$ = fraction of the volume receiving at least 95% of the prescribed dose, or 36.6 Gy; $D_{107\%}$ = fraction of the volume receiving at least 107% of the prescribed dose, or 41.2 Gy; *Ips. lung* = ipsilateral lung; MLD = mean lung dose (over both lungs); V_{XGy} = fraction of volume receiving at least X Gy; D_{2cc} = dose received by 2 cc of the structure; *Contr. breast* = contralateral breast.

Discussion

The results of this treatment-planning study show effects on the dose distribution when treating breast-cancer patients with a 6 MV photon beam in presence of a magnetic field. The induced dosimetric effects on the skin are observed at 0.35 T and 1.5 T. A significant increase in skin dose is observed when conventional treatment by tangential-field WBI is performed. This observation could impair the clinical acceptability of the plans in the MRL. Therefore, a seven-field WBI technique was introduced, in an attempt to reduce the skin dose, as predicted in a previous film-based phantom study [22], although the other OARs would receive more dose than with the tangential technique. However, an increase in skin dose is observed there as well. For the APBI technique, the impact on the skin dose is small in comparison with WBI.

Doses to the OARs in WBI are comparable to those from other studies in the 0 T cases [23–26] except for the $V_{20\text{Gy}}$ of the ipsilateral lung in WBI-7, which is relatively high. Differences in the dose distribution between the WBI-2 and WBI-7 techniques are mainly in the low-dose regions of the OARs as a consequence of the different beam orientations, and in the high-dose region of the ipsilateral lung. Although the MLD is higher in seven-field WBI, the high-dose volume is smaller compared to the tangential set-up, since in the tangential plans the dose is less conformal near the lung. In the seven-field set-up the mean skin dose is lower relative to the tangential-field technique. However, a magnetic-field-induced effect was still observed, thus the plans were clinically not better than for the tangential technique.

In APBI, the observed effects on the skin dose are found to be negligible in presence of a magnetic field. Moreover, the absolute dose values on the other OARs are low relative to WBI and comparable to values found in other studies at 0 T [25,27], while it should be kept in mind that the fractionation in APBI is different from WBI. Since the OAR doses are not affected adversely under influence of the magnetic field, it can be concluded that the performance of APBI treatments in the MRL is not impaired by the ERE.

Current cosmetic outcome for treatments by WBI after BCS is good to excellent [17,18,28,29]. For APBI, at least in the studies by Lewin *et al.* [7] and Shaikh *et al.* [8], the current cosmetic outcome was shown to be good to excellent. With regard to the skin dose, the presence of the magnetic field is clearly disadvantageous for WBI. Further increases to the skin dose could result in a higher complication rate and severity of complications [30]. The actual clinical implications of the observed raised skin dose – especially in the regions receiving 30-40 Gy or more – have to be investigated further, since precise data and calculations on the biological effects of high skin dose are unavailable. However, negative side effects induced by high skin dose are observed [31–33], implying a potential drawback when considering the performance of WBI treatments in the MRL.

A fluence-based optimization process is used in MRLTP to optimize the dose distribution, which means that the sequencing step for actual dose delivery is not included. Thus, any quality degradation of the plan caused by a sequencer is omitted. The aim of our study, however, was to investigate the induced physical influences on the dose caused by the magnetic field. Although the absolute dose values may differ slightly when including a sequencer, the physical effects on the skin dose in general are already reflected in the dose plans.

The highest dose increases in the skin were observed in the most superficial layer of the skin (figure 4). In our analysis a voxel size of $2 \times 2 \times 2 \text{ mm}^3$ was used. Further investigation of the magnetic-field-induced effects on the dose distribution with a higher-resolution dose grid was performed by Oborn *et al.* [34]. In specific phantom set-ups, layers of tiny voxels (in the order of $10 \text{ }\mu\text{m}$ per voxel) were constructed and analysed for a 6 MV photon spectrum and a range of magnetic-field strengths (0-3.0 T) using Monte Carlo simulations. It was shown that at non-zero magnetic fields the first $70 \text{ }\mu\text{m}$ under the surface receive a larger increase in skin dose than what was to be expected based on lower-resolution calculations. As a consequence, there is a possibility that even in APBI treatments, a dose peak may appear in the top layers of the skin. This should be properly measured and monitored extensively before the clinical implementation of APBI treatments in the MRL. Moreover, it was shown in Monte Carlo dose calculations [35] that the contribution of contaminant electrons to both the entry dose and entry-surface dose can cause an increase at 0 T.

However, this effect is again limited to about the first 70 μm of the tissue. Contaminant electrons are not incorporated in the MRLTP.

The current study was based on static-image treatment-planning, which means that effects due to intra-fraction movements are not accounted for. However, Frazier *et al.* showed that dose plans for WBI are relatively insensitive to the effects of breast motion during normal breathing [36]. Furthermore, in a study by George *et al.* [37] it was concluded that there were no significant effects observed in the IMRT delivery when respiratory motion is compensated for in breast RT. Additionally, the MRL is primarily designed for tracking the target volume and performing dynamic planning, thus compensating for all motion.

The added value of MRI for breast RT in the MRL will especially be the visualization of the tumour bed in high contrast to the surrounding anatomy. For WBI alone, the breast boundaries can also be visualized with other modalities such as kV or MV radiographs. However, the purpose of the research was to investigate the dosimetric effects of the magnetic field on RT treatments, including the standard technique of WBI, which involves relatively large field sizes. This can be of special relevance when WBI is to be performed in the MRL in combination with, for example, the delivery of a (stereotactic) boost. In future studies, more novel treatments in the MRL will be investigated as well. A single modality which can perform both standard and more sophisticated RT techniques at once could lead to a very high efficiency in the treatment of the patient.

The use of MRI allows for very precise RT performances in the MRL, from which breast-cancer patients could potentially benefit. However, from the previous discussion we find that the direct application in the MRL of currently standard treatments such as WBI is not straightforward. In both tangential and seven-field WBI, the skin-dose increase caused by the ERE is probable to cause negative side effects, which implies a potential drawback for those treatments. On the other hand, in the APBI set-up considered, negative side effects are much more unlikely, which makes APBI in the MRL feasible. APBI treatments could fully benefit from the capabilities of MRI, such as the high soft-tissue contrast, enabling direct, on-line position verification of the target area itself. This opens new possibilities for developing novel treatment techniques for breast cancer, aiming directly at

the primary tumour location [38]. Therefore, our future research will focus on MR-guided partial-breast treatments.

Conclusions

The treatment of patients in the MRL using a conventional tangential WBI set-up or a seven-field WBI technique, at 0.35 T or 1.5 T, implies an increase in skin dose of the ipsilateral breast. In APBI treatments the skin dose and other OAR doses are relatively low and only minimally affected by the magnetic field. This opens new possibilities for developing MR-guided partial-breast treatment techniques in the MRL.

References

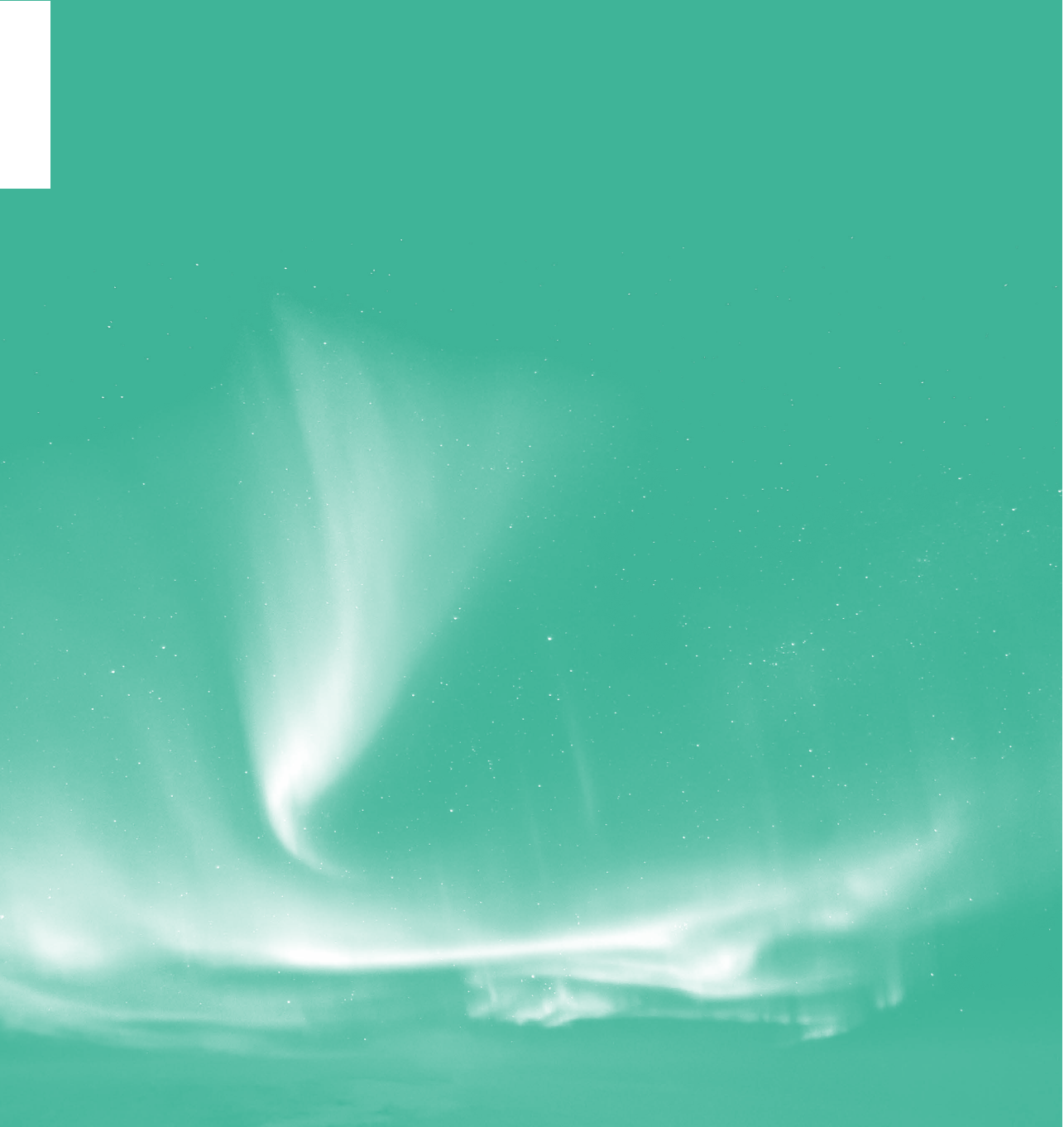
- [1] Raaymakers BW, Lagendijk JJW, Overweg J, Kok JGM, Raaijmakers AJE, Kerkhof EM, et al. Integrating a 1.5 T MRI scanner with a 6 MV accelerator: proof of concept. *Phys Med Biol* 2009;54:N229–37. doi:10.1088/0031-9155/54/12/N01.
- [2] Fallone BG, Murray B, Rathee S, Stanescu T, Steciw S, Vidakovic S, et al. First MR images obtained during megavoltage photon irradiation from a prototype integrated linac-MR system. *Med Phys* 2009;36:2084–8.
- [3] Dempsey J, Dionne B, Fitzsimmons J, Haghigat A, Li J, Low D, et al. WE-E-ValA-06: A Real-Time MRI Guided External Beam Radiotherapy Delivery System. *Med Phys* 2006;33:2254. doi:10.1118/1.2241803.
- [4] Oliver M, Chen J, Wong E, Van Dyk J, Perera F. A treatment planning study comparing whole breast radiation therapy against conformal, IMRT and tomotherapy for accelerated partial breast irradiation. *Radiother Oncol* 2007;82:317–23. doi:10.1016/j.radonc.2006.11.021.
- [5] Njeh CF, Saunders MW, Langton CM. Accelerated Partial Breast Irradiation (APBI): A review of available techniques. *Radiat Oncol* 2010;5:90. doi:10.1186/1748-717X-5-90.
- [6] Livi L, Buonamici FB, Simontacchi G, Scotti V, Fambrini M, Compagnucci A, et al. Accelerated partial breast irradiation with IMRT: new technical approach and interim analysis of acute toxicity in a phase III randomized clinical trial. *Int J Radiat Oncol Biol Phys* 2010;77:509–15. doi:10.1016/j.ijrobp.2009.04.070.
- [7] Lewin A a, Derhagopian R, Saigal K, Panoff JE, Abitbol A, Wieczorek DJ, et al. Accelerated partial breast irradiation is safe and effective using intensity-modulated radiation therapy in selected early-stage breast cancer. *Int J Radiat Oncol Biol Phys* 2012;82:2104–10. doi:10.1016/j.ijrobp.2011.02.024.
- [8] Shaikh AY, LaCombe M a, Du H, Raghavan VT, Nanda RK, Bloomer WD. Accelerated partial breast irradiation using once-daily fractionation: analysis of 312 cases with four years median follow-up. *Radiat Oncol* 2012;7:17. doi:10.1186/1748-717X-7-17.
- [9] Fein DA, McGee KP, Schultheiss TE, Fowble BL, Hanks GE. Intra- and interfractional reproducibility of tangential breast fields: a prospective on-line portal imaging study. *Int J Radiat Oncol Biol Phys* 1996;34:733–40.
- [10] Jaffray DA, Siewerdsen JH, Wong JW, Martinez AA. Flat-panel cone-beam computed tomography for image-guided radiation therapy. *Int J Radiat Oncol Biol Phys* 2002;53:1337–49.
- [11] Whipp EC, Halliwell M. Magnetic resonance imaging appearances in the postoperative breast: the clinical target volume-tumor and its relationship to the chest wall. *Int J Radiat Oncol Biol Phys* 2008;72:49–57. doi:10.1016/j.ijrobp.2007.12.021.
- [12] Kirby AM, Yarnold JR, Evans PM, Morgan V a, Schmidt M a, Scurr ED, et al. Tumor bed delineation for partial breast and breast boost radiotherapy planned in the prone position: what does MRI add to X-ray CT localization of titanium clips placed in the excision cavity wall? *Int J Radiat Oncol Biol Phys* 2009;74:1276–82. doi:10.1016/j.ijrobp.2009.02.028.
- [13] Giezen M, Kouwenhoven E, Scholten AN, Coerkamp EG, Heijnenbrok M, Jansen WPA, et al. Magnetic resonance imaging-versus computed tomography-based target volume delineation of the glandular breast tissue (clinical target volume breast) in breast-conserving therapy: An exploratory study. *Int J Radiat Oncol Biol Phys* 2011;81:804–11.

- [14] Sabine B, Giovanna D, Peter P, Clara J, Bert P, John K. Open Low-Field Magnetic Resonance (MR) Versus CT Scanner (CT) Imaging in Breast Radiotherapy Treatment Planning. *Int J Radiat Oncol* 2005;63:S232–3. doi:10.1016/j.ijrobp.2005.07.397.
- [15] Raaijmakers AJE, Raaymakers BW, Lagendijk JJW. Integrating a MRI scanner with a 6 MV radiotherapy accelerator: dose increase at tissue-air interfaces in a lateral magnetic field due to returning electrons. *Phys Med Biol* 2005;50:1363–76. doi:10.1088/0031-9155/50/7/002.
- [16] Raaijmakers AJE, Raaymakers BW, van der Meer S, Lagendijk JJW. Integrating a MRI scanner with a 6 MV radiotherapy accelerator: impact of the surface orientation on the entrance and exit dose due to the transverse magnetic field. *Phys Med Biol* 2007;52:929–39. doi:10.1088/0031-9155/52/4/005.
- [17] Taylor ME, Perez CA, Halverson KJ. Factors influencing cosmetic results after conservation therapy for breast cancer 1995;31:753–64.
- [18] Munshi A, Kakkar S, Bhutani R, Jalali R, Budrukkar A, Dinshaw KA. Factors influencing cosmetic outcome in breast conservation. *Clin Oncol (R Coll Radiol)* 2009;21:285–93. doi:10.1016/j.clon.2009.02.001.
- [19] Hissoiny S, Ozell B, Bouchard H, Després P. GPUMCD: A new GPU-oriented Monte Carlo dose calculation platform. *Med Phys* 2011;38:754–64. doi:10.1118/1.3539725.
- [20] Goldman SP, Turnbull D, Johnson C, Chen JZ, Battista JJ. Real-time fast inverse dose optimization for image guided adaptive radiation therapy—Enhancements to fast inverse dose optimization (FIDO). *J Appl Phys* 2009;105:102008. doi:10.1063/1.3115640.
- [21] Bol GH, Hissoiny S, Lagendijk JJW, Raaymakers BW. Fast online Monte Carlo-based IMRT planning for the MRI linear accelerator. *Phys Med Biol* 2012;57:1375–85. doi:10.1088/0031-9155/57/5/1375.
- [22] Almberg SS, Lindmo T, Frengen J. Superficial doses in breast cancer radiotherapy using conventional and IMRT techniques: a film-based phantom study. *Radiother Oncol* 2011;100:259–64. doi:10.1016/j.radonc.2011.05.021.
- [23] Hong L, Hunt M, Chui C, Spirou S, Forster K, Lee H, et al. Intensity-modulated tangential beam irradiation of the intact breast. *Int J Radiat Oncol Biol Phys* 1999;44:1155–64.
- [24] Popescu CC, Olivotto I, Patenaude V, Wai E, Beckham W a. Inverse-planned, dynamic, multi-beam, intensity-modulated radiation therapy (IMRT): a promising technique when target volume is the left breast and internal mammary lymph nodes. *Med Dosim* 2006;31:283–91. doi:10.1016/j.meddos.2006.05.003.
- [25] Moran JM, Ben-David MA, Marsh RB, Balter JM, Griffith KA, Hayman JA, et al. Accelerated partial breast irradiation: what is dosimetric effect of advanced technology approaches? *Int J Radiat Oncol Biol Phys* 2009;75:294–301. doi:10.1016/j.ijrobp.2009.03.043.
- [26] Johansen S, Cozzi L, Olsen DG. A planning comparison of dose patterns in organs at risk and predicted risk for radiation induced malignancy in the contralateral breast following radiation therapy of primary breast using conventional, IMRT and Volumetric modulated arc treatment techniqu. *Acta Oncol (Madr)* 2009:495–503.
- [27] Moon SH, Shin KH, Kim TH, Yoon M, Park S, Lee D-H, et al. Dosimetric comparison of four different external beam partial breast irradiation techniques: three-dimensional conformal radiotherapy, intensity-modulated radiotherapy, helical tomotherapy, and proton beam therapy. *Radiother Oncol* 2009;90:66–73. doi:10.1016/j.radonc.2008.09.027.
- [28] Vrieling C, Collette L, Fourquet A, Hoogenraad WJ, Horiot JH, Jager JJ, et al. The influence of patient, tumor and treatment factors on the cosmetic results after breast-conserving therapy in the EORTC “boost vs. no boost” trial. *EORTC Radiotherapy and Breast Cancer Cooperative Groups. Radiother Oncol* 2000;55:219–32.

- [29] Immink JM, Putter H, Bartelink H, Cardoso JS, Cardoso MJ, van der Hulst-Vijgen MH V, et al. Long-term cosmetic changes after breast-conserving treatment of patients with stage I-II breast cancer and included in the EORTC “boost versus no boost” trial. *Ann Oncol* 2012;23:2591–8. doi:10.1093/annonc/mds066.
- [30] Mukesh M, Harris E, Jena R, Evans P, Coles C. Relationship between irradiated breast volume and late normal tissue complications: a systematic review. *Radiother Oncol* 2012;104:1–10. doi:10.1016/j.radonc.2012.04.025.
- [31] Hopewell JW. The skin: its structure and response to ionizing radiation. *Int J Radiat Biol* 1990;57:751–73.
- [32] Kurtz JM. I Review article Impact of radiotherapy on breast cosmesis 1995:163–9.
- [33] Archambeau JO, Pezner R, Wasserman T. Pathophysiology of irradiated skin and breast. *Int J Radiat Oncol Biol Phys* 1995;31:1171–85. doi:10.1016/0360-3016(94)00423-1.
- [34] Oborn BM, Metcalfe PE, Butson MJ, Rosenfeld AB. Monte Carlo characterization of skin doses in 6 MV transverse field MRI-linac systems: effect of field size, surface orientation, magnetic field strength, and exit bolus. *Med Phys* 2010;37:5208–17. doi:10.1118/1.3488980.
- [35] Oborn BM, Metcalfe PE, Butson MJ, Rosenfeld AB. High resolution entry and exit Monte Carlo dose calculations from a linear accelerator 6 MV beam under the influence of transverse magnetic fields. *Med Phys* 2009;36:3549–59. doi:10.1118/1.3157203.
- [36] Frazier RC, Vicini FA, Sharpe MB, Yan D, Fayad J, Baglan KL, et al. Impact of breathing motion on whole breast radiotherapy: a dosimetric analysis using active breathing control. *Int J Radiat Oncol Biol Phys* 2004;58:1041–7. doi:10.1016/j.ijrobp.2003.07.005.
- [37] George R, Keall PJ, Kini VR, Vedam SS, Siebers J V., Wu Q, et al. Quantifying the effect of intrafraction motion during breast IMRT planning and dose delivery. *Med Phys* 2003;30:552. doi:10.1118/1.1543151.
- [38] Schmitz AC, Pengel KE, Loo CE, van den Bosch MAAJ, Wesseling J, Gertenbach M, et al. Pre-treatment imaging and pathology characteristics of invasive breast cancers of limited extent: potential relevance for MRI-guided localized therapy. *Radiother Oncol* 2012;104:11–8. doi:10.1016/j.radonc.2012.04.014.

“Always in motion is the future.”

Yoda



Quantification of intra-fraction motion in breast radiotherapy using supine MRI

Tristan C. F. van Heijst
Marielle E. P. Philippens
Ramona K. Charaghvandi
Mariska D. den Hartogh
Jan J. W. Lagendijk
H. J. G. Desirée van den Bongard
Bram van Asselen

Abstract

In early-stage breast-cancer patients, accelerated partial-breast irradiation techniques (APBI) and hypofractionation are increasingly implemented after breast-conserving surgery (BCS). For a safe and effective radiation therapy (RT), the influence of intra-fraction motion during dose delivery becomes more important as associated fraction durations increase and targets become smaller. Current image-guidance techniques are insufficient to characterize local target movement in high temporal and spatial resolution for extended durations. Magnetic resonance imaging (MRI) can provide high soft-tissue contrast, allow fast imaging, and acquire images during longer periods. The goal of this study was to quantify intra-fraction motion using MRI scans from 21 breast-cancer patients, before and after BCS, in supine RT position, on two time scales. High-temporal 2-dimensional (2D) MRI scans (cine-MRI), acquired every 0.3 s during 2 min, and three 3D MRI scans, acquired over 20 min, were performed. The tumour (bed) and whole breast were delineated on 3D scans and delineations were transferred to the cine-MRI series. Consecutive scans were rigidly registered and delineations were transformed accordingly. Motion in sub-second time-scale (derived from cine-MRI) was generally regular and limited to a median of 2 mm. Infrequently, large deviations were observed, induced by deep inspiration, but these were temporary. Movement on multi-minute scale (derived from 3D MRI) varied more, although medians were restricted to 2.2 mm or lower. Large whole-body displacements (up to 14 mm over 19 min) were sparsely observed. The impact of motion on standard RT techniques is likely small. However, in novel hypofractionated APBI techniques, whole-body shifts may affect adequate RT delivery, given the increasing fraction durations and smaller targets. Motion management may thus be required. For this, on-line MRI guidance could be provided by a hybrid MRI/RT modality, such as the University Medical Center Utrecht MRI linear accelerator.

Introduction

In early-stage breast-cancer patients, accelerated partial-breast irradiation (APBI) is currently being explored as an alternative to whole-breast irradiation (WBI), which is the standard treatment after breast-conserving surgery (BCS). APBI techniques aim to deliver a high dose solely to the tumour bed including the surrounding tissue, in fewer fractions relative to WBI, in order to reduce RT-associated toxicity and patient burden. Hypofractionated APBI has been shown to be effective in several studies [1–6]. Furthermore, the implementation of novel *preoperative* APBI (PAPBI) treatments is currently being investigated. First results of a clinical trial, and a phase-1 trial [7], showed low complication rates and good to excellent cosmetic outcome [5,8].

For a safe and effective dose delivery in APBI, both inter- and intra-fraction motion become increasingly relevant, as targets become smaller and consequently geometrical (partial) miss of the target more likely. Inter-fraction motion is induced by daily set-up errors. An accurate position verification strategy is thus required. Moreover, the duration of individual fractions will increase with a higher dose prescription per fraction, thereby increasing the relevance of intra-fraction motion. Movement during a fraction can primarily be caused by respiration and whole-body displacements [9]. Current image-guidance techniques used in breast RT include cone-beam computed tomography (CBCT), electronic portal imaging devices (EPID), and 3-dimensional (3D) surface imaging. Previous studies using these methods suggest that intra-fraction motion is generally limited to a maximum average of 5 mm during treatment, with large maximum deviations across patients, ranging up to several cm [10]. However, the actual extent of intra-fraction motion in APBI, during the entire fraction, cannot be inferred with these techniques. In CBCT, temporal resolution is limited due to the fact that images are usually acquired before and after irradiation. Conversely, the use of EPID allows sampling rates of two images/s. However, EPID imaging durations were limited to <15 s and only allow for visualization of projected anatomical structures, such as the thoracic wall. Moreover, 3D surface imaging only allows tracking of the outer anatomy contour.

In order to accurately characterize local target movement, a more suitable imaging technique is required. Magnetic resonance imaging (MRI) could enable this, since it provides superior soft-tissue contrast and potentially high temporal resolution, thereby allowing fast tumour (bed) visualization relative to the surrounding anatomy, in 2D and 3D, in high spatial resolution [11–13]. In the future, on-line adaptive MRI-guided RT strategies could be facilitated by a hybrid MRI/RT modality, such as the MRI linear accelerator (MRL), currently in development at the University Medical Center (UMC) in Utrecht, The Netherlands, which is specifically designed for target tracking and dynamic planning [14,15].

The goal of this study was to determine local intra-fraction target motion in breast RT using supine MRI in early-stage breast-cancer patients, on two temporal scales. Scans from both before and after BCS are analysed, in order to provide information for both postoperative RT techniques and novel preoperative hypofractionated APBI strategies.

Methods and materials

Patients

Written informed consent was obtained from 21 patients, who were included from the NTR3198 study. The study was approved by the Institutional Review Board of UMC Utrecht. Patients eligible for inclusion were diagnosed with early-stage breast cancer (T1-2N0M0 stage tumour) and scheduled for breast-conserving therapy, which consisted of BCS, followed by whole-breast RT. The median age of the women was 61 yr (range: 39 – 72 yr). One patient had tumours in both breasts, but for this study only the left-sided lesion was taken into account to ensure motion independence. In total, 9 of the tumours were left-sided, while 12 were in the right breast. The median volume of the ipsilateral breast was 802 cc (range: 476 – 3231 cc).

MRI scanning

Participants in the study underwent MRI for motion analysis on two temporal scales.

Patient set-up

MRI was performed in 21 patients before and 20 patients after BCS. All patients were scanned at the Radiology Department of UMC Utrecht, in 2011 or 2012. The first MRI scan was performed a median 6 days (range: 0 – 16 days) before BCS, while for the second scan the median time after BCS was 21 days (range: 14 – 50 days). MRI was performed on a 1.5 T Ingenia (Philips Medical Systems, Best, The Netherlands) wide-bore scanner. No breathing instructions were given. The subjects were scanned in RT position, i.e. supine with both arms in abduction, while lying on a 10° board. An anterior FlexCoverage receive coil (Philips, Best, The Netherlands) was used for data acquisition, which was placed on a custom-made adjustable bridge to prevent deformation of the outer contour of the patient. A posterior receive coil (Philips, Best, The Netherlands) was located in the MRI table. A more detailed description of the MRI scanning set-up, as used in this study, has been published previously (den Hartogh *et al.* 2014). The same MRI techniques were applied pre- and postoperatively, in all patients (table 1). However, not all patients completed all MRI scans on both occasions (table 2).

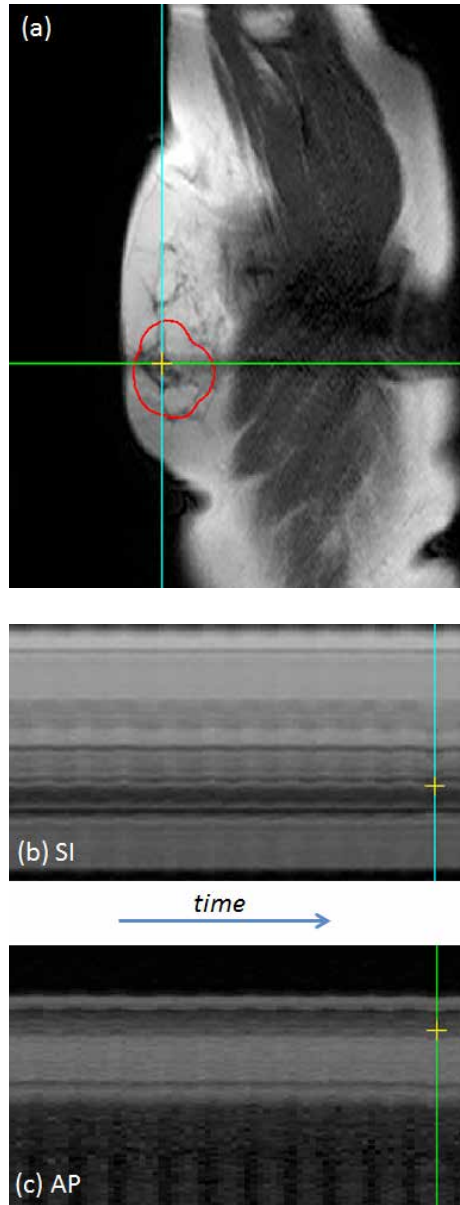
Cine-MRI for sub-second motion

The MRI scanning protocol included two dynamic two-dimensional (2D), balanced steady state free precession (bSSFP) series for analysis of sub-second motion, and is referred to as cine-MRI (figure 1). The slices were oriented through the tumour or tumour bed and orthogonal transverse and sagittal planes were acquired interleaved. Acquisition rate was 3.3 Hz, i.e. one scan in either orientation was acquired every 0.6 s. A complete series of 200 interleaved transverse and sagittal cine-MRI scans was obtained in 120 s.

● *Table 1 Imaging parameters of the MRI scans. In-plane FOV of the cine-MRI was 400 x 300 mm², while the average FOV of the 3D scans was 250 x 500 x 200 mm³, in anterior-posterior (AP), left-right (LR), and superior-inferior (SI) orientations. The 3D scans were reconstructed using overcontiguous slices.*

<i>Imaging parameters</i>					
<i>Sequences</i>	cine-MRI	T2-FSE	T1-FFE	DCE-MRI	
<i>Type of sequence</i>	SSFP	FSE	SPGR	SPGR	
<i>Weighting</i>	T1/T2	T2	T1	T1	
<i>Fat suppression</i>	-	SPAIR	mDixon	mDixon	
<i>Dimensionality</i>	2D	3D	3D	3D	
<i>Acquired resolution</i>	1.04 x 1.04 mm ²	1.25 x 1.32 x 2.41 mm ³	0.99 x 1.05 x 2.19 mm ³	1.20 x 1.22 x 2.41 mm ³	
<i>Reconstructed resolution</i>	-	0.78 x 0.78 x 1.21 mm ³	0.95 x 0.95 x 1.10 mm ³	1.16 x 1.16 x 1.20 mm ³	
<i>Slice thickness</i>	10 mm	-	-	-	
<i>Time per scan</i>	0.6 s	5:48 min	7:51 min	1:00 min	

SPGR = spoiled gradient echo; FSE = fast spin echo; DCE = dynamic contrast-enhanced; SSFP = steady state free precession; mDixon = multi-point Dixon; SPAIR = Spectral Attenuated Inversion Recovery.



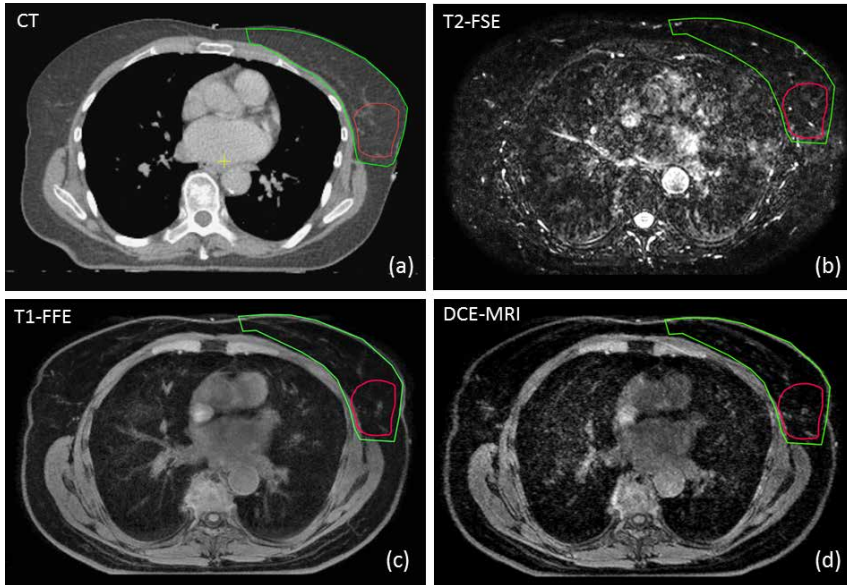
● *Figure 1 Intra-fraction motion visualized on cine-MRI. In (a), a postoperative sagittal slice example, oriented through the tumour bed, is depicted. The clinical target volume (CTV) is depicted in red. Two perpendicular lines (blue and green) are oriented through the tumour bed. Below, the lines acquired for each sagittal slice in the cine-MRI series are stacked from left to right as a function of time, during 120 s. The upper time-stack (a) represents motion in SI direction (blue line), while the bottom time-stack (c) shows AP motion (green line). Stable motion induced by respiration can be observed in both time-stacks. In-plane spatial resolution is $1 \times 1 \text{ mm}^2$. Temporal resolution is 0.6 s.*

● *Table 2* Number of patients with completed scans, on preoperative ('preop.') and postoperative ('postop.') MRI sessions. Completing cine-MRI comprised both sagittal and transverse sequences, while for 3D-MRI this included the acquisition of T1-FFE, T2-FSE, and DCE-MRI scans. 'Both' indicates how many patients completed the scans on both occasions. Some cine-MRI series were omitted for motion analysis; 'Cine-MRI series used' indicates the number of cine-MRI series used, oriented in the transverse ('trans.') and sagittal ('sag.') planes, for the clinical target volume (CTV) and whole breast (WB).

Scans performed	Cine-MRI			3D MRI		
	Preop.	Postop.	Both	Preop.	Postop.	Both
Total completed	18	18	16	21	15	16
Cine-MRI series used (trans./sag.)						
CTV	14 / 16	13 / 18				
WB	14 / 16	14 / 18				

3D MRI for multi-minute motion

Three high-resolution 3-dimensional (3D) scans were applied for motion analysis on a multi-minute time-scale. They were all acquired in the transverse plane (figure 2, table 1). The techniques included a T1 spoiled gradient echo with multi-point Dixon (mDixon) water-fat separation (T1-FFE), which can provide both water-suppressed and fat-suppressed images [17]. Moreover, a T2 fast spin echo technique (T2-FSE) with fat suppression was applied. Finally, a T1-weighted (T1w) dynamic contrast-enhanced technique (DCE-MRI) was performed, employing mDixon water-fat separation. DCE-MRI was included for identification of the tumour preoperatively. First, one scan was acquired in 60 s. Then, immediately after intravenous injection of a contrast agent (Gadobutrol (Gadovist, Bayer), 0.1 mmol/kg, 1 ml/s), another six post-contrast scans were acquired with 60 s intervals each. A single postoperative scan of 60 s was performed similarly, only without acquisition of subsequent contrast-enhanced imaging. The DCE-MRI was the last to be acquired in each MRI session.



● *Figure 2* Transverse slices of a CT scan (a) and three MRI scans (b-d) of one patient, oriented through the tumour (left-sided). Delineations of the CTV_{preop} (red contour) and WB_{preop} (green) are depicted. The 3D MRI sequences shown are (b) T2-FSE; (c) T1-FFE, water-only image of mDixon water-fat suppression method; (d) pre-contrast DCE-MRI, water-only image of mDixon.

The acquisition time of the full MRI scanning protocol was 21 minutes. Hence, the 3D scans performed, i.e. T2-FSE (first), T1-FFE, and DCE-MRI (last), provide information on 3D intra-fraction motion in multi-minute temporal resolution.

CT acquisition

In addition to MRI, all participants underwent computed tomography (CT) scans in RT position for target delineation purposes, both before and after BCS. Preoperatively, this was a contrast-enhanced CT scan, while postoperatively no CT contrast was administered. The CT scans were performed on the same day as the respective MRI measurements. CT acquisition duration was 20 s, slice thickness was 3 mm, and minimal in-plane resolution was $1 \times 1 \text{ mm}^2$ (Brilliance, Philips, Best, The Netherlands).

Delineations

The volumes of interest (VOIs) were delineated, with the use of contouring software Volumetool®, which is developed at the RT Department of UMC Utrecht [18]. Each delineation was performed by one breast radiation oncologist.

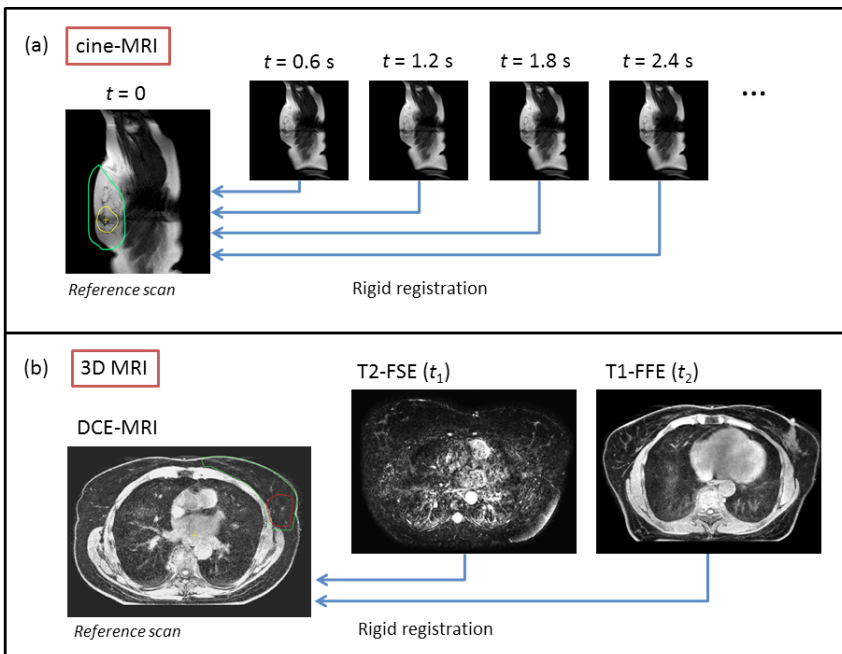
For the preoperative delineations, all available 3D MRI scans were co-registered to the DCE-MRI images, together with the preoperative CT scan. The gross target volume (GTV) was delineated on DCE-MRI. The clinical target volume (CTV_{preop}) was generated by a 15 mm isotropic extension of the GTV, restricted by the chest wall and a 5 mm margin beneath the skin surface. The whole breast (WB_{preop}) was delineated as well, in order to compare motion parameters with those of the CTV_{preop} (figure 2). Significant differences between these parameters could indicate dependence of CTV_{preop} motion with respect to the relative location of the CTV_{preop} and WB_{preop} .

Postoperatively, clinically available delineations were used. These were contoured on CT, which was performed for conventional RT planning. For this study, the CT was co-registered with the postoperative 3D MRI sequences. First, the tumour bed was contoured. Then, the clinical target volume (CTV_{postop}) was generated by a 15 mm extension of the tumour bed in all spatial directions, excluding the chest wall and first 5 mm beneath the skin surface. Again, the whole breast (WB_{postop}) was delineated as well, for a comparison with motion parameters of the CTV_{postop} .

Subsequently, all VOIs were transferred onto a reference scan in the transverse and sagittal planes from the respective cine-MRI series using the MRI coordinate system. No adjustments to the delineations were applied. The fifth slice of each series was taken to be the reference scan in order to ensure a steady state for the bSSFP, such that the contrast was established.

Image registration

To quantify motion, registration between subsequent scans was performed (figure 3).



● Figure 3 Schematic overview of the registrations, depicted by the blue arrows, for (a) cine-MRI (sagittal example) and (b) 3D MRI scans (depicted in transverse plane). Each consecutive cine-MRI scan (acquired every 0.6 s) is registered to the reference cine-MRI scan at $t = 0$. The registration is rigid, and restricted to an area (shown in green in the reference scan) around the whole breast, including a margin of 20 mm outside the outer anatomy to ensure inclusion of the breast contour. The CTV is depicted in yellow. For the 3D MRI scans, the T2-FSE and T1-FFE scans, acquired at t_1 and t_2 , respectively, are rigidly registered to the reference scan, which is the first DCE-MRI scan.

Cine-MRI registration

In the cine-MRI scans, each consecutive scan in a series was registered to the reference slice (figure 3) using a rigid registration algorithm, which only allows rotations and translations, and was based on mutual information (Elastix, Klein *et al.* 2010). Registration was restricted to a two-dimensional (2D) area in the reference frame, encompassing the ipsilateral breast, and an extension of up to 20 mm to ensure inclusion of the breast boundary. Cine-MRI data from two patients was omitted, since the scans were not properly oriented through the tumour area. Furthermore, due to banding artefacts of the bSSFP technique, prominent registration errors were induced in a few scans which were therefore omitted from the analysis (table 2).

The accuracy of registration was validated visually in all cine-MRI scans. The average estimated local error was 1 voxel, with an estimated maximum local error of 2 voxels, in all sagittal and transverse cine-MRI series. A maximum error of 2 voxels amounts to 2 mm in either superior-inferior (SI), anterior-posterior (AP), or left-right (LR) direction.

3D MRI registration

For registration of the 3D scans, the water image of the pre-contrast DCE-MRI scan was taken as reference scan (figure 3). Manual rigid registration of T1-FFE and T2-FSE scans to the reference scan was performed using in-house developed software Volumetool® [18]. Automatic cross-contrast registration algorithms are complex and prone to errors, thereby hampering automatic registration using mutual information, similar to what was used in the cine-MRI data. Particularly, in the T2-FSE sequence, the outer breast boundary was not visible. Therefore, manual registration was chosen for the 3D scans, by employing anatomical landmarks within the ipsilateral breast. In 5 of the 20 patients who were scanned post-BCS, no DCE-MRI was performed (table 2). Therefore, in the post operative analysis, the 3D scans from the remaining 15 patients are considered. The accuracy of registration was validated visually in all 3D MRI scans. The maximum estimated local registration errors from the 3D scans to the reference scan was 2-3 mm in either spatial direction.

Quantifying motion

Intra-fraction motion of all CTV and WB delineations was derived, on scans in both temporal scales.

Sub-second motion calculation

After registration of the cine-MRI scans, the displacements of all image voxels, between two scans were calculated using Elastix. The transformation for this was derived, and the points of the delineated volume were transformed accordingly. From this, absolute distances were then derived for each point in each delineation and in all in-plane directions using MATLAB (*Math Works*, USA) software. From the sagittal cine-MRI series, SI and AP motion was calculated, while the transverse cine-MRI scans yielded information on AP and LR motion (table 2). Thus, the cine-MRI provided motion information on sub-second temporal resolution,

during two minutes.

Multi-minute motion calculation

The displacements of all voxels in each VOI between the consecutive 3D scans were calculated from the manual registration using the Volumetool® software. The VOIs were subsequently transformed. Similar to the sub-second motion calculation, absolute distances were calculated from these transformations in the multi-minute analysis, using MATLAB software. The 3D MRI scans provided motion data in all three spatial directions, on a multi-minute time-scale.

P95 distance parameter

As a measure of intra-fraction motion, the P95 distance was acquired in both cine-MRI and 3D MRI, for each delineation in each direction. P95 is defined as the distance which ensures coverage of 95% of the voxel displacements in the delineation, in a specific direction. This cut-off was chosen such that any large deviations induced by possible registration errors are omitted, which could induce overestimation of motion. The P95 parameter was derived for CTV_{preop} , CTV_{postop} , WB_{preop} , and WB_{postop} , in all orientations, for each time step, in both temporal regimes. As an indication of the maximum amplitude during the full 120 s duration of a cine-MRI series, the maximum P95 ($P95_{max}$) in each direction was determined. Since three 3D MRI scans were acquired each MRI session, two P95 values were found to indicate multi-minute displacements.

Statistics

For patients who underwent both pre-BCS and post-BCS MRI, motion parameters were compared by a paired student's *t*-test. Moreover, motion parameters between all patients (including those who are scanned once) are compared using the unpaired student's *t*-test. A statistically significant difference is indicated by $p < 0.05$.

Results

Sub-second intra-fraction motion during two minutes

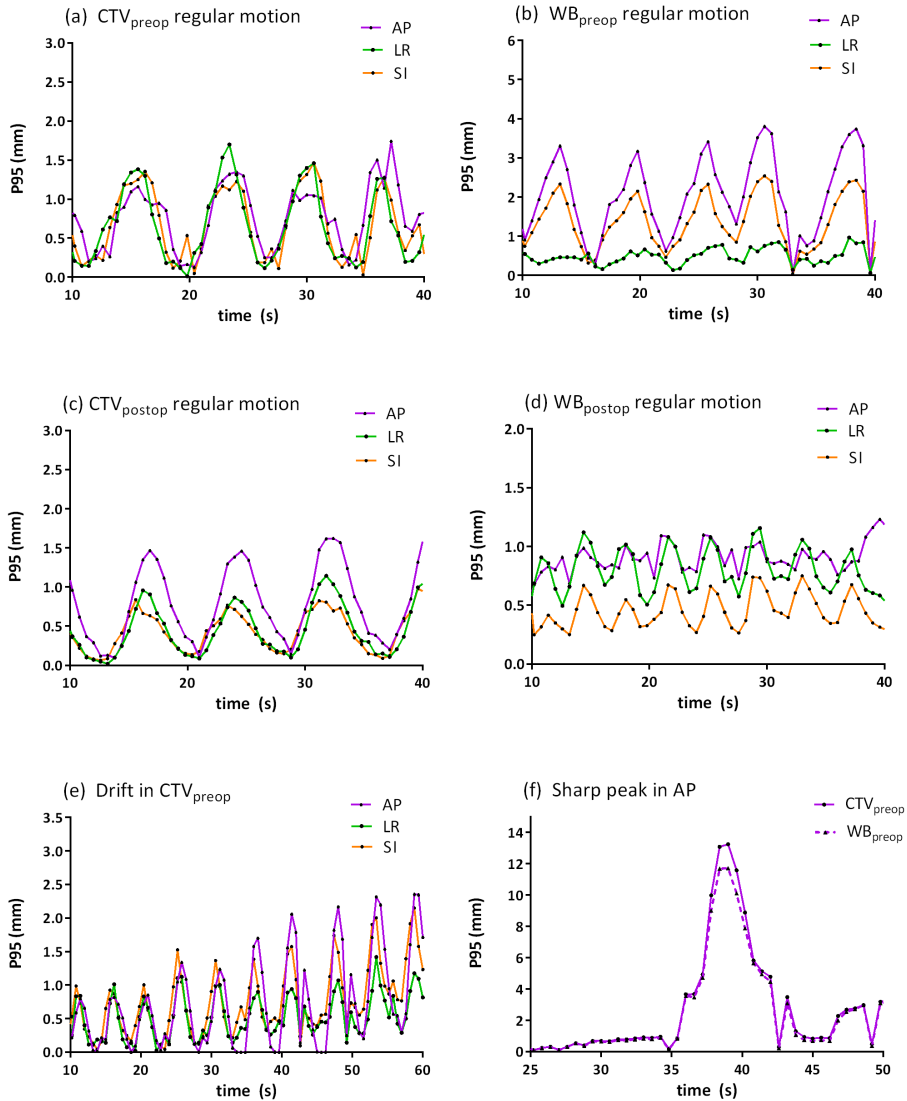
The P95 motion behaviour is regular through time during two minutes, i.e. stable and repeating motion is visible in all spatial directions in almost all patients (figure 4). This wave-like pattern indicates stable breathing, which is reflected by the P95 generally showing the highest values in AP direction. Stable and limited motion amplitudes were predominantly observed in both the preoperative and postoperative settings, for almost all cine-MRI series (figure 4). When regular breathing was observed, peak-to-peak cycle durations were found to be in the range of 5 – 12 s, both before and after BCS. For individual patients showing regular respiration during two minutes, P95 motion amplitudes and cycle durations were very similar when comparing preoperative and postoperative situations.

Irregularities were observed as well, which induced deviations of the P95 parameter. Three distinct types of atypical behaviour are noted: an upward drift in motion amplitude; a temporary peak in P95; a sudden amplitude drop. An upward drift was only observed in five patients, for whom the associated P95 increase was limited to a maximum of 2.4 mm (in CTV and WB) over 120 s (figure 4(e)).

In three cine-MRI series a temporary peak was observed, indicating a significant increase in P95 during several seconds. The largest deviation caused by this amounted to a $P95_{\max}$ of 11.7 mm/13.2 mm in AP direction for $CTV_{\text{preop}}/WB_{\text{preop}}$ in one patient (figure 4(f)). This exceptional value was induced by a single deep respiration. Other peaks were visible in two other patients, yielding one large $P95_{\max}$ of 7.0 mm/8.2 mm for $CTV_{\text{preop}}/WB_{\text{preop}}$ in AP, and a smaller one of 2.3 mm/2.4 mm in the same orientation.

Finally, a sudden amplitude drop was observed in three series. The maximum P95 value for these patients, just before the sudden decline in amplitude, was on average 2.0 mm for WB_{postop} . Therefore, the decrease in P95 implied an even smaller motion amplitude.

In general, intra-fraction motion over the course of 2 min is limited: the median $P95_{\max}$ in AP, LR, and SI direction is 1.2 mm, 0.6 mm, and 0.8 mm



● Figure 4 Examples of parameter P95 as a measure of motion, in six different patients. P95 is plotted as a function of time, in sub-second temporal resolution (0.6 s). Note that the ranges of the vertical axes differ. Typical regular motion can be observed in (a)-(d), where P95 (indicated by black dots) is shown during 30 s for the CTV_{preop}, WB_{preop}, CTV_{postop}, and WB_{postop}, respectively. This is shown for the AP (purple), LR (green), and SI (orange) directions. An insignificant drift in intra-fraction motion of a CTV_{preop} during 50 s is depicted in (e), while (f) shows a peak in P95 value in the AP direction for a patient in both CTV_{preop} (black dots, full purple line) and WB_{preop} (black triangles, dashed purple line) due to deep in- and exhalation. Different breathing phases and amplitudes were observed throughout all patients.

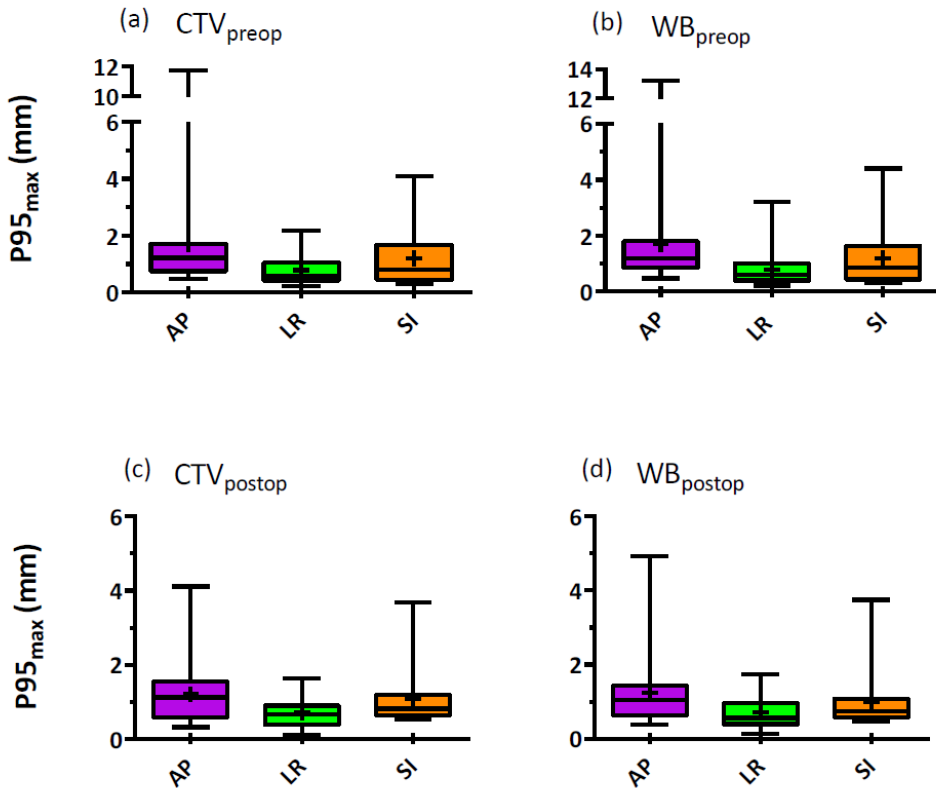
for CTV_{preop} , while for WB_{preop} this is very similar (table 3, figure 5). Motion calculated from the postoperative cine-MRI scans is restricted to a median $P95_{max}$ for CTV_{postop} in AP, LR, and SI direction of 1.2 mm, 0.7 mm, and 0.8 mm, respectively, while the values for WB_{postop} are almost identical. Relative to preoperative values of $P95_{max}$, no differences were found for the postoperative values for both whole breast and CTV, in all spatial directions ($p > 0.05$ for all).

Temporal resolution of multi-minute motion

The temporal resolution of the multi-minute motion was determined by the start and duration of acquisition of each 3D scan. The median interval between the DCE-MRI scan and the start of acquisition of the T2-FSE scan was 13 min (range: 9 – 26 min), in the preoperative setting, which is taken as the first time-point (t_1) for the multi-minute analysis. The second time-point (t_2) was chosen as the median interval between the reference scan and start of acquisition of the T1-FFE, which was 20 min (range: 16 – 35 min). The two postoperative time-points were determined similarly: t_1 was taken at 13 min, whereas t_2 was 19 min. Analogously to the preoperative values, postoperative t_1 and t_2 are determined by the median intervals relative to the reference scan (ranges: 7 – 16 min and 14 – 22 min, respectively).

Multi-minute intra-fraction motion

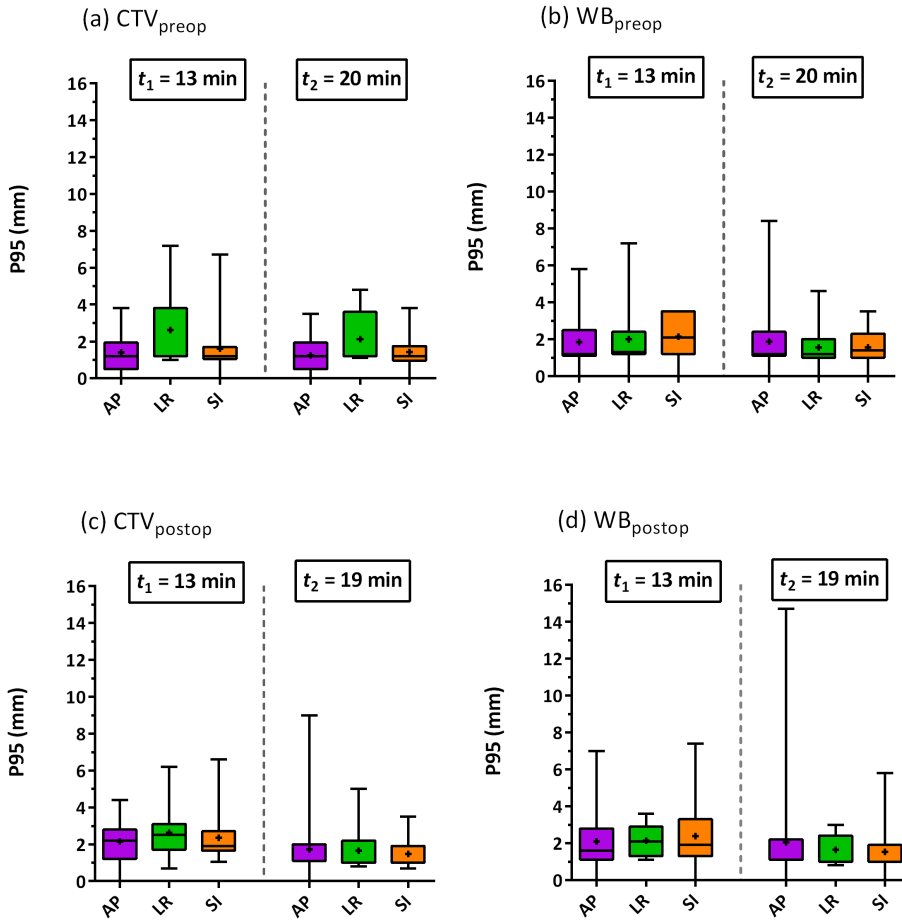
Multi-minute displacements are limited to about the voxel sizes in the preoperative 3D MRI scans for CTV_{preop} : the median $P95$ in AP, LR, and SI direction is 1.2, 1.2, and 1.2 mm for CTV_{preop} at t_1 . For WB_{preop} this is 1.2 mm, 1.3 mm and 2.1 mm. At t_2 , median motion in the AP, LR, SI directions is found to be similar for CTV_{preop} and WB_{preop} (table 3, figure 6). Between the two time-points ($t_2 - t_1 = 7$ min), there are no significant differences in AP and LR for both CTV_{preop} and WB_{preop} ($p > 0.05$ for all, both paired and unpaired). In SI, a paired t -test shows no difference ($p = 0.02$) for WB_{preop} between t_2 and t_1 , whereas the unpaired t -test shows a slight difference in WB_{preop} ($p < 0.05$) in that orientation. However, the respective medians at both time-points are small. Large maximum deviations in $P95$ over the course of several minutes were infrequently observed as well, up to 7.2 mm/8.4 mm in SI direction for CTV_{preop}/WB_{preop} .



● *Figure 5* The maximum P95 ($P95_{max}$) parameter as a measure of maximum motion, derived from the cine-MRI scans, acquired during 120 s, of all patients, shown for (a) CTV_{preop} , (b) WB_{preop} , (c) CTV_{postop} , and (d) WB_{postop} . The spatial directions are labelled: AP (purple boxes), LR (green), and SI (orange). The height of the boxes represents the 25-75 percentile range, with whiskers marking the minimum/maximum values. The line inside each box represents the median value, whereas the mean value is denoted by the '+' symbol. Note that the vertical axes in (a) and (b) are broken.

Motion derived from the postoperative scans was also limited: the median P95 displacements for CTV_{postop} in AP, LR, and SI directions was about 2 mm at t_1 , with similar values for WB_{postop} (table 3). At t_2 , the median P95 parameters were 1.2 mm in all spatial directions for both CTV_{postop} and WB_{postop} . This indicates significant differences between the two time-points ($t_2 - t_1 = 6$ min); however, the respective values are small. Over the course of minutes in the postoperative setting, large maximum displacements were also found, although infrequently. The maximum deviation found amounted to a P95 value of 9.0 mm/14.5 mm for CTV_{postop} / WB_{postop} in AP direction for one patient at t_2 .

Finally, P95 for CTV_{postop} and WB_{postop} , at both time-points were compared relative to the preoperative values. Only one parameter was found to be significant: P95 of CTV_{preop} in AP direction, compared to P95 of CTV_{postop} at t_1 ($p = 0.01$, paired; $p = 0.09$, unpaired). However, the respective medians were again very small. No other statistically significant differences were found pre- vs. postoperatively ($p > 0.05$ for all).



● *Figure 6 The P95 parameter as a measure of motion, derived from the 3D MRI scans, at $t_1 = 13$ min and $t_2 = 20$ min (preoperatively) or $t_2 = 19$ min (postoperatively), for all patients, shown for (a) CTV_{preop} , (b) WB_{preop} , (c) CTV_{postop} , and (d) WB_{postop} . The spatial directions are labelled: AP (purple boxes), LR (green), and SI (orange). The height of the boxes represents the 25-75 percentile range, while the whiskers mark the minimum/maximum values. The line inside each box represents the median value, whereas the mean value is denoted by the '+' symbol.*

● *Table 3 P95 motion values as an indication of motion. They are derived for the WB and CTV, from both preoperative and postoperative MRI scans. Values are indicated as ‘median (range)’, and are given for anterior-posterior (AP), left-right (LR), and superior-inferior (SI) orientations. For the cine-MRI scans, the P95_{max} are given, indicating the maximum P95 motion values during the 2-min cine-MRI series. For 3D MRI, P95 is given at two time-points. Preoperatively, t₁ = 13 min and t₂ = 20 min, while postoperatively, t₁ = 13 min and t₂ = 19 min, with respect to the reference scan.*

	Cine-MRI		3D MRI			
	P95 _{max} WB _{preop}	WB _{postop}	P95 WB _{preop} t ₁	t ₂	WB _{postop} t ₁	t ₂
AP	1.2 (0.5 – 13.2)	1.0 (0.4 – 4.9)	1.2 (0 – 3.8)	1.2 (0 – 8.4)	1.6 (0 – 7.0)	1.1 (0 – 14.7)
LR	0.6 (0.2 – 3.2)	0.6 (0.1 – 1.7)	1.3 (0 – 7.2)	1.2 (0 – 4.6)	2.1 (1.1 – 3.6)	1.0 (0.8 – 3.0)
SI	0.9 (0.3 – 4.4)	0.7 (0.5 – 3.7)	2.1 (0 – 3.5)	1.4 (0 – 3.5)	1.9 (0 – 7.4)	1.0 (0 – 5.8)
	CTV _{preop}	CTV _{postop}	CTV _{preop} t ₁	t ₂	CTV _{postop} t ₁	t ₂
AP	1.2 (0.5 – 11.7)	1.1 (0.3 – 4.1)	1.2 (0 – 3.8)	1.2 (0 – 3.5)	2.2 (0 – 4.4)	1.1 (0 – 9.0)
LR	0.6 (0.2 – 2.2)	0.7 (0.7 – 1.6)	1.2 (1.0 – 7.2)	1.2 (1.1 – 4.8)	2.5 (0.7 – 6.2)	1.0 (0.8 – 5.0)
SI	0.8 (0.3 – 4.1)	0.8 (0.5 – 3.7)	1.2 (0 – 6.7)	1.2 (0 – 3.8)	1.9 (1.1 – 1.9)	1.0 (0.7 – 3.5)

Discussion

To our knowledge, this is the first study to characterize local intra-fraction target motion in breast RT, using supine MRI. We were able to quantify motion in high temporal (on cine-MRI) and low temporal resolution (on 3D MRI), both before and after BCS. In high temporal resolution, motion over 120 s was regular, and median motion amplitudes were restricted to 2 mm. These patterns reflected normal respiration. Amplitudes were generally small, and large amplitudes (up to 14 mm), due to sudden in- and exhalation, were only temporary. Therefore, the impact of respiratory motion on RT treatments will likely be small. Conversely, the multi-minute analysis, in lower temporal resolution, showed actual whole-body shifts between or during acquisition of 3D MRI scans. Although the median displacements were limited, the values varied more, and ranged up to 14 mm over the course of up to 21 minutes. Large shifts will affect the treatment accuracy, especially in case of long treatment times and small targets. Therefore, this is especially relevant for novel hypofractionated APBI techniques, such as a single fraction of 15 Gy, 18 Gy, or 21 Gy [7,20].

Limited intra-fraction motion values have been reported previously, on both short and long time scales, with average movement never exceeding 5 mm (Michalski *et al.* 2012). Similar to our study, large variations (in the order of cm), over the course of a treatment session, were observed infrequently. These studies were performed using imaging techniques which are unable to directly image the target, in 3D, in high temporal resolution, and over extended periods, during RT delivery. Thus, a suitable technique should have the capability of visualizing the tumour (bed), and the ability to image during actual dose delivery. In these aspects, current image-guidance methods are limited. Firstly, EPID samples projections, which are generated perpendicularly to the radiation beam [22]. The tumour (bed) cannot be visualized directly in 3D, such that relative motion of anatomical structures, e.g. the thoracic wall and lungs, are usually considered instead. EPID sampling rates are in the order of 2 images/s. Although imaging durations in the previous studies were limited to <15 s, EPID can be performed for extended times, and during RT delivery. However, EPID sampling usually requires tangential RT delivery with opposing beams to visualize the thoracic wall and therefore the technique will be less suitable for increasingly complex beam orientations. Furthermore, CBCT can image the tumour bed directly in 3D [23], although often in combination with fiducial markers due to insufficient tumour visualization. However, the temporal resolution of CBCT is limited, since it is only performed before and after RT delivery. Finally, 3D surface imaging is capable of tracking the patient position, in near real-time over long periods [21]. However, the method is limited to monitoring the outer breast boundary. MRI, on the other hand, enables direct characterization of local target motion due to inherently high soft-tissue contrast and has the ability to produce images both in high and low temporal regimes, and over long periods of time, without the necessity of using markers. MRI during actual RT delivery could be enabled by an MRI/RT hybrid modality, such as the UMC Utrecht MRL [14,15].

Fast MR imaging was achieved in the cine-MRI series by use of a bSSFP sequence. Cine-MRI has previously been used to determine motion of other soft-tissue targets [24–28]. An advantage of bSSFP is the relatively high signal-to-noise ratio, compared to T1-weighted (T1w) or T2w SSFP scans, while being acquired at high speed [13]. However, in 13 (18%) out of the 72 cine-MRI scans in our study, prominent banding artefacts were

present near the skin surface and/or lung, which could partly or completely obscure the tumour (bed) and/or breast boundary. A bSSFP sequence is sensitive to magnetic-field inhomogeneities [13,29], resulting in these artefacts when the accumulated phase is exactly π . This is prominent where susceptibility differences are large, e.g. near air-tissue boundaries. A better shimming method could reduce the artefacts [30]. In order to minimize the impact of these artefacts, all registrations in this study were rigid, thereby only allowing translations and rotations. This was supported by the fact that observed motion amplitudes were generally small. However, due to the imaging artefacts, registration remained unsuccessful in the 13 cine-MRI series, which were omitted from our analysis.

Analysis of intra-fraction motion was performed on both the whole breast and CTV, since large motion differences between these could indicate that local tumour (bed) movement is dependent on the location with respect to the whole breast. However, this was not observed in our study. Furthermore, the results of the whole breast analysis may be relevant for highly hypofractionated WBI techniques [31].

The goal of the current work was to observe and analyze variations through time, given a certain delineation. Each delineation was performed by one breast radiation oncologist. Hence, intra-observer contouring variability was not taken into account in this study. However, we have shown that intra-fraction motion of CTV and WB contours is very similar. Analogously, we expect that a small variation in contouring of the tumour (bed) will not affect the results presented here.

Some blurring could be observed in the 3D MRI scans, possibly induced due to breathing during acquisition of the images. However, the position of the registration landmarks, albeit possibly blurred, was on average the same. Therefore, it was possible to derive motion in the multi-minute scale.

The maximum local estimated registration error in the cine-MRI scans was small (2 mm) and was observed in a limited number of scans – up to 2 out of 200 per series per patient. Since each scan is registered to the reference scan, this is not a propagating error. No extra uncertainty due to observer bias is expected here, since cine-MRI registration was performed automatically and observed errors were generally very small.

Furthermore, sub-second P95 motion could clearly be observed, which implies that blurring of the motion by registration errors is only minimal. The maximum local manual registration error of the 3D MRI is larger, at 2-3 mm, which is in the order of the median displacement values. However, the maximum P95 values observed over minutes are significantly larger. Both registration error and validation uncertainties could be reduced if more observers are employed. Potentially, for both cine-MRI and 3D MRI data, it is possible that some P95 values are influenced by registration errors. However, the most relevant errors are the maximum P95 values. Relative to these, the registration errors are small.

Displacements between individual fractions could be taken into account by employing an adequate position verification strategy. However, the potential problem of intra-fraction motion, i.e. movement during RT delivery, remains. In order to account for this, extra margins could be applied to the target volumes. This will, however, lead to increased radiation dose to healthy tissue, possibly resulting in higher toxicity and impaired cosmetic results. Although the impact of breathing on RT treatments is limited, respiratory motion may be restricted by breath-holding techniques during dose delivery [32,33]. Whole-body shifts are more likely to affect treatments since they are not temporary. Permanent displacements will be of significant consequence as they result in geometric target miss, leading to target underdosage and higher dose to healthy tissue [34]. This has been shown in other tumour sites as well [35–37]. Accounting for these shifts is therefore necessary. Whole-body displacements could be reduced by immobilizing the patient. The use of customized vacuum bags or other immobilization devices has been investigated, albeit with largely varying results [38–40]. In order to directly observe whole-body displacements, the target position could also be tracked during irradiation. External markers are commonly used to establish a relation between external and internal motion.

The best approach, however, is imaging the internal motion itself. Current methods are fiducial-based techniques [41,42], which are inherently invasive and are unable to handle anatomical deformations. Due to the many possibilities of MRI, on-line MRI guidance is a potentially powerful non-invasive approach which can be explored. As mentioned previously, MRI guidance is facilitated by the MRL, and it is also investigated in

other hybrid MRI/RT modalities [43,44]. We have previously shown the dosimetric feasibility of performing APBI in the MRL [45]. Since the MRL is primarily designed for dynamic (re-)planning and tracking, fast on-line plan adaptation is possible. Dedicated MRI/RT techniques are required for detection of anatomical variations during RT delivery.

In this study, MRI was performed in a diagnostic MRI scanner. Thus, any aspects, both physical and psychological, which could influence patient motion during actual irradiation, were not taken into account. Using a hybrid MRI/RT modality, an analysis of intra-fraction motion during dose delivery is required.

Our study indicated no differences between motion from before and after BCS, supporting recent studies which are exploring preoperative approaches [5,7,8]. The fusion of MRI and RT may allow for the development of novel high-precision hypofractionated APBI strategies. Currently, we are further exploiting the potential advantages of preoperative MRI-guided breast RT. A study is ongoing at UMC Utrecht to investigate the clinical feasibility of delivering a single high dose preoperatively to the tumour, in early-stage breast-cancer patients. In the future, it may be feasible to move towards highly precise stereotactic breast-cancer treatments in the MRL.

Conclusions

Intra-fraction motion in breast RT was quantified with MRI sequences in supine RT position, at high and low temporal resolution. Breathing motion could be observed, as well as whole-body shifts at long time scales (up to 14 mm). Although the impact of intra-fraction movement on standard breast RT techniques is likely small, this information is essential for safe delivery in future (pre- and postoperative) hypofractionated APBI strategies due to long treatment times and small targets. In order to avoid target miss, adaptive strategies could be enabled by on-line guidance on an MRL.

Acknowledgements

The authors hereby thank Jean-Paul Kleijnen and Didi de Gouw for their input.

References

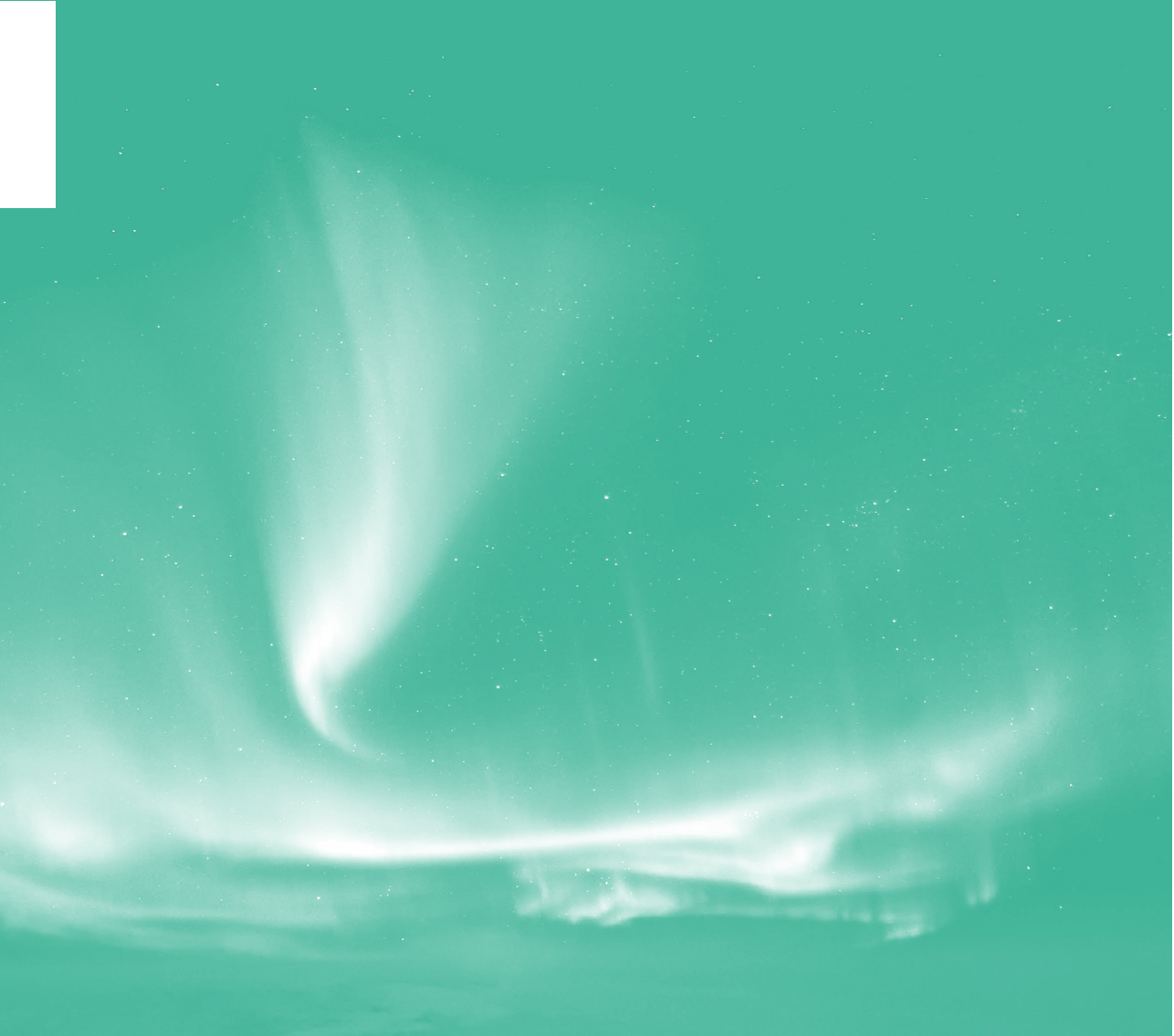
- [1] Ciammella P, Podgornii A, Galeandro M, Micera R, Ramundo D, Palmieri T, et al. Toxicity and cosmetic outcome of hypofractionated whole-breast radiotherapy: predictive clinical and dosimetric factors. *Radiat Oncol* 2014;9:97. doi:10.1186/1748-717X-9-97.
- [2] Min C, Connolly E, Chen T, Jozsef G, Formenti SC. Hypofractionated radiation therapy for early stage breast cancer: outcomes, toxicities, and cost analysis. *Breast J* 2014;20:267–73. doi:10.1111/tbj.12254.
- [3] Moser EC, Vrieling C. Accelerated partial breast irradiation: the need for well-defined patient selection criteria, improved volume definitions, close follow-up and discussion of salvage treatment. *Breast* 2012;21:707–15. doi:10.1016/j.breast.2012.09.014.
- [4] Shaitelman SF, Khan AJ, Woodward WA, Arthur DW, Cuttino LW, Bloom ES, et al. Shortened Radiation Therapy Schedules for Early-Stage Breast Cancer: A Review of Hypofractionated Whole-Breast Irradiation and Accelerated Partial Breast Irradiation. *Breast J* 2014;20:131–46. doi:10.1111/tbj.12232.
- [5] van der Leij F, Bosma SCJ, van de Vijver MJ, Wesseling J, Vreeswijk S, Rivera S, et al. First results of the preoperative accelerated partial breast irradiation (PAPBI) trial. *Radiother Oncol* 2015. doi:10.1016/j.radonc.2015.02.002.
- [6] Polgár C, Fodor J, Major T, Sulyok Z, Kásler M. Breast-conserving therapy with partial or whole breast irradiation: ten-year results of the Budapest randomized trial. *Radiother Oncol* 2013;108:197–202. doi:10.1016/j.radonc.2013.05.008.
- [7] Horton JK, Blitzblau RC, Yoo S, Geradts J, Chang Z, Baker JA, et al. Preoperative Single-Fraction Partial Breast Radiation Therapy: A Novel Phase 1, Dose-Escalation Protocol With Radiation Response Biomarkers. *Int J Radiat Oncol* 2015;92:846–55. doi:10.1016/j.ijrobp.2015.03.007.
- [8] Blitzblau RC, Arya R, Yoo S, Baker JA, Chang Z, Palta M, et al. A phase 1 trial of preoperative partial breast radiation therapy: Patient selection, target delineation, and dose delivery. *Pract Radiat Oncol* 2015. doi:10.1016/j.ppro.2015.02.002.
- [9] Langen KM, Jones DT. Organ motion and its management. *Int J Radiat Oncol Biol Phys* 2001;50:265–78.
- [10] Michalski A, Atyeo J, Cox J, Rinks M. Inter- and intra-fraction motion during radiation therapy to the whole breast in the supine position: a systematic review. *J Med Imaging Radiat Oncol* 2012;56:499–509. doi:10.1111/j.1754-9485.2012.02434.x.
- [11] Schmitz AC, Pengel KE, Loo CE, van den Bosch M a a J, Wesseling J, Gertenbach M, et al. Pre-treatment imaging and pathology characteristics of invasive breast cancers of limited extent: potential relevance for MRI-guided localized therapy. *Radiother Oncol* 2012;104:11–8. doi:10.1016/j.radonc.2012.04.014.
- [12] Oseledchyk A, Kaiser C, Nemes L, Döbler M, Abramian A, Keyver-Paik M-D, et al. Preoperative MRI in patients with locoregional recurrent breast cancer: influence on treatment modalities. *Acad Radiol* 2014;21:1276–85. doi:10.1016/j.acra.2014.05.012.
- [13] Bieri O, Scheffler K. Fundamentals of balanced steady state free precession MRI. *J Magn Reson Imaging* 2013;38:2–11. doi:10.1002/jmri.24163.
- [14] Legendijk JJW, Raaymakers BW, Raaijmakers AJE, Overweg J, Brown KJ, Kerkhof EM, et al. MRI/linac integration. *Radiother Oncol* 2008;86:25–9. doi:10.1016/j.radonc.2007.10.034.
- [15] Raaymakers BW, Legendijk JJW, Overweg J, Kok JGM, Raaijmakers AJE, Kerkhof EM, et al. Integrating a 1.5 T MRI scanner with a 6 MV accelerator: proof of concept. *Phys Med Biol* 2009;54:N229–37. doi:10.1088/0031-9155/54/12/N01.

- [16] den Hartogh MD, Philippens ME, van Dam IE, Kleynen CE, Tersteeg RJ, Pijnappel RM, et al. MRI and CT imaging for preoperative target volume delineation in breast-conserving therapy. *Radiat Oncol* 2014;9:63. doi:10.1186/1748-717X-9-63.
- [17] Eggers H, Brendel B, Duijndam A, Herigault G. Dual-echo Dixon imaging with flexible choice of echo times. *Magn Reson Med* 2011;65:96–107. doi:10.1002/mrm.22578.
- [18] Bol GH, Kotte ANTJ, van der Heide UA, Lagendijk JJW. Simultaneous multi-modality ROI delineation in clinical practice. *Comput Methods Programs Biomed* 2009;96:133–40. doi:10.1016/j.cmpb.2009.04.008.
- [19] Klein S, Staring M, Murphy K, Viergever M a, Pluim JPW. Elastix: a Toolbox for Intensity-Based Medical Image Registration. *IEEE Trans Med Imaging* 2010;29:196–205. doi:10.1109/TMI.2009.2035616.
- [20] Palta M, Yoo S, Adamson JD, Prosnitz LR, Horton JK. Preoperative single fraction partial breast radiotherapy for early-stage breast cancer. *Int J Radiat Oncol Biol Phys* 2012;82:37–42. doi:10.1016/j.ijrobp.2010.09.041.
- [21] Wiant DB, Wentworth S, Maurer JM, Vanderstraeten CL, Terrell JA, Sintay BJ. Surface imaging-based analysis of intrafraction motion for breast radiotherapy patients. *J Appl Clin Med Phys* 2014;15:4957.
- [22] Fein DA, McGee KP, Schultheiss TE, Fowble BL, Hanks GE. Intra- and interfractional reproducibility of tangential breast fields: a prospective on-line portal imaging study. *Int J Radiat Oncol Biol Phys* 1996;34:733–40.
- [23] Jaffray DA, Siewerdsen JH, Wong JW, Martinez AA. Flat-panel cone-beam computed tomography for image-guided radiation therapy. *Int J Radiat Oncol Biol Phys* 2002;53:1337–49.
- [24] Heerkens HD, van Vulpen M, van den Berg CAT, Tijssen RHN, Crijs SPM, Molenaar IQ, et al. MRI-based tumor motion characterization and gating schemes for radiation therapy of pancreatic cancer. *Radiother Oncol* 2014;111:252–7. doi:10.1016/j.radonc.2014.03.002.
- [25] Akino Y, Oh R-J, Masai N, Shiomi H, Inoue T. Evaluation of potential internal target volume of liver tumors using cine-MRI. *Med Phys* 2014;41:111704. doi:10.1118/1.4896821.
- [26] Sawant A, Keall P, Pauly KB, Alley M, Vasanawala S, Loo BW, et al. Investigating the feasibility of rapid MRI for image-guided motion management in lung cancer radiotherapy. *Biomed Res Int* 2014;2014:485067. doi:10.1155/2014/485067.
- [27] Bjerre T, Crijs S, af Rosenschöld PM, Aznar M, Specht L, Larsen R, et al. Three-dimensional MRI-linac intra-fraction guidance using multiple orthogonal cine-MRI planes. *Phys Med Biol* 2013;58:4943–50. doi:10.1088/0031-9155/58/14/4943.
- [28] Stam MK, van Vulpen M, Barendrecht MM, Zonnenberg BA, Intven M, Crijs SPM, et al. Kidney motion during free breathing and breath hold for MR-guided radiotherapy. *Phys Med Biol* 2013;58:2235–45. doi:10.1088/0031-9155/58/7/2235.
- [29] Tsao J, Kozerke S, Boesiger P, Pruessmann KP. Optimizing spatiotemporal sampling for k-t BLAST and k-t SENSE: application to high-resolution real-time cardiac steady-state free precession. *Magn Reson Med* 2005;53:1372–82. doi:10.1002/mrm.20483.
- [30] Lee J, Lustig M, Kim D, Pauly JM. Improved shim method based on the minimization of the maximum off-resonance frequency for balanced steady-state free precession (bSSFP). *Magn Reson Med* 2009;61:1500–6. doi:10.1002/mrm.21800.
- [31] Tsang Y, Haviland J, Venables K, Yarnold J. The impact of dose heterogeneity on late normal tissue complication risk after hypofractionated whole breast radiotherapy. *Radiother Oncol* 2012;104:143–7. doi:10.1016/j.radonc.2012.06.002.

- [32] George R, Keall PJ, Kini VR, Vedam SS, Siebers J V, Wu Q, et al. Quantifying the effect of intrafraction motion during breast IMRT planning and dose delivery. *Med Phys* 2003;30:552. doi:10.1118/1.1543151.
- [33] Chopra S, Dinshaw KA, Kamble R, Sarin R. Breast movement during normal and deep breathing, respiratory training and set up errors: implications for external beam partial breast irradiation. *Br J Radiol* 2006;79:766–73. doi:10.1259/bjr/98024704.
- [34] Fatunase T, Wang Z, Yoo S, Hubbs JL, Prosnitz RG, Yin F-F, et al. Assessment of the residual error in soft tissue setup in patients undergoing partial breast irradiation: results of a prospective study using cone-beam computed tomography. *Int J Radiat Oncol Biol Phys* 2008;70:1025–34. doi:10.1016/j.ijrobp.2007.07.2344.
- [35] Navarro-Martin A, Cacicedo J, Leaman O, Sancho I, García E, Navarro V, et al. Comparative analysis of thermoplastic masks versus vacuum cushions in stereotactic body radiotherapy. *Radiat Oncol* 2015;10:176. doi:10.1186/s13014-015-0484-7.
- [36] Josipovic M, Persson GF, Logadottir A, Smulders B, Westmann G, Bangsgaard JP. Translational and rotational intra- and inter-fractional errors in patient and target position during a short course of frameless stereotactic body radiotherapy. *Acta Oncol* 2012;51:610–7. doi:10.3109/0284186X.2011.626448.
- [37] Schippers MGA, Bol GH, de Leeuw AAC, van der Heide UA, Raaymakers BW, Verkooijen HM, et al. Position shifts and volume changes of pelvic and para-aortic nodes during IMRT for patients with cervical cancer. *Radiother Oncol* 2014;111:442–5. doi:10.1016/j.radonc.2014.05.013.
- [38] Nalder CA, Bidmead AM, Mubata CD, Tait D, Beardmore C. Influence of a vac-fix immobilization device on the accuracy of patient positioning during routine breast radiotherapy. *Br J Radiol* 2001;74:249–54. doi:10.1259/bjr.74.879.740249.
- [39] Thilmann C, Adamietz IA, Saran F, Mose S, Kostka A, Böttcher H. The Use of a Standardized Positioning Support Cushion During Daily Routine of Breast Irradiation. *Int J Radiat Oncol* 1998;41:459–63. doi:10.1016/S0360-3016(98)00022-4.
- [40] Mitine C, Dutreix A, van der Schueren E. Tangential breast irradiation: influence of technique of set-up on transfer errors and reproducibility. *Radiother Oncol* 1991;22:308–10.
- [41] Ma Y, Lee L, Keshet O, Keall P, Xing L. Four-dimensional inverse treatment planning with inclusion of implanted fiducials in IMRT segmented fields. *Med Phys* 2009;36:2215. doi:10.1118/1.3121425.
- [42] Willoughby TR, Kupelian PA, Pouliot J, Shinohara K, Aubin M, Roach M, et al. Target localization and real-time tracking using the Calypso 4D localization system in patients with localized prostate cancer. *Int J Radiat Oncol Biol Phys* 2006;65:528–34. doi:10.1016/j.ijrobp.2006.01.050.
- [43] Dempsey J, Dionne B, Fitzsimmons J, Haghigat A, Li J, Low D, et al. WE-E-ValA-06: A Real-Time MRI Guided External Beam Radiotherapy Delivery System. *Med Phys* 2006;33:2254. doi:10.1118/1.2241803.
- [44] Fallone BG, Murray B, Rathee S, Stanescu T, Steciw S, Vidakovic S, et al. First MR images obtained during megavoltage photon irradiation from a prototype integrated linac-MR system. *Med Phys* 2009;36:2084–8.
- [45] van Heijst TCF, den Hartogh MD, Lagendijk JJW, van den Bongard HJGD, van Asselen B. MR-guided breast radiotherapy: feasibility and magnetic-field impact on skin dose. *Phys Med Biol* 2013;58:5917–30. doi:10.1088/0031-9155/58/17/5917.

“Je gaat het pas zien als je het doorhebt.”

Johan Cruijff



MRI sequences for detection of individual lymph nodes in regional breast radiotherapy planning

Tristan C. F. van Heijst
Bram van Asselen
Ruud M. Pijnappel
Marissa Cloos-van Balen
Jan J. W. Lagendijk
H. J. G. Desirée van den Bongard
Marielle E. P. Philippens

British Journal of Radiology 89 (2016): 20160072

Abstract

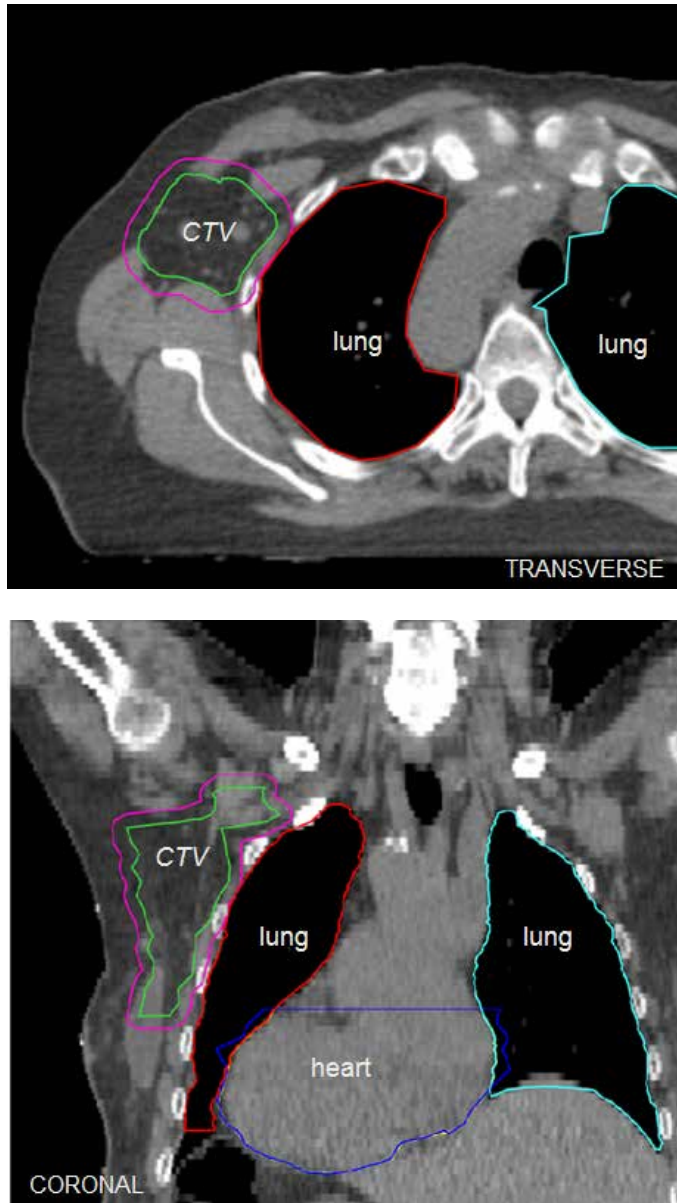
In regional radiotherapy (RT) for breast-cancer patients, lymph node (LN) targets are delineated on CT, defined by anatomical boundaries. By identifying individual LNs, MRI-based delineations may reduce target volumes and thereby toxicity. We optimized MRI sequences for this purpose. Aim was to evaluate the techniques for LN delineation in RT planning. Supine MRI was explored at 1.5 T in RT position (arms in abduction). Five MRI techniques were optimized in 10 and evaluated in 12 healthy female volunteers. The scans included one T1-weighted (T1w), three T2w, and a diffusion-weighted technique (DWI). Quantitative evaluation was performed by scoring LN numbers per volunteer and per scan. Qualitatively, scans were assessed on seven aspects, including LN contrast, anatomical information and insensitivity to motion during acquisition. Two T2w FSE methods showed the highest LN numbers (median 24 axillary), high contrast, excellent fat suppression, and relative insensitivity to motion during acquisition. A third T2w sequence and DWI showed significantly fewer LNs (14 and 10), and proved unsuitable due to motion sensitivity and geometrical uncertainties. T1w MRI showed an intermediate number of LNs (17), provided valuable anatomical information, but lacked LN contrast. Explicit LN imaging was achieved, in supine RT position, using MRI. Two T2w FSE techniques had the highest detection rates and were motion-insensitive. T1w MRI showed anatomical information. MRI enables direct delineation of individual LNs. Our optimized MRI scans enable accurate target definition in MRI-guided regional breast RT, and development of personalized treatments.

Introduction

The standard treatment for breast-cancer patients with tumour-positive sentinel node(s) or clinical axillary lymph node (LN) metastasis is axillary LN dissection (ALND). ALND has been shown to cause arm morbidity in up to 60% of the patients, including arm oedema, shoulder pain, and shoulder function restriction [1,2]. In patients with tumour-positive sentinel node(s), ALND is increasingly being omitted or replaced by regional radiotherapy (RT), based on recent results of the American College of Surgeons Oncology Group (ACOSOG) Z0011 study and the European Organization for Research and Treatment of Cancer (EORTC) *After Mapping of the Axilla: Radiotherapy or Surgery?* (AMAROS) trial [3–8]. In the latter, no difference was observed in regional recurrence rate, with decreased arm oedema in the RT group. RT-induced toxicity of all grades occurred in a median 14% of the patients [6].

Standard regional RT comprises irradiation of the LNs in the axilla with or without the supraclavicular area +/- internal mammary LNs. Conventionally, these LN areas are delineated on computed tomography (CT) scans. The contouring is performed following delineation guidelines defined by anatomical boundaries, since most LNs cannot be visualized with CT [9–11]. As a consequence, target volumes are relatively large (figure 1), resulting in large high-dose volumes in normal tissue, such as muscles, brachial plexus, lungs, heart, and connective tissue [6,12–15]. Complications associated with regional RT include arm oedema, decreased arm mobility, brachial plexopathy, and radiation pneumonitis.

More accurate target delineation could be achieved by more explicit LN imaging than currently achievable with CT. Direct visualization of regional LNs in relation to their surrounding organs-at-risk (OARs) is of utmost importance to accomplish a higher accuracy. Due to its superior soft-tissue contrast in particular, magnetic resonance imaging (MRI) may be more useful than CT on this aspect [16], and could facilitate individual LN delineation. Potentially, the implementation of MRI in RT planning can lead to smaller treated volumes.



● *Figure 1* Example of standard axillary delineations on CT in a breast-cancer patient in RT position. A transverse slice of the CT scan is shown (top), with the corresponding coronal view (bottom). Green is the clinical target volume (CTV) of the lower axilla for standard right-sided axillary RT; purple is the planning target volume (PTV, not indicated in the figure), which is generated by an expansion of the CTV by 5 mm isotropic. Target delineations are performed based on guidelines with the use of anatomical boundaries. As a consequence, target volumes are relatively large. Other delineated structures are the ipsilateral lung (red), contralateral lung (sky blue), and heart (dark blue).

Previous studies on LN imaging indicate an added value of diagnostic MRI, for several anatomical locations, including the axilla [17–22]. However, conventional diagnostic MRI techniques for breast-cancer patients are not suitable for regional RT planning. Conventional techniques are not optimized for visualization of all LNs, as they are primarily developed for imaging and staging of the tumour. Secondly, the scanning position is prone, which differs from the RT position, i.e. supine with abducted arms. Furthermore, diagnostic MRI scans for the breast are usually T1-weighted (T1w) images. As a result, on these images, LNs lack contrast with surrounding tissues, and as such, can go unnoticed. Additionally, since a breast coil is used conventionally, which does not cover the entire regional area, not all regional LNs are imaged. For these reasons, dedicated MRI techniques in supine RT position are required to be suitable in regional RT planning.

Accurate LN visualization using MRI is challenging, since several aspects need to be taken into account in the design of pulse sequences capable of making regional LNs visible. These elements include contrast of LNs relative to the surrounding tissue, resolution, geometric accuracy, sensitivity to motion during scan acquisition, and visibility of anatomical reference structures. Moreover, methods to suppress fat and blood signal are required to distinguish LNs from fatty tissue and nearby blood vessels. In particular, the success of fat suppression techniques can be influenced by the scanning position.

Since the aim of regional RT is to irradiate all regional LNs in the target area, the MRI technique should have a high sensitivity to detect individual LNs. To our knowledge, no previous study has been published which focused on MRI in supine RT position for this goal. In 10 healthy volunteers we have designed and optimized five clinically applicable MRI sequences to visualize individual axillary and supraclavicular LNs. Evaluation of these techniques is performed in another 12 healthy female volunteers. The objective of this work was to establish which MRI sequences best facilitate LN delineation in RT planning.

Methods and materials

All participants provided their written informed consent to participate in the study. The Internal Review Board of the University Medical Center (UMC) Utrecht approved this procedure. Scanning was performed at the Radiology and RT Department of UMC Utrecht from 2013 to 2015.

Volunteers and scanner set-up

Five MRI sequences were developed and optimized on image quality and scan time, in ten healthy female volunteers, whose age ranged from 24 – 54 yr. Subsequently, in 12 additional female volunteers, the optimized MRI scans were applied for evaluation. Age of the final 12 volunteers ranged from 23 – 49 yr, and the range of their body-mass-index ($BMI = weight / length^2$) was 19.4 – 31.2 kg/m². The subjects were scanned on a wide-bore 1.5 T Ingenia MRI scanner (Philips, Best, The Netherlands) in supine position, with a knee support. A 10° Thorawedge board (CIVCO Medical Solutions, Reeuwijk, The Netherlands) was used, and both arms were in abduction, resting on the board (RT position). An anterior FlexCoverage receive coil (Philips, Best, The Netherlands) was connected, placed on a custom-made, adjustable polymethyl methacrylate (PMMA) support to avoid deformation of the outer body contour, and secured to the table. A posterior receive coil (Philips, Best, The Netherlands) was situated in the patient table of the scanner (figure 2). No contrast agent was administered.

In total, the MRI scanning protocol was restricted to 20 minutes. Additional time in supine RT position of up to 10 min was required for subject positioning and scanning preparation. Endurance was monitored by noting whether a volunteer could finish the entire MRI scanning procedure without physical problems (e.g. pain in shoulder or arms). If not, the reason of insufficient endurance was noted.

MRI scans

The optimized MRI scans included 2-dimensional (2D) and 3D sequences. The field-of-view (FOV) for all scans was chosen to cover the breast, the axillary and supraclavicular regions, up to the mandible, and was 250 mm, 420 mm, and 100 mm in caudal-cranial (CC), right-left (RL), and



● *Figure 2 MRI scanning set-up. The volunteer is placed on a 10° Thorawedge board (CIVCO Medical Solutions, Reeuwijk, The Netherlands) in supine RT position, i.e. with arms in abduction, resting on the board. Scanning is performed with a 1.5 T Ingenia (Philips, Best, The Netherlands) wide-bore MRI scanner. An anterior FlexCoverage (Philips, Best, The Netherlands) receive coil is connected and placed on top of a custom-made PMMA support, which is adjustable, in order to prevent deformation of the outer body contour. A posterior receive coil (Philips, Best, The Netherlands) is located in the table.*

anterior-posterior (AP) directions, respectively. All images were acquired in the coronal plane. Clinical applicability was established by limiting the scan duration to a maximum of seven minutes per scan. Relevant scan parameters are summarized in table 1.

The sequences included a T1w 3D spoiled gradient echo (SPGR) technique, or T1-FFE. Water-only images from mDixon fat separation could be generated with the T1-FFE technique, which shows similar contrast of soft tissues to CT scans used for standard RT planning. Three T2-weighted (T2w) sequences were also applied, which included a 3D T2w steady state free precession (T2-FFE), and both 3D and 2D T2w fast spin echo (FSE) techniques (T2-VISTA, T2-TSE). T2 weighting yields inherently positive contrast of LNs but also requires a method for blood-signal and fat suppression to provide endogenous high contrast with blood and fat. In the T2-VISTA technique, T2 preparation with velocity encoding of 1 cm/s in CC and RL directions was applied by velocity-encoding preparation pulses, in order to eliminate signal from blood with a low flow velocity. The echo train lengths in T2-VISTA and T2-TSE were 65 and 33, respectively.

● *Table 1 Imaging parameters of the optimized MRI scans. The FOV for each scan was 250 mm, 420 mm, and 100 mm in CC, RL, and AP, respectively.*

Sequences	T1-FFE	T2-FFE	T2-VISTA	T2-TSE	DWI
<i>Imaging parameters</i>					
TR/TE (ms)	5.7 / 1.9 / 3.8 ^a	12 / 4.8	155 / 2000	4500 / 100 / 2 ^b	6147 / 80
Fat suppression	mDixon	ProSet	SPAIR	mDixon	SPAIR
Dimensionality	3D	3D	3D	2D	2D
Acquired resolution	1.0 × 1.0 × 2.2 mm ³	0.7 × 0.7 × 2.0 mm ³	1.0 × 1.0 × 2.0 mm ³	0.7 × 0.7 mm ²	3.0 × 3.0 mm ²
BW / pixel (Hz)	719	134	439	434	29
Slice thickness (mm)	-	-	-	3.0	3.0
Diffusion <i>b</i> values (s/mm ²)	-	-	-	-	0, 200, 400, 1000
Preparation / pre-pulse	-	-	$v_{enc} = 1.0$ cm/s (CC and RL)	-	-
Scan time (m:ss)	3:06	6:30	3:24	4:50	2:15

T1-FFE = T1-weighted fast field echo; T2-FFE = T2-weighted fast field echo; T2-VISTA = T2-weighted Volumetric Isotropic T2-weighted Acquisition; T2-TSE = T2-weighted turbo spin echo; DWI = diffusion-weighted imaging; TR = repetition time; TE = echo time; FFE = fast field echo; VISTA = Volumetric Isotropic T2w Acquisition; TSE = turbo spin echo; mDixon = multi-point Dixon; SPAIR = Spectral Attenuated Inversion Recovery; BW = bandwidth; v_{enc} = velocity encoding; CC = caudo-cranial; RL = right-left.

^a TR/TE1/TE2 (ms); ^b TR/TE/ATE (ms).

Finally, diffusion-weighted single-shot spin echo, echo planar imaging (DWI) with 4 b -values (up to $b = 1000 \text{ s/mm}^2$) was performed. Signal preservation in DWI reflects motion restriction of water molecules. Water motion is more restricted in LNs than in background tissue, and thus has higher signal intensity. A scan time of less than three minutes could be used for DWI, since resolution and signal-to-noise ratio (SNR) could not be improved by simply prolonging scan time. A known drawback of DWI is geometric distortions due to magnetic-field susceptibility artefacts [23]. Hence, the geometric reliability is limited, which can be determined by taking into account the pixel bandwidth (BW) and resolution (table 1).

Fat suppression

On both T1w and T2w MRI, fat has high signal intensity. However, contrast between fat and LNs on T1w images is higher than on T2w scans. Since most LNs are located in or near fatty tissue, a method to suppress fat signal was applied in T2w MRI sequences. In the T1w sequence, a water-fat separation method was used because it was not obvious whether fat-suppressed images were beneficial.

One technique to suppress fat signal, applied in T2-VISTA and DWI, is Spectral Attenuated Inversion Recovery (SPAIR). In SPAIR, an adiabatic frequency-selective inversion pulse is used to invert the magnetization which originated from fat, followed by spoilers [24,25].

Another method is to separate water and fat. This was applied in the T1-FFE and T2-TSE scans, with multi-point Dixon (mDixon). In this technique, multiple echoes are used to separate water and fat based on the phase and magnitude of the acquired signals. Therefore, it can provide both water-suppressed and fat-suppressed images [26,27].

The third method for fat-signal suppression, performed in T2-FFE, uses binomial water-selective pulses, or Principle of Selective Excitation Technique (ProSet), consisting of a composite radiofrequency pulse with pre-defined flip angles and time intervals. The fat suppression is provided by exploiting the dephasing of fat and water [24,25].

Lymph node detection rates and statistics

As a quantitative evaluation of the MRI sequences, the numbers of right-sided axillary and supraclavicular LNs were determined in each scan for each volunteer. This was performed independently of the other MRI scans available for that volunteer. The scoring process was performed by one researcher who was extensively trained to identify regional LNs on MRI. During several inter-disciplinary meetings, the researcher, together with a breast radiologist, a breast radiation oncologist, an MRI physicist, and a clinical physicist, assessed all MRI techniques, and identified LNs. The team discussed regularly, in order to establish consensus on anatomical structure identification on the MRI sequences.

After the scoring process was completed, statistical analysis was performed by paired Wilcoxon signed-rank tests, between the LN detection rates in each MRI technique, for both LN areas. A significant difference is indicated by $p < 0.05$.

Imaging assessment

The MR images were assessed qualitatively by an experienced breast radiologist. For LN detection, maximum intensity projections (MIPs) of three slices were used to increase SNR and increase LN detection in T2-FFE and T2-VISTA. In both T1-FFE and T2-TSE, the water image of mDixon was used for evaluation. For evaluation of DWI scans, the highest diffusion weighting was chosen, i.e. $b = 1000 \text{ s/mm}^2$.

The following aspects were evaluated in view of suitability for LN delineation: contrast of the LNs to the surrounding tissue, suppression of blood signal, fat suppression in the axillary and supraclavicular areas, visibility of anatomical reference structures – which is essential for localizing LNs –, susceptibility to motion artefacts of the sequences, and SNR. The qualitative parameters were determined visually and given a score of ‘- -’ (very poor), ‘-’ (poor), ‘+/-’ (average), ‘+’ (good), or ‘++’ (excellent), on a five-point Likert scale, cf. [28,29].

Results

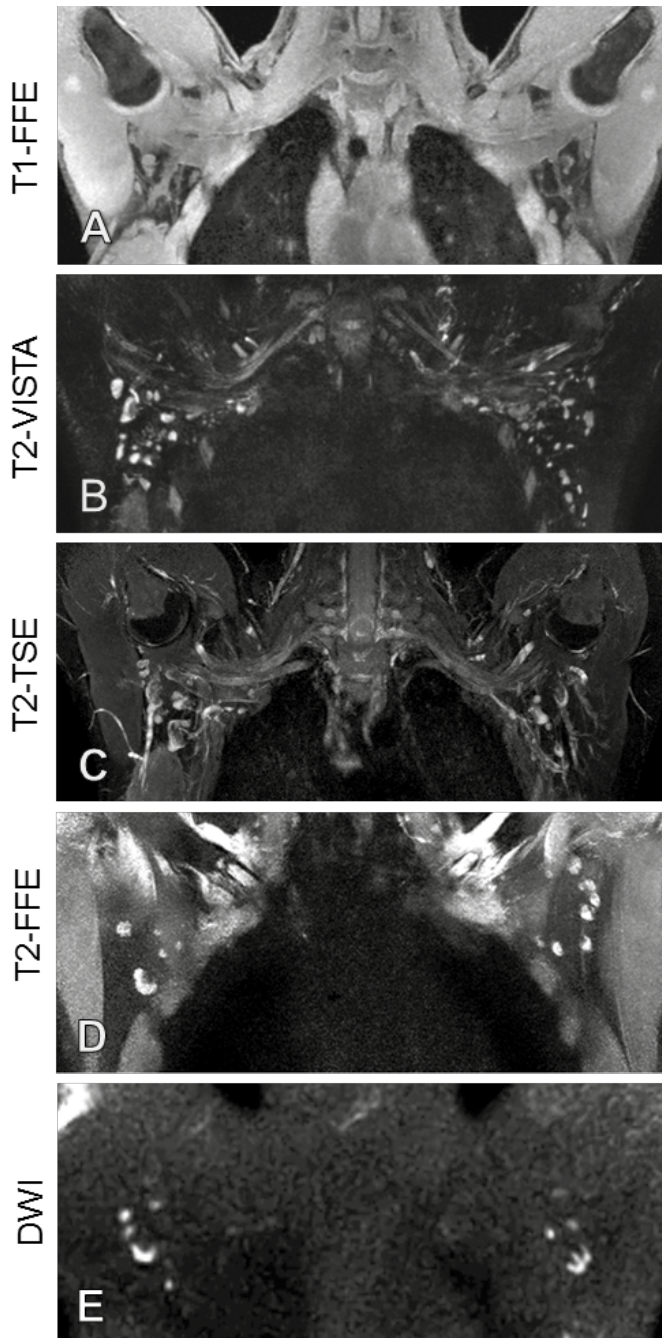
Endurance for undergoing the MRI procedure was excellent in all volunteers. MRI of regional healthy LNs was achieved in the final 12 volunteers using the five optimized sequences (figures 3 and 4). All numbers of right-sided LNs determined per volunteer and per scan, are listed in table 2, and represented in figure 5. The results of the qualitative evaluation are summarized in table 3.

Quantitative evaluation

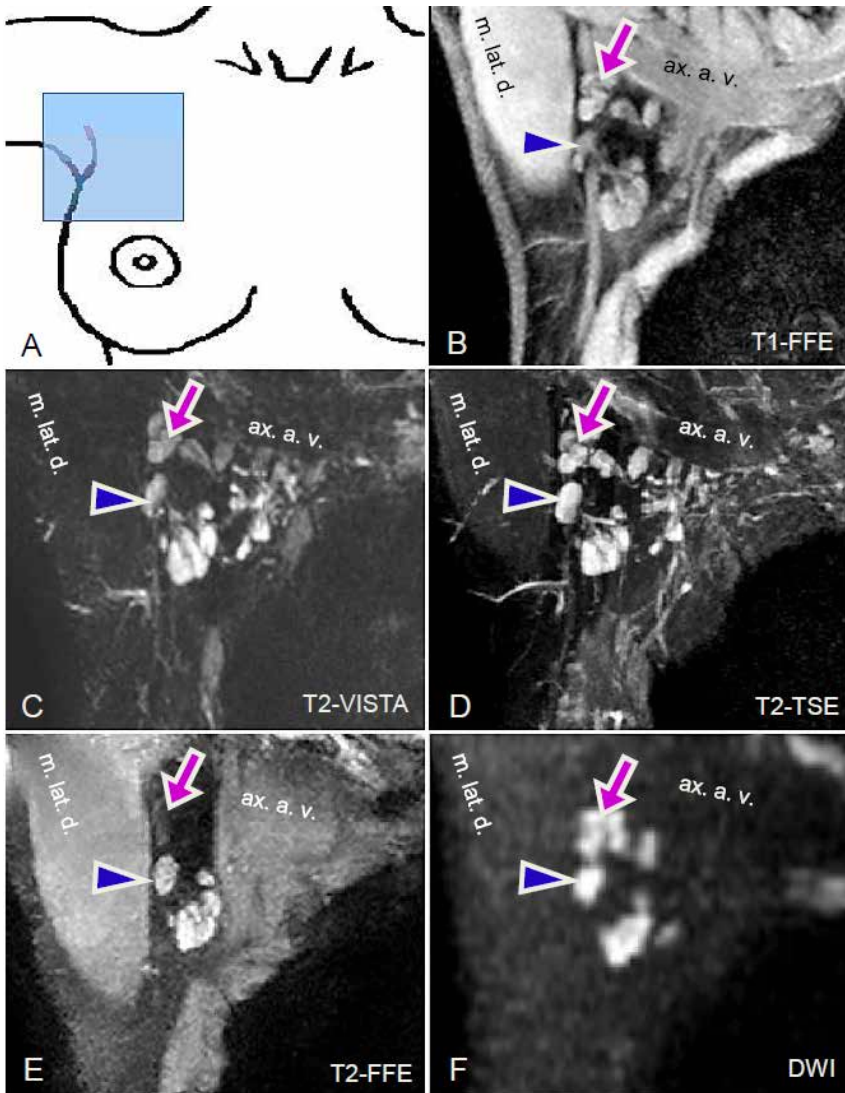
Of the five MRI techniques, the two T2w FSE techniques proved to have the highest LN detection rates (table 2, figure 5). T2-VISTA showed the highest numbers in all 12 volunteers: up to 44 axillary (median: 24) and up to 5 supraclavicular LNs (median: 2) were detected. Statistical significances from the paired Wilcoxon signed-rank tests are indicated with respect to T2-VISTA in figure 5.

T2-TSE showed similar numbers, at a median of 23 axillary and 2 supraclavicular LNs (ranges: 11 – 40, and 0 – 4 respectively). No difference was found between the two T2w FSE methods for either the axillary ($p = 0.47$) or supraclavicular ($p = 0.39$) LNs. The median number of axillary LNs identified with T1-FFE was 17, ranging between 10 and 21. This was higher than in T2-FFE (median 14, range: 9 – 19, $p = 0.01$). Moreover, T1-FFE showed a range of 0 – 4 supraclavicular LNs, compared to the range of 0 – 2 found in T2-FFE, both showing a median number of one LN ($p = 0.05$). Finally, the number of LNs counted in the DWI scans was lowest in all subjects at a median of 10 axillary LNs. Moreover, in ten out of twelve subjects, no supraclavicular LNs could be identified with the DWI technique, while only one supraclavicular LN was found in the other two volunteers. LN detection rate of DWI was by far the lowest of the five techniques ($p = 0.001$ axillary, $p = 0.002$ supraclavicular).

In the T2-VISTA and T2-TSE scans, the number of axillary LNs was significantly higher than for T1-FFE, T2-FFE, and DWI ($p = 0.002$, $p = 0.002$, $p = 0.001$, respectively). This was also true for the supraclavicular LNs in T2-FFE and DWI ($p = 0.002$ for both), but not for T1-FFE ($p = 0.26$).



● *Figure 3* Coronal slices showing axillary LNs in five volunteers bilaterally, visualized with MRI. The MRI techniques represented are (A) T1-FFE (water-only image); (B) T2-VISTA; (C) T2-TSE (water-only image); (D) T2-FFE; (E) DWI ($b = 1000 \text{ s/mm}^2$). For the T1-FFE, T2-VISTA and T2-FFE examples, maximum intensity projections of three slices were used to increase SNR and to cover the same volume as in the T2-TSE and DWI.

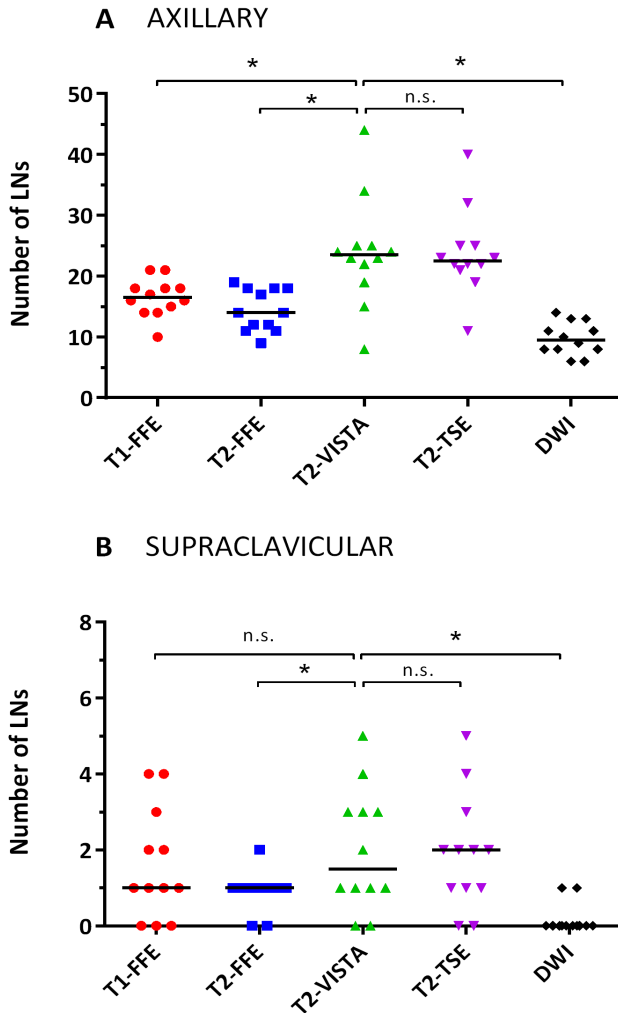


● *Figure 4 Coronal slices showing right-sided axillary LNs in one volunteer, visualized with MRI. The slices shown are cropped to approximately 80 x 80 mm². Location with respect to anatomy is depicted schematically by the blue square in (A). MRI techniques represented are (B) T1-FFE (water-only image); (C) T2-VISTA; (D) T2-TSE (water-only image); (E) T2-FFE; (F) DWI (b = 1000 s/mm²). For the T2-VISTA and T2-FFE examples, maximum intensity projections (MIPs) of three slices were used to increase SNR and to cover the same volume as in the T2-TSE and DWI. The purple arrow indicates LNs, apparent in T1-FFE, T2-VISTA, DWI and T2-TSE, but obscured in T2-FFE due to a pulsating artery nearby. The blue arrowhead indicates a LN that is clearly identifiable in the T2w and DWI sequences, but lacks contrast in T1-FFE. M. lat. d. = musculus latissimus dorsi; ax. a. v. = axillary arteria and vein.*

● *Table 2 Numbers of right-sided axillary/supraclavicular LNs identified in each volunteer per MRI scan. Results from scans in healthy female volunteers (n = 12). Numbers are denoted: axillary LNs / supraclavicular LNs. For this evaluation, in T1-FFE and T2-TSE, only the water image from the mDixon method was taken into account. For DWI, the highest diffusion weighting (b = 1000 s/mm²) was used.*

<i>Technique</i>	T1-FFE	T2-FFE	T2-VISTA	T2-TSE	DWI
<i>Volunteer</i>					
1	21 / 1	19 / 1	44 / 5	40 / 4	8 / 0
2	15 / 1	14 / 1	24 / 1	22 / 2	11 / 0
3	16 / 3	17 / 1	24 / 3	25 / 1	9 / 0
4	16 / 4	18 / 1	34 / 4	32 / 5	10 / 0
5	21 / 2	18 / 0	23 / 1	23 / 1	8 / 0
6	18 / 0	18 / 0	25 / 0	22 / 0	13 / 0
7	14 / 0	9 / 1	19 / 1	19 / 2	6 / 0
8	10 / 1	11 / 1	8 / 0	11 / 0	6 / 0
9	14 / 1	12 / 1	15 / 1	25 / 2	11 / 0
10	17 / 4	12 / 2	25 / 3	22 / 2	13 / 0
11	18 / 0	14 / 1	23 / 2	23 / 1	8 / 1
12	18 / 2	11 / 1	22 / 3	21 / 3	14 / 1

LN = lymph node; MRI = magnetic resonance imaging; T1-FFE = T1-weighted fast field echo; T2-FFE = T2-weighted fast field echo; T2-VISTA = T2-weighted Volumetric ISotropic T2-weighted Acquisition; T2-TSE = T2-weighted turbo spin echo; DWI = diffusion-weighted imaging; LNs = lymph nodes; supraclav. = supraclavicular.



● Figure 5 Numbers of LNs identified in images acquired with different MR sequences. For both (A) the axilla and (B) the supraclavicular area, the numbers of detected LNs are denoted, per MRI technique, for all 12 volunteers. Note that the y-axes in (A) and (B) differ. T1-FFE is denoted by red dots, T2-FFE by blue squares, T2-VISTA by green triangles pointing upwards, T2-TSE by purple triangles pointing downwards, and DWI by black diamonds. Black horizontal lines indicate the median values. Statistical significances from paired Wilcoxon signed-rank tests are indicated with respect to T2-VISTA. Here, ‘*’ means $p < 0.05$, and ‘n.s.’ denotes non-significance, or $p > 0.05$.

Qualitative evaluation

T1-FFE yielded excellent water-fat separation with mDixon and the high resolution clearly showed individual LNs in the axilla and supraclavicular area. However, in the water image of mDixon, the signal of some LNs blended in with the surrounding soft tissue and blood vessels, thereby impeding identification of small structures. Anatomical landmarks, such as pectoral and deltoid muscles and arteries, were clearly visible and could be used as structural references. The technique proved to be relatively insensitive to motion. Furthermore, the SNR was good (table 3, figures 4).

T2-FFE showed high contrast of the LNs in high resolution and excellent suppression of blood due to intrinsic diffusion weighting, but the water-selective binomial pulses resulted in poor fat suppression in the supraclavicular region (figure 4). Furthermore, some LNs located near pulsating arteries were obscured due to motion (figure 4). Obscuration of LNs was also observed after gross motion of the volunteer during scanning. The latter was evident in two volunteers. The high susceptibility to motion artefacts affects T2-FFE to a large extent. Moreover, the SNR in T2-FFE was relatively low (table 3).

Both FSE techniques showed high T2 contrast of the LNs, with successful fat suppression in the axilla. In the supraclavicular area, fat was excellently suppressed by mDixon in the water-only image of T2-TSE, but SPAIR fat suppression in T2-VISTA failed in four cases. The regional LNs could clearly be identified in both FSE scans, and even minute LNs were detectable. However, both FSE sequences still showed some remaining blood signal. Additionally, T2-VISTA showed slightly more blurring than T2-TSE. In the latter, anatomical reference structures, such as the pectoral and deltoid muscles, were better visible than in the T2-VISTA scans. Both T2w FSE sequences were robust for motion. SNR of the FSE images was average and good, for T2-VISTA and T2-TSE, respectively (table 3, figures 4). In one case, however, T2-VISTA was greatly outperformed by T2-TSE in terms of LNs contrast and SNR.

Finally, DWI yielded high LN contrast relative to all surrounding tissue, but it has an inherently low resolution. Furthermore, no anatomical reference structures were clearly visible in DWI due to very efficient background

suppression. The technique proved to be very insensitive to motion during acquisition. Nevertheless, DWI yielded low SNR (table 3, figures 4). Furthermore, visual inspection suggested geometric inaccuracies, due to the high sensitivity to magnetic-field variations, which led to pixel shifts of up to 15 mm. Analogously to T2-VISTA, SPAIR fat suppression in DWI worked successfully in the axillary region, but failed in four cases in the supraclavicular area.

● *Table 3 Qualitative evaluation of the MRI sequences. Results from scans in healthy female volunteers (n = 12), determined visually. Classifications on a five-point Likert scale: ‘++’ = excellent; ‘+’ = good; ‘+/-’ = average; ‘-’ = poor; ‘--’ = very poor. In T1-FFE and T2-TSE, mDixon was applied, while in T2-FFE, ProSet was used for fat suppression. In T2-VISTA and DWI, fat was suppressed by SPAIR. For this evaluation, only the water image from the mDixon method was taken into account. The highest diffusion weighting (b = 1000 s/mm²) was used for evaluation of DWI.*

Sequence	T1- FFE	T2-FFE	T2-VISTA	T2-TSE	DWI
<i>Qualitative parameters</i>					
Contrast of LNs	-	+	+	+	++
Axillary fat suppression	++	+	+	++	+
Supraclavicular fat suppression	++	-	+	++	+/-
Blood suppression	N.A.	++	+	+	++
Visibility of anatomical reference structures	++	+/-	+/-	+	--
Insusceptibility to motion artifacts	++	--	+	+	-
SNR	+	-	+/-	+	+/-

T1-FFE = T1-weighted fast field echo; T2-FFE = T2-weighted fast field echo; T2-VISTA = T2-weighted Volumetric Isotropic T2-weighted Acquisition; T2-TSE = T2-weighted turbo spin echo; DWI = diffusion-weighted imaging; LNs = lymph nodes; N.A. = not applicable; SNR = signal-to-noise ratio.

Discussion

As a first step towards MRI-guided regional breast RT, this study explored MRI for visualizing healthy LNs in supine RT position. Five clinically applicable MRI sequences were optimized in 10 female healthy volunteers, and subsequently evaluated in another 12 female healthy volunteers. Evaluation of the MRI methods was aimed at the potential suitability for LN delineation in RT planning.

Although MRI for axillary LN imaging is thoroughly studied [30], MRI studies for target delineation in regional breast RT are scarce. Diagnostic MRI is performed for staging of the tumour and/or regional LNs, and scans are usually acquired in prone position. These techniques include contrast-enhanced T1w MRI methods, as well as T2w sequences and DWI [22,31]. LN staging is usually based on size of LNs, relative T2 values, morphology, contrast agent uptake, or a combination of these [32]. Recently, DWI has become popular due to the high signal intensity of LNs relative to surrounding tissue [33,34]. Furthermore, apparent diffusion coefficients can be calculated from DWI for an indication for malignancy. In contrast to these diagnostic methods, the MRI techniques presented here are acquired in supine RT position, without administration of contrast agent, using anterior and posterior receive coils. They were specifically optimized to image regional LNs explicitly for RT planning.

Two FSE techniques – T2-VISTA and T2-TSE – showed the highest LN detection rates, while being relatively insensitive to motion during acquisition. Both sequences have specific advantages and limitations. Contrast of LNs relative to the background is high in both techniques due to successful fat suppression, such that individual LNs could be directly identified. The techniques differ in resolution, as the T2-TSE is a multi-slice method with 3-mm slices, which might be a disadvantage for accuracy in target delineation. T2-VISTA has 1-mm isotropic resolution, but showed some blurring due to a long echo train. Although both sequences were optimized to show black blood, some signal remained visible in axillary blood vessels. Additional T2 weighting induced by the preparation pulses for velocity encoding caused loss of background signal. In one volunteer, this degraded SNR and LN contrast severely in the T2-VISTA.

T1-FFE showed fewer LNs, as contrast between LNs and blood vessels or muscles is lacking, due to the limited T1 differences between these tissues. Consequently, LNs could be unnoticed or other structures could be misidentified to be LNs. This issue could be addressed by including water-fat images provided by mDixon. A fatty core might help to differentiate a LN from other tissues. Presence of anatomical information makes the robust T1-FFE sequence valuable for RT planning, and complementary to the T2w FSE techniques. Furthermore, T2-FFE proved to be unsuitable since LNs are obscured due to motion. Finally, DWI, while robust for motion artefacts due to rapid image acquisition, and showing high LN contrast at high b -values, suffered from geometric inaccuracies and low resolution, which is inherent to echo planar imaging (EPI) based sequences.

Since most regional LNs are located in or near fatty tissue, a method for suppression of fat signal was applied. Fat-suppression techniques can be adversely affected by B_0 inhomogeneities. These are found particularly in the supraclavicular area, due to ubiquitous tissue-air transitions and sharp curvature of the outer contour. In our study, mDixon proved to be very reliable – even in subjects with a high BMI (up to 31.2 kg/m²). The mDixon method is relatively insensitive to B_0 irregularities [26,27,35], but the use of multiple echoes requires a longer scan duration. Conversely, the water-selective binomial pulse ProSet performed poorly due to B_0 non-uniformities. SPAIR, as frequency-selective inversion pulse, was only slightly impaired.

The gold standard for the total number of LNs is not available. Therefore, the key question is how accurate the MRI sequence of choice is. In previous imaging (including MRI, CT, and ultrasonography) and histological studies [36–43], numbers of axillary LNs, both benign and malignant, ranged between 6 and 45, emphasizing large (anatomical) variation between subjects. In these studies, the goal was to compare diagnostic values of imaging techniques in correlation with histology, rather than establish LN detection capability. Histological information, usually after ALND, is limited to the lower axilla (i.e. axillary levels I and II), while our work aimed to image LNs in the entire regional area (i.e. axillary level I, II, III and supraclavicular region). Numbers of axillary LNs detected with the MRI sequences in our work fall in the reported range. Finally, numbers of LNs observed in the supraclavicular region were within the expected

range of 1 – 10 LNs [41]. This region is particularly difficult, due to large pulsating blood vessels which were not always adequately suppressed in the FSE scans, thereby possibly impairing localization of small LNs there.

This study showed the technical feasibility of explicitly visualizing healthy LNs using MRI in volunteers. Furthermore, endurance to undergo the entire MRI procedure was excellent. Quantitative and qualitative analyses indicated that MRI, and in particular the T2w FSE and T1-FFE sequences, could be excellent tools for explicit LN delineation. In order to assess the added value of these methods for RT planning, the next step will be MRI in breast-cancer patients. In our study, a large range of BMI was chosen (19.4 – 31.2 kg/m²) to reflect the expected patient population, but several issues remain to be investigated. Endurance and anatomy in patients are likely to differ from those in the healthy volunteers. LN morphology could also change with age [44,45]. Moreover, any axillary surgery (e.g. sentinel-node biopsy) might affect LN detection rates in MRI. These aspects, as well as image quality and patient set-up reproducibility [46], are under investigation in a patient study that is ongoing at UMC Utrecht. Patient data will also allow a comparison of MRI and CT scans, both in supine RT position.

The MRI techniques presented potentially have a high added value for clinical practice. Localizing individual LNs may lead to adaptation of standard target volumes [37], as currently defined on CT. A possible consequence of MRI guidance is smaller treatment fields and, thus, reduced treated volume. This may result in a lower integral dose, OARs sparing and, thereby, a reduction of RT-induced toxicity. Furthermore, combining RT with dedicated MRI could enable more selective regional RT. However, in the current clinical situation, due to set-up uncertainties of regional RT, introducing these new RT techniques requires LN visualization while the patient is treated. On-line MRI guidance could achieve this, as enabled by the UMC Utrecht MRI/linear accelerator (MRL) [47]. Relative to current treatment techniques, the MRL and other MRI/RT modalities [48,49] could allow for personalized treatments, such as stereotactic RT of individual tumour-positive LNs. For such advanced RT techniques, methods for identifying metastatic LNs on MRI, with a high sensitivity, could be beneficial [19]. Ultimately, breast-cancer patients may benefit from the many possibilities of MRI of the regional LNs.

Conclusions

Identification of individual axillary and supraclavicular LNs is feasible with MRI in supine RT position. Two T2w FSE techniques were robust and showed the highest numbers of LNs, while a T1-FFE method provided the most anatomical information. Fat separation by mDixon performed excellently. This work serves as a required first step to investigate MRI guidance in regional RT for breast-cancer patients. By identifying individual LNs, MRI-based target delineation could reduce target volumes, and thereby further reduce RT-induced toxicity in the future.

References

- [1] Ivens D, Hoe AL, Podd TJ, Hamilton CR, Taylor I, Royle GT. Assessment of morbidity from complete axillary dissection. *Br J Cancer* 1992;66:136–8.
- [2] Kakuda JT, Stuntz M, Trivedi V, Klein SR, Vargas HI. Objective assessment of axillary morbidity in breast cancer treatment. *Am Surg* 1999;65:995–8.
- [3] Giuliano AE, McCall L, Beitsch P, Whitworth PW, Blumencranz P, Leitch AM, et al. Locoregional recurrence after sentinel lymph node dissection with or without axillary dissection in patients with sentinel lymph node metastases: the American College of Surgeons Oncology Group Z0011 randomized trial. *Ann Surg* 2010;252:426–32-3. doi:10.1097/SLA.0b013e3181f08f32.
- [4] Senn H-J, Thürlimann B, Galimberti V, Chifu C, Rodriguez Perez S, Veronesi P, et al. Positive axillary sentinel lymph node: Is axillary dissection always necessary? *The Breast* 2011;20:S96–8.
- [5] Jagsi R, Chadha M, Moni J, Ballman K, Laurie F, Buchholz TA, et al. Radiation Field Design in the ACOSOG Z0011 (Alliance) Trial. *J Clin Oncol* 2014. doi:10.1200/JCO.2014.56.5838.
- [6] Donker M, van Tienhoven G, Straver ME, Meijnen P, van de Velde CJH, Mansel RE, et al. Radiotherapy or surgery of the axilla after a positive sentinel node in breast cancer (EORTC 10981-22023 AMAROS): a randomised, multicentre, open-label, phase 3 non-inferiority trial. *Lancet Oncol* 2014;15:1303–10. doi:10.1016/S1470-2045(14)70460-7.
- [7] Galimberti V, Cole BF, Zurrada S, Viale G, Luini A, Veronesi P, et al. Axillary dissection versus no axillary dissection in patients with sentinel-node micrometastases (IBCSG 23-01): a phase 3 randomised controlled trial. *Lancet Oncol* 2013;14:297–305. doi:10.1016/S1470-2045(13)70035-4.
- [8] DiSipio T, Rye S, Newman B, Hayes S. Incidence of unilateral arm lymphoedema after breast cancer: a systematic review and meta-analysis. *Lancet Oncol* 2013;14:500–15. doi:10.1016/S1470-2045(13)70076-7.
- [9] Li XA, Tai A, Arthur DW, Buchholz TA, Macdonald S, Marks LB, et al. Variability of target and normal structure delineation for breast cancer radiotherapy: an RTOG Multi-Institutional and Multiobserver Study. *Int J Radiat Oncol Biol Phys* 2009;73:944–51. doi:10.1016/j.ijrobp.2008.10.034.
- [10] Nielsen MH, Berg M, Pedersen AN, Andersen K, Glavicic V, Jakobsen EH, et al. Delineation of target volumes and organs at risk in adjuvant radiotherapy of early breast cancer: national guidelines and contouring atlas by the Danish Breast Cancer Cooperative Group. *Acta Oncol* 2013;52:703–10. doi:10.3109/0284186X.2013.765064.
- [11] Offersen B V, Boersma LJ, Kirkove C, Hol S, Aznar MC, Biete Sola A, et al. ESTRO consensus guideline on target volume delineation for elective radiation therapy of early stage breast cancer. *Radiother Oncol* 2015;114:3–10. doi:10.1016/j.radonc.2014.11.030.
- [12] Hoebbers FJ, Borger JH, Hart AA, Peterse JL, Th EJ, Lebesque J V. Primary axillary radiotherapy as axillary treatment in breast-conserving therapy for patients with breast carcinoma and clinically negative axillary lymph nodes. *Cancer* 2000;88:1633–42.
- [13] Bentzen SM, Dische S. Morbidity related to axillary irradiation in the treatment of breast cancer. *Acta Oncol* 2000;39:337–47.
- [14] Coen JJ, Taghian AG, Kachnic LA, Assaad SI, Powell SN. Risk of lymphedema after regional nodal irradiation with breast conservation therapy. *Int J Radiat Oncol Biol Phys* 2003;55:1209–15.

- [15] Sanuki N, Takeda A, Amemiya A, Ofuchi T, Ono M, Ogata H, et al. Outcomes of clinically node-negative breast cancer without axillary dissection: can preserved axilla be safely treated with radiation after a positive sentinel node biopsy? *Clin Breast Cancer* 2013;13:69–76. doi:10.1016/j.clbc.2012.09.005.
- [16] Dooms GC, Hricak H, Crooks LE, Higgins CB. Magnetic resonance imaging of the lymph nodes: comparison with CT. *Radiology* 1984;153:719–28. doi:10.1148/radiology.153.3.6093190.
- [17] van den Brekel MW. Lymph node metastases: CT and MRI. *Eur J Radiol* 2000;33:230–8. doi:10.1016/S0720-048X(99)00145-X.
- [18] Hövels AM, Heesakkers RAM, Adang EM, Jager GJ, Strum S, Hoogeveen YL, et al. The diagnostic accuracy of CT and MRI in the staging of pelvic lymph nodes in patients with prostate cancer: a meta-analysis. *Clin Radiol* 2008;63:387–95. doi:10.1016/j.crad.2007.05.022.
- [19] Harnan SE, Cooper KL, Meng Y, Ward SE, Fitzgerald P, Papaioannou D, et al. Magnetic resonance for assessment of axillary lymph node status in early breast cancer: a systematic review and meta-analysis. *Eur J Surg Oncol* 2011;37:928–36. doi:10.1016/j.ejso.2011.07.007.
- [20] Li X-T, Sun Y-S, Tang L, Cao K, Zhang X-Y. Evaluating local lymph node metastasis with magnetic resonance imaging, endoluminal ultrasound and computed tomography in rectal cancer: a meta-analysis. *Colorectal Dis* 2015. doi:10.1111/codi.12909.
- [21] Menezes GL, Knuttel FM, Stehouwer BL, Pijnappel RM, van den Bosch MA. Magnetic resonance imaging in breast cancer: A literature review and future perspectives. *World J Clin Oncol* 2014;5:61–70. doi:10.5306/wjco.v5.i2.61.
- [22] Bazan JG, White J. Imaging of the axilla before preoperative chemotherapy: Implications for postmastectomy radiation. *Cancer* 2014. doi:10.1002/cncr.28859.
- [23] Le Bihan D, Poupon C, Amadon A, Lethimonnier F. Artifacts and pitfalls in diffusion MRI. *J Magn Reson Imaging* 2006;24:478–88. doi:10.1002/jmri.20683.
- [24] de Kerviler E, Leroy-Willig A, Clément O, Frija J. Fat suppression techniques in MRI: an update. *Biomed Pharmacother* 1998;52:69–75. doi:10.1016/S0753-3322(98)80006-1.
- [25] Delfaut EM, Beltran J, Johnson G, Rousseau J, Marchandise X, Cotten A. Fat suppression in MR imaging: techniques and pitfalls. *Radiographics* 1999;19:373–82. doi:10.1148/radiographics.19.2.g99mr03373.
- [26] Dixon WT. Simple proton spectroscopic imaging. *Radiology* 1984;153:189–94. doi:10.1148/radiology.153.1.6089263.
- [27] Eggers H, Brendel B, Duijndam A, Herigault G. Dual-echo Dixon imaging with flexible choice of echo times. *Magn Reson Med* 2011;65:96–107. doi:10.1002/mrm.22578.
- [28] Taron J, Martirosian P, Schwenzler NF, Erb M, Kuestner T, Weiß J, et al. Scan time minimization in hepatic diffusion-weighted imaging: evaluation of the simultaneous multislice acceleration technique with different acceleration factors and gradient preparation schemes. *MAGMA* 2016. doi:10.1007/s10334-016-0553-4.
- [29] Rauscher GH, Conant EF, Khan JA, Berbaum ML. Mammogram image quality as a potential contributor to disparities in breast cancer stage at diagnosis: an observational study. *BMC Cancer* 2013;13:208. doi:10.1186/1471-2407-13-208.
- [30] Kuijs VJL, Moosdorff M, Schipper RJ, Beets-Tan RGH, Heuts EM, Keymeulen KBMI, et al. The role of MRI in axillary lymph node imaging in breast cancer patients: a systematic review. *Insights Imaging* 2015;6:203–15. doi:10.1007/s13244-015-0404-2.
- [31] Schacht D V, Drukker K, Pak I, Abe H, Giger ML. Using quantitative image analysis to classify axillary lymph nodes on breast MRI: a new application for the Z 0011 Era. *Eur J Radiol* 2015;84:392–7. doi:10.1016/j.ejrad.2014.12.003.

- [32] Harnan SE, Cooper KL, Meng Y, Ward SE, Fitzgerald P, Papaioannou D, et al. Magnetic resonance for assessment of axillary lymph node status in early breast cancer: A systematic review and meta-analysis. *Eur J Surg Oncol* 2011;37:928–36.
- [33] Kamitani T, Hatakenaka M, Yabuuchi H, Matsuo Y, Fujita N, Jinnouchi M, et al. Detection of axillary node metastasis using diffusion-weighted MRI in breast cancer. *Clin Imaging* 37:56–61. doi:10.1016/j.clinimag.2012.02.014.
- [34] Kim EJ, Kim SH, Kang BJ, Choi BG, Song BJ, Choi JJ. Diagnostic value of breast MRI for predicting metastatic axillary lymph nodes in breast cancer patients: Diffusion-weighted MRI and conventional MRI. *Magn Reson Imaging* 2014. doi:10.1016/j.mri.2014.07.001.
- [35] Leiner T, Habets J, Versluis B, Geerts L, Alberts E, Blanken N, et al. Subtractionless first-pass single contrast medium dose peripheral MR angiography using two-point Dixon fat suppression. *Eur Radiol* 2013;23:2228–35. doi:10.1007/s00330-013-2833-y.
- [36] Luciani A, Pigneur F, Ghozali F, Dao T-H, Cunin P, Meyblum E, et al. Ex vivo MRI of axillary lymph nodes in breast cancer. *Eur J Radiol* 2009;69:59–66. doi:10.1016/j.ejrad.2008.07.040.
- [37] MacDonald SM, Harisinghani MG, Katkar A, Napolitano B, Wolfgang J, Taghian AG. Nanoparticle-enhanced MRI to evaluate radiation delivery to the regional lymphatics for patients with breast cancer. *Int J Radiat Oncol Biol Phys* 2010;77:1098–104. doi:10.1016/j.ijrobp.2009.06.002.
- [38] Korteweg MA, Zwanenburg JJM, van Diest PJ, van den Bosch MAAJ, Luijten PR, van Hillegerberg R, et al. Characterization of ex vivo healthy human axillary lymph nodes with high resolution 7 Tesla MRI. *Eur Radiol* 2011;21:310–7. doi:10.1007/s00330-010-1915-3.
- [39] Jiang J, He Q, Yang X, Liang Y, Fan L, Zhang Y, et al. Contribution of minute axillary lymph nodes to accurate staging for patients with breast cancer. *Chin Med J (Engl)* 2007;120:1762–5.
- [40] Nakai G, Matsuki M, Harada T, Tanigawa N, Yamada T, Barentsz J, et al. Evaluation of axillary lymph nodes by diffusion-weighted MRI using ultrasmall superparamagnetic iron oxide in patients with breast cancer: initial clinical experience. *J Magn Reson Imaging* 2011;34:557–62. doi:10.1002/jmri.22651.
- [41] Ying M, Ahuja A. Sonography of Neck Lymph Nodes. Part I: Normal Lymph Nodes. *Clin Radiol* 2003;58:351–8. doi:10.1016/S0009-9260(02)00584-6.
- [42] Willoughby TR, Kupelian PA, Pouliot J, Shinohara K, Aubin M, Roach M, et al. Target localization and real-time tracking using the Calypso 4D localization system in patients with localized prostate cancer. *Int J Radiat Oncol Biol Phys* 2006;65:528–34. doi:10.1016/j.ijrobp.2006.01.050.
- [43] Baltzer PAT, Dietzel M, Burmeister HP, Zoubi R, Gajda M, Camara O, et al. Application of MR mammography beyond local staging: is there a potential to accurately assess axillary lymph nodes? evaluation of an extended protocol in an initial prospective study. *AJR Am J Roentgenol* 2011;196:W641-7. doi:10.2214/AJR.10.4889.
- [44] Hadamitzky C, Spohr H, Debertin AS, Guddat S, Tsokos M, Pabst R. Age-dependent histoarchitectural changes in human lymph nodes: an underestimated process with clinical relevance? *J Anat* 2010;216:556–62. doi:10.1111/j.1469-7580.2010.01213.x.
- [45] Luscieti P, Hubschmid T, Cottier H, Hess MW, Sobin LH. Human lymph node morphology as a function of age and site. *J Clin Pathol* 1980;33:454–61.
- [46] Dijkema IM, Hofman P, Raaijmakers CPJ, Lagendijk JJ, Battermann JJ, Hillen B. Loco-regional conformal radiotherapy of the breast: delineation of the regional lymph node clinical target volumes in treatment position. *Radiother Oncol* 2004;71:287–95. doi:10.1016/j.radonc.2004.02.017.

- [47] Raaymakers BW, Lagendijk JJW, Overweg J, Kok JGM, Raaijmakers AJE, Kerkhof EM, et al. Integrating a 1.5 T MRI scanner with a 6 MV accelerator: proof of concept. *Phys Med Biol* 2009;54:N229-37. doi:10.1088/0031-9155/54/12/N01.
- [48] Dempsey J, Dionne B, Fitzsimmons J, Haghigat A, Li J, Low D, et al. WE-E-ValA-06: A Real-Time MRI Guided External Beam Radiotherapy Delivery System. *Med Phys* 2006;33:2254. doi:10.1118/1.2241803.
- [49] Fallone BG, Murray B, Rathee S, Stanescu T, Steciw S, Vidakovic S, et al. First MR images obtained during megavoltage photon irradiation from a prototype integrated linac-MR system. *Med Phys* 2009;36:2084-8.

“Milano, un paesaccio dove per mangiare
un piatto di maccheroni bisogna pensarci
una settimana prima.”

Giuseppe Tomasi di Lampedusa



Supine MRI of individual axillary lymph nodes before and after sentinel-node biopsy

Tristan C. F. van Heijst
Debora Eschbach-Zandbergen*
Nienke Hoekstra*
Bram van Asselen
Jan J. W. Lagendijk
Helena M. Verkooijen
Ruud M. Pijnappel
Stephanie N. de Waard
Arjen J. Witkamp
Thijs van Dalen
H. J. G. Desirée van den Bongard
Marielle E. P. Philippens

Manuscript submitted

**Authors contributed equally*

Abstract

Regional radiotherapy (RT) is increasingly used in breast-cancer treatment. Conventionally, computed tomography (CT) is performed for RT planning. Lymph node (LN) target levels are delineated according to anatomical boundaries. MRI could enable individual LN delineation. The purpose was to evaluate applicability of MRI for LN detection in supine treatment position, before and after sentinel-node biopsy (SNB). 23 female breast-cancer patients (cTis-3N0M0) underwent 1.5 T MRI, before and after SNB, additional to CT. Endurance for MRI was monitored. Axillary levels were delineated. LNs were identified and delineated on MRI from before and after SNB, and on CT, and compared by Wilcoxon signed-rank tests. LN locations and LN-based volumes were related to axillary delineations and associated volumes. Although postoperative effects were visible, LN numbers on postoperative MRI (median 26 LNs) were highly reproducible compared to preoperative MRI when adding excised sentinel nodes, and higher than on CT (median 11, $p < 0.001$). LN-based volumes were considerably smaller than respective axillary levels. Supine MRI of LNs is feasible and reproducible before and after SNB. This may lead to more accurate RT target definition compared to CT. With the MRI techniques described here, initiation of novel MRI-guided RT strategies aiming at individual LNs could be possible.

Introduction

In recent years, regional treatment for breast cancer patients with tumour-positive sentinel nodes (SNs) has changed. Regional radiation therapy (RT), performed after breast-conserving surgery (BCS) or mastectomy, is increasingly used as an alternative for axillary lymph node (LN) dissection [1–3]. In conventional regional breast RT, target volumes are contoured on computed tomography (CT) scans, according to contouring guidelines, including those recently published by European Society for Radiotherapy and Oncology (ESTRO) [4]. These guidelines focus on delineation of axillary vessels based on vessels and muscles, since LN visibility on CT is limited. Furthermore, the location of regional LNs varies largely between patients [5]. Magnetic resonance imaging (MRI) can image individual axillary LNs better [6–12]. Guidance by MRI in regional breast RT planning may therefore enable a redefinition and reduction of target volumes, possibly leading to decreased RT-related toxicity, consisting of arm morbidity, e.g. pain, edema, and shoulder stiffness.

Conventional diagnostic breast MRI is not optimized for RT planning, and is acquired in prone position. We have previously developed dedicated MRI, in healthy volunteers, to image axillary LNs for RT planning in supine treatment position [13]. Both anatomy and posture endurance for undergoing MRI in patients are likely to differ from healthy volunteers [14,15]. The next step is, therefore, to validate MRI for regional RT in breast cancer patients in treatment position.

In standard elective RT, axillary LN levels are irradiated. Using MRI, LNs could potentially be delineated and targeted individually. This makes reproducibility of detecting LNs of utmost importance. Furthermore, LN identification on MRI may be affected by axillary surgery. This is usually limited to sentinel-node biopsy (SNB), which is performed for staging purposes, in combination with breast surgery. The surgical excision of one or more SNs in SNB leads to anatomical alterations, due to inflammation and seroma formation [16]. Moreover, patient posture endurance for undergoing MRI may be affected by surgery.

The purpose of this work is to test the reproducibility of LN detection using MRI, and posture endurance, in breast cancer patients who undergo

SNB, pre- and postoperatively, in supine position. Furthermore, locations and volumes of all LNs, including SNs excised during SNB, are related to standard delineation of axillary levels. LN detection rates of MRI are compared to standard postoperative CT.

Materials and Methods

Patients

The Internal Review Board of University Medical Center (UMC) Utrecht approved the *MRI of regional lymph nodes in cT1-3N0 breast cancer and cTisN0 DCIS patients (MILANO)* study, which is registered under Netherlands trial number NL50046.041.14. Written informed consent was obtained from 23 female patients (table 1), who were diagnosed with either ductal carcinoma *in situ* (DCIS), or early-stage breast cancer without pathologically involved LNs or distant metastasis (cTis-T3N0M0). They were scheduled for SNB, performed during BCS or mastectomy, at UMC Utrecht or at Diaconessenhuis Hospital, in Utrecht, The Netherlands. No surgery or RT had been performed previously in the ipsilateral axilla. One patient underwent mastectomy, while 22 participants underwent BCS, 21 of whom received subsequent standard RT treatment at UMC Utrecht.

MRI set-up

Scanning was performed on a 1.5 T wide-bore MRI scanner (Philips Ingenia, The Netherlands) at the RT Department of UMC Utrecht, from February 2015 until February 2016. Participants were scanned in supine RT position [13], i.e. with arms in abduction, supported by a wedge-board (Thorawedge, CIVCO Medical Solutions, The Netherlands). An anterior receive coil was connected and placed on an adjustable polymethyl-metacrylate support, such that the outer anatomy was not deformed. Furthermore, a posterior receive coil was located in the scanner table.

● *Table 1 Patient characteristics for the 23 participants included in our MILANO study.*

<i>Variable</i>		<i>n = 23</i>
<i>Age (years)</i>	Range	40 - 80
	Median	58
<i>BMI (kg/m²)</i>	Range	18.3 - 34.5
	Median	24.0
<i>Affected breast</i>		
	Left	11 (48%)
	Right	12 (52%)
<i>Tumour stage</i>		
<i>Clinical</i>	cTis	3 (13%)
	cT1	18 (78%)
	cT2	2 (9%)
<i>Pathological</i>	pTis	3 (13%)
	pT1	17 (74%)
	pT2	3 (13%)
<i>Nodal stage</i>		
<i>Clinical</i>	N0	23 (100%)
<i>Pathological</i>	N0(sn)	21 (91%)
	N1(sn)	2 (9%)

BMI = body-mass-index; sn = sentinel node.

MRI and CT scanning

Participants underwent two MRI scan sessions. The first was performed a median 7 days (range: 1–23 days) before surgery, whereas the second took place a median 20 days (range: 8–45 days) after surgery. Five MRI scans were acquired on both occasions, which were optimized previously in healthy volunteers [13]. Relevant imaging parameters are listed in table 2.

The first method was a T1-weighted (T1w) spoiled gradient echo (SPGR) technique, acquired transversally. The in-plane field-of-view (FOV) encompassed the outer body contour, ranging in cranial-caudal direction from the mandible to the caudal border of the breast. Here, multi-point Dixon (mDixon) water-fat separation was applied, where two echoes are used to separate signal from fat and water [17]. The other four MRI scans were acquired in the coronal plane, with FOVs covering the axillary areas. One MRI technique was a T1w SPGR sequence using mDixon, with smaller FOV than the first T1w SPGR, but in higher resolution. Furthermore, both a two-dimensional (2D) and 3D T2w fast spin echo technique were applied. The final scan was a diffusion-weighted MRI (DWI), in which restriction of water mobility is reflected by hyper-intense signal. No contrast agent was administered.

Twenty-one patients underwent postoperative CT imaging for standard RT planning in supine RT position, on a support (CIVCO, The Netherlands). This was usually performed on the same day as postoperative MRI. Acquisition duration was 20 s, slice thickness 3 mm, and minimal in-plane resolution was $1 \times 1 \text{ mm}^2$ (Brilliance, Philips). The FOV of the RT-planning CT included the breast and axillary areas.

● Table 2 Imaging parameters of the MRI sequences used for LN imaging in our MILANO study. The 3D scans were reconstructed using overcontiguous slices.

Sequences	T1-TFE (reference)	T2-TSE	T2-VISTA	DWI	T1-FFE
Imaging parameters					
Type of sequence	TFE	TSE	TSE	EPI	FFE
Weighting	T1	T2	T2	Diffusion	T1
Fat suppression/separation	mDixon	mDixon	SPAIR	STIR	mDixon
Dimensionality	3D	2D	3D	2D	3D
Acquisition plane	transverse	coronal	coronal	coronal	coronal
Acquired resolution	1.50 x 1.50 x 2.00 mm ³	0.75 x 0.76 mm ²	0.99 x 1.00 x 2.00 mm ³	2.98 x 3.03 mm ²	0.99 x 1.00 x 2.20 mm ³
Reconstructed resolution	0.78 x 0.78 x 1.00 mm ³	0.59 x 0.59 mm ²	0.60 x 0.60 x 1.00 mm ³	1.04 x 1.05 mm ²	0.76 x 0.76 x 1.10 mm ³
Slice thickness (mm)	-	3.00	-	3.00	-
TR/TE (ms)	5.6 / 2.0 / 3.8 *	4134 / 80	1600 / 157	4787 / 78	5.8 / 2.2 / 4.0 *
Preparation/pre-pulse	-	-	$v_{enc} = 1.0$ cm/s (CC/RL)	-	-
Diffusion b values (s/mm ²)	-	-	-	0, 400, 800	-
FOV (mm ²)	300 x 450 x 300	250 x 450 x 100	250 x 450 x 100	250 x 450 x 100	250 x 425 x 100
Acquisition time (m:ss)	4:00	4:53	3:14	3:06	3:10

TFE = turbo field echo; TSE = turbo spin echo; VISTA = volumetric isotropic T2w acquisition; DWI = diffusion-weighted imaging; FFE = fast field echo; mDixon = multi-point Dixon; SPAIR = spectral attenuated inversion recovery; STIR = short T1 inversion recovery; 3D = 3-dimensional; TR = repetition time; TE = echo time; v_{enc} = velocity encoding; CC = caudal-cranial; RL = right-left; FOV = field-of-view.

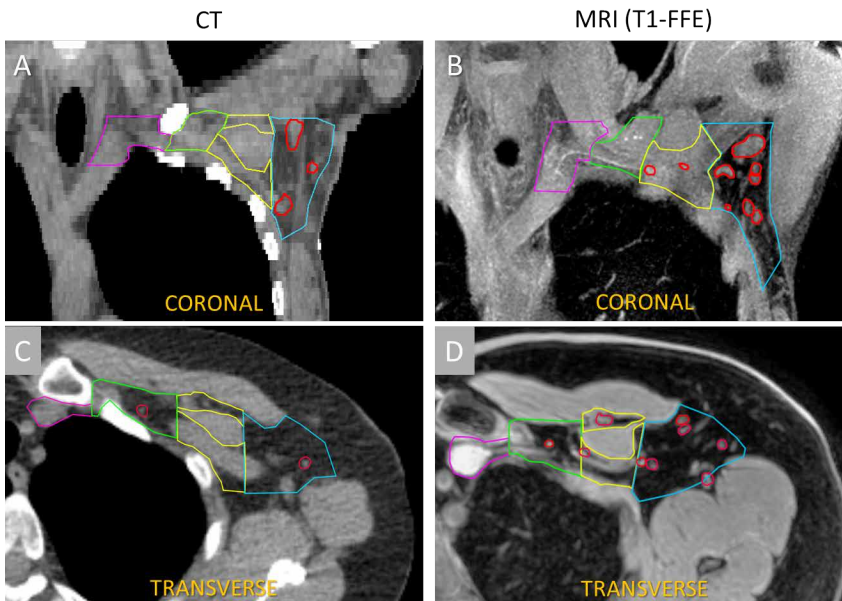
*TR/TE1/TE2.

Posture endurance for MRI

Acquisition time of MRI was limited to 20 minutes per session. Due to extra time for positioning and scanner preparation, the supine RT position had to be maintained up to 30 min each session. Since this is potentially difficult to endure, we monitored whether the patient was able to finish the procedure. If applicable, the reason of insufficient posture endurance was captured, as was the need for adjustments in positioning.

Contouring of axillary levels on MRI

The first T1w scan, with the largest FOV, was considered as reference scan, to which other scans of the same MRI session were co-registered. For MRI methods using mDixon, water-only (Dixon-water) and fat-only (Dixon-fat) images were both examined. A breast radiation oncologist contoured standard regional target volumes on preoperative scans (figure 1), according to ESTRO delineation guidelines [4]. These were developed for



● *Figure 1 Examples of delineations performed on CT and MRI. CT is shown on the left, while the Dixon-water image of the T1-FFE MRI scan is shown on the right. Standard axillary levels I-IV, contoured according to ESTRO guidelines, are depicted in lateral-medial order (in blue: level I, yellow: level II, green: level III, purple: level IV). Individual LNs are also contoured (red).*

CT, but are also applicable for use on MRI. For MRI, minor adaptations were implemented due to soft-tissue differences. We will refer to axillary target contours, defined as levels I-IV, as axillary levels. The interpectoral level was incorporated in level II.

Lymph node identification and delineation

Using information from all scans in one MRI session, individual LNs were identified, and delineated on the reference scan (figure 1). LN identification was first performed by two observers independently, who were trained for this by a breast radiologist. Identification on MRI and CT was validated by two other observers, including a breast radiation oncologist and a breast radiologist. After multidisciplinary meetings with all observers, consensus was reached on pre- and postoperative sets of LNs, on MRI and CT.

The number of LNs was determined for each patient in scans from both MRI sessions. Moreover, it was determined in which axillary level a LN was located on preoperative MRI. If a LN was partly located in an axillary level, it was considered to be included in that contour. If a LN was located in more than one level, the level was chosen in which it occupied the most volume. Finally, LNs outside the axillary level contours, but within 5 mm, were counted separately. LNs at more than 5-mm distance were excluded. Pre- and postoperative sets of delineated LNs in each patient were compared on a node-to-node basis. If possible, spatial correlation was established between individual LNs on both MRI sessions.

Furthermore, if possible, the excised SNs were retrospectively identified on preoperative MRI. This was performed visually, by comparing surrounding LNs and studying anatomical changes. Moreover, the number of excised SNs was taken from the pathology report and compared to difference in number of LNs before and after SNB. During SNB, SNs excised can also be internal mammary LNs. However, for our analysis we only consider axillary SNs.

LN detection rate is defined by the number of identified LNs. These were compared per patient, on MRI before and after SNB, while also accounting for the excised SN(s). The postoperative LN detection rate on CT was compared to the postoperative MRI detection rate.

Statistical analysis

Statistical analysis was performed using *R* software [18]. Normality was checked by visual inspection of calculated Q-Q plots. To assess reproducibility, LN detection rate on pre-SNB MRI was compared with the LN detection rate on post-SNB MRI using paired Wilcoxon signed-rank tests. Similarly, the LN detection rate of post-SNB MRI was compared to post-SNB CT. Furthermore, Bland-Altman plots were calculated which represent the difference between the LN detection rates as a function of the average of the two measurements.

Volumes of lymph nodes and axillary levels

On MRI, the summed volumes of all delineated LNs were determined, in order to indicate potential reduction in target volume based on individual LNs. These LN-based volumes were compared to volumes of the respective axillary levels. The effect of expanding the LN delineations was also explored by making an isotropic expansion of 5 mm and performing a similar comparison of the resulting encompassing volumes, compared to the axillary levels.

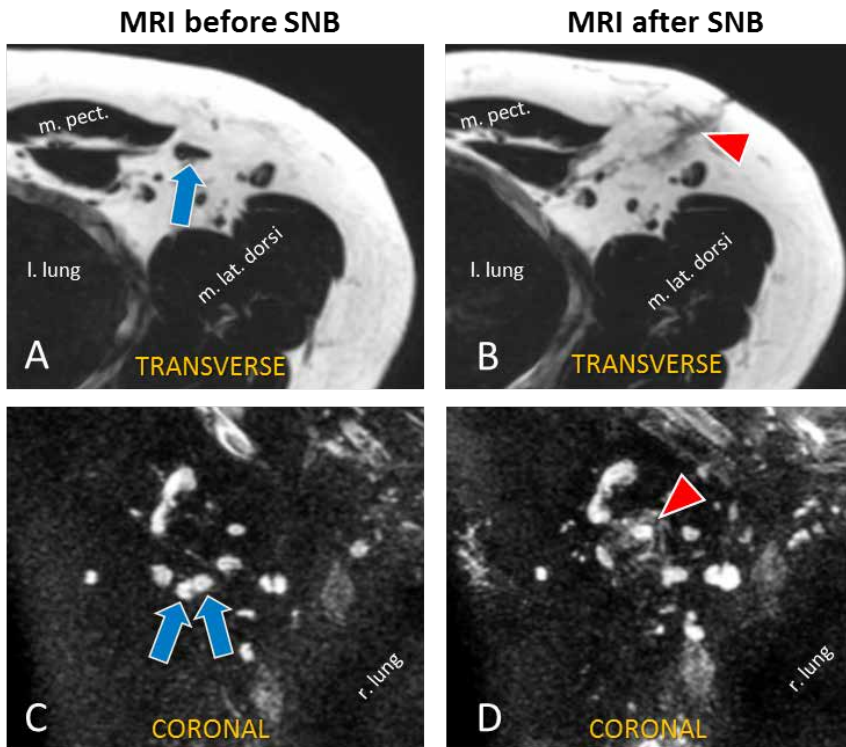
Results

Posture endurance for MRI

Twenty out of 23 patients finished both scan sessions without posture adjustments. One patient experienced pain in her shoulders on both occasions during pre- and postoperative MRI. As she was unable to finish the scanning sessions, not all scans were acquired. Another patient experienced pain in the ipsilateral shoulder, preoperatively, due to a pre-existing cervical hernia. A third patient had a painful contralateral shoulder during postoperative MRI. Patient positioning was adjusted for both patients after acquisition of three scans, by lowering the ipsilateral or contralateral arm. The remaining scans were acquired without problems.

Use of MRI in practice

LNs were visualized in all patients (figure 2). Fat separation by mDixon was excellent. For LN identification, all acquired MRI scans could be used. In practice not all scans were always contributive. Most LNs were first identified on the T1w SPGR reference scan. The T2w TSE scans were consulted to confirm this, and to identify additional LNs, usually close to blood vessels and arteries, due to lack of contrast on T1w images in those locations. A drawback was that image quality of the T2w scans was lower in patients with higher BMI. The other T1w method showed similar



● *Figure 2 Axillary LNs visualized with MRI before and after SNB. MR images from before SNB (left, A, C) and after SNB (right, B, D), in two patients (each row) are depicted. The first row shows Dixon-fat images of a transverse T1-FFE (A,B) where the arrow points to the SN (i.e. absence of fat signal in the SN); the right arrowhead points to postoperative anatomical changes, e.g. presence of seroma. The second example (C,D) is a T2-TSE coronal scan. “The arrows and arrowhead similarly show two SNs and postoperative seroma, respectively. SNB = sentinel-node biopsy; m. pect = musculus pectoralis; r. lung = right lung; m. lat. dorsi = latissimus dorsi muscle; l. lung = left lung; T1-FFE = T1-weighted fast field echo; T2-TSE = T2-weighted turbo spin echo.*

contrast as the reference scan and therefore served as confirmation for LN identification. The added value of DWI was limited due to low resolution.

Postoperative artifacts

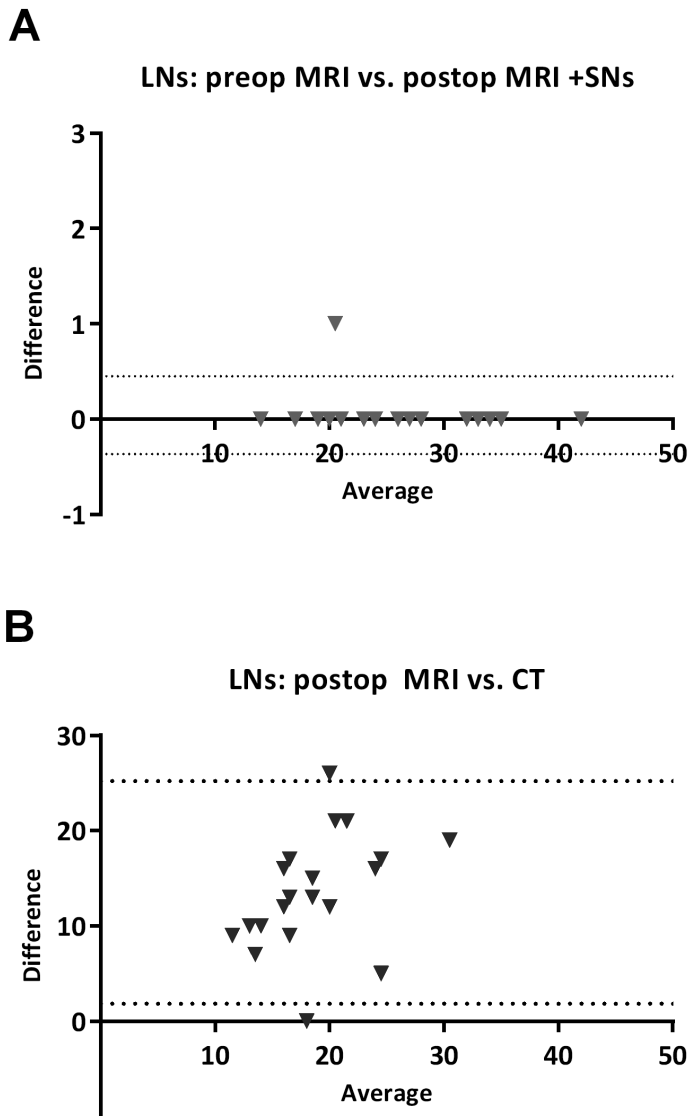
In all patients, postoperative effects were recognizable on MRI. Enlargement of LNs was observed after SNB in some patients. Repositioning of arteries, muscles and LNs was observed in all patients. Spatial differences related to this were usually small. Formation of postoperative seroma was also visible in all patients, which appeared diluted in all but two patients. The presence of post-SNB effects served as landmarks for retrospectively localizing SNs on preoperative MRI that were excised during SNB (figure 2).

MRI: detection rates, correlation, and sentinel nodes

The median number of LNs was 26 (range: 14–42) on preoperative MRI, while this was 25 (range: 13–40) on postoperative MRI (table 3). In total, 617 and 587 LNs were identified, on MRI, pre- and post-SNB, respectively. The median number of SNs excised during SNB was 1 (range: 1–3), with a total of 33. For 22 out of 23 patients, preoperative LN detection rate was equal to postoperative detection rate on MRI, when the SNs were added ($p = 1.00$) (table 3, figure 3). In one patient, 20 LNs were identified before and 17 after SNB, while 2 SNs had been removed.

In 20 out of the remaining 22 patients, all 550 individual LNs could be spatially correlated between MRI sessions. Any anatomical variation due to a different scanning position did not affect LN correlation in general. In the two other patients, a large postoperative seroma, as well as shifted muscles and arteries, disrupted the anatomy, thereby hampering an exact correlation. However, pre- and postoperative MRI detection rates were equal.

All SNs were identified retrospectively on preoperative MRI. For all patients, numbers of identified SNs matched numbers of excised SNs described in pathology reports (table 3).



● Figure 3 Bland-Altman plots of LN detection rates. Plots are shown for (A) preoperative MRI and postoperative MRI plus number of excised SNs ($n = 23$); (B) postoperative MRI and CT ($n = 21$). These indicate the difference of the two detection rates, as a function of the average of the two measurements. The 95% confidence intervals are indicated by dotted lines.

● *Table 3 LN detection rates and numbers of excised SNs. Per individual patient, LN detection rates on MRI and CT are listed. Furthermore, the number of excised SNs is listed, together with PA value in brackets, denoted as ‘number of SNs, PA result’. A value of ‘-’ reflects a tumour-negative SN, while ‘+’ is a tumour-positive SN. Only in patient 12 does ‘ Δ LN on MRI’ not coincide with the number of axillary SNs from the histopathology reports.*

<i>Patient number</i>	<i>Preop MRI</i>	<i>Postop MRI</i>	<i>Postop CT</i>	<i>ΔLN on MRI</i>	<i>SNs excised (number, +/-)</i>
1	28	27	22	1	1 (1,-)
2	42	40	21	2	2 (2,-)
3	35	33	16	2	2 (2,-)
4	24	23	10	1	1 (1,-)
5	34	33	7	1	2 (2,-)*
6	33	32	11	1	1 (1,+; macro)
7	19	18	8	1	1 (1,-)
8	23	22	10	1	1 (1,-)
9	21	18	18	3	3 (3,-)
10	28	26	14	2	2 (2,-)
11	23	21	12	2	2 (2,+; isolated cells)
12	20	17	10	3	2 (2,-)
13	33	32	16	1	1 (1,-)
14	26	24	8	2	3 (3,-)*
15	26	25	12	1	1 (1,-)
16	17	16	7	1	1 (1,-)
17	20	19	9	1	1 (1,-)
18	26	25	8	1	1 (1,-)
19	14	13	NA	1	1 (1,-)
20	32	31	10	1	1 (1,-)
21	27	26	11	1	1 (1,-)
22	33	32	16	1	1 (1,-)
23	33	32	NA	1	1 (1,-)

LN = lymph node; preop = preoperative; MRI = magnetic resonance imaging; postop = postoperative; CT = computed tomography; Δ LN = difference in numbers of lymph nodes; SN = sentinel node; PA = pathology; NA = not applicable (since no CT was performed for those patients).

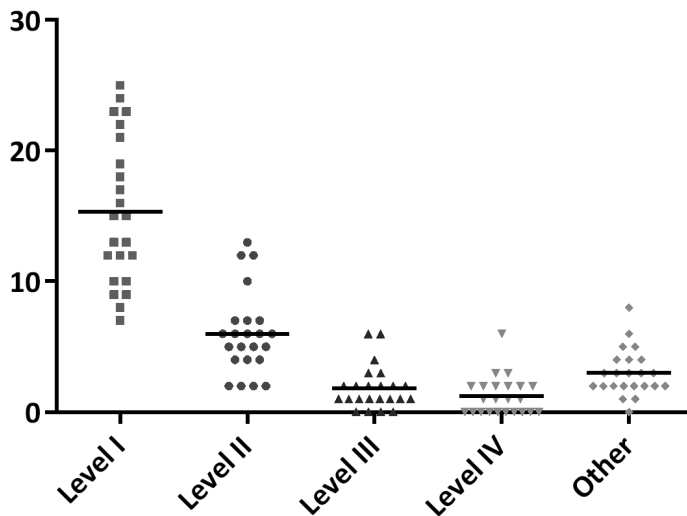
**In patients 5 and 14, one SN was an internal mammary LN; it was therefore not counted on preoperative MRI in our analysis.*

Detection rate on postoperative CT

In total, 255 LNs were identified on all 21 postoperative CT scans. The median number of LNs was 11 (range: 7–22) per patient. LN detection rate on CT was significantly lower than on postoperative MRI ($p < 0.0001$) (table 3, figure 3).

Relative location of lymph nodes to axillary levels

The majority (353, 57%) of all 617 identified LNs were located in axillary level I (median per patient: 15, range: 13–28) (figure 4). Particularly, all 33 identified SNs were identified in level I. More cranially located axillary levels gradually contained fewer LNs. A total of 138 (median per patient 6, range: 4–12) LNs were in level II. Only one patient showed more LNs in level II than in level I. Summed over all patients, levels III and IV contained only 42 and 28 LNs (7% and 5%), at a median of 1 LN per patient (ranges: 0–4 and 0–3, respectively). Moreover, 69 LNs (11%) were counted outside the axillary levels, at a median of 2 per patient (range: 0–8). Most of these LNs (49 of 69, 71%) were located nearest to level I.



● Figure 4 Number of LNs as determined on preoperative MRI for all 23 patients per axillary level. Axillary contours indicated are level I (squares), level II (circles), level III, (triangles pointing up), and level IV (triangles pointing down). LNs located outside the axillary levels but within 5 mm distance from the contours are depicted as 'other' (diamonds). Medians are indicated by the horizontal lines.

Lymph node-based volumes

The summed volume of LNs in level I was the largest, in all patients (table 4). Median LN-based volumes were at most 3% of the volumes of the respective axillary levels. After 5-mm expansion, encompassing volumes of individual LN delineations was limited to at most 46% of the corresponding axillary level. The median encompassing volume of LNs counted outside axillary levels on MRI was 5.0 cc after expansion.

● *Table 4 LN-based target volumes, without and with expansion, per respective axillary level. Volumes based on individual LNs as delineated on MRI are calculated both without expansion (summed volume), and with a 5-mm expansion (encompassing volume). Volumes of respective axillary levels (I-IV) are given, delineated on MRI according to modified ESTRO delineation guidelines [4]. LNs counted outside of the levels are indicated as ‘other’. Values are denoted ‘median (range)’. Values < 0.05 cc were rounded up to 0.1 cc.*

	Summed volume (cc)	Encompassing volume (cc)	Volume (cc)
Location	Individual LNs	Individual LNs (+5 mm)	Axillary levels
Level I	2.2 (0.9 – 8.0)	32.8 (16.2 – 52.5)	71.9 (23.4 – 162.4)
Level II	0.4 (0.1 – 0.8)	10.0 (2.9 – 20.4)	32.0 (17.6 – 61.7)
Level III	0.1 (0.1 – 0.3)	3.0 (1.1 – 10.3)	17.6 (8.8 – 30.3)
Level IV	0.1 (0.1 – 0.4)	3.7 (1.4 – 7.9)	15.4 (11.2 – 20.7)
Other	0.1 (0.1 – 0.9)	5.0 (1.7 – 16.2)	-
Total	3.2 (1.2 – 9.7)	47.9 (26.7 – 81.1)	132.8 (69.4 – 239.8)

LN = lymph node.

Discussion

MRI of axillary LNs, in supine RT position, is feasible, before and after SNB. Although diagnostic MRI for axillary imaging is thoroughly studied [6–12], MRI studies for target delineation in regional breast RT are scarce.

SNB did not affect patient posture endurance for MRI in supine position. LN detection on MRI scans before and after SNB was highly reproducible, despite postoperative artifacts observed in all patients. All SNs that were excised during SNB were retrospectively identified. Moreover, in 20 patients, all other LNs could be individually correlated between MRI sessions. Compared to MRI, LN detection rate on CT was significantly lower.

There is no gold standard for the number of LNs. Numbers in our study, ranging from 14–42 on MRI, fall in the expected range of 6–45 LNs, based on previous imaging (MRI, CT, and ultrasonography) and histological studies on LNs [19–24]. Histological information, after axillary dissection, is limited to axillary levels I and II, while our work aimed to image LNs in axillary levels I–IV. The range is also similar to that in healthy volunteers [13]. Most LNs (57%) were located in level I, being the largest axillary volume, including all identified SNs. Two SNs were tumour-positive, but these were not obviously enlarged on MRI. We did not perform a diagnostic analysis on MRI for the SNs. More cranially located levels gradually contained fewer LNs. Numbers of LNs detected in levels III and IV were within the expected range of 1–10 LNs [25]. However, the supraclavicular region was difficult to image, due to signal from large blood vessels that was not always adequately suppressed in T2w scans, and which could obscure other structures in T1w images. This could have impaired localization of small LNs.

LN detection rate on MRI was significantly higher than on CT, mainly due to its superior soft-tissue contrast. It should be noted that CT was acquired for standard RT target delineation and was not optimized for LN identification.

There are limitations in the set-up of our study. Consensus was reached on LN identification with the expertise of a multidisciplinary team of

observers. This did not allow determination of inter-observer variation, as LN identification was performed in consensus, and in a relatively limited number of patients. Most discussion was on LNs that were located close to blood vessels, the signal of which was not suppressed adequately. This might have led to false-positives and false-negatives. The current work focused on reproducibility of LN detection before and after SNB, where information from preoperative scans was used in the postoperative scans, and vice versa. An inter-observer delineation study will be conducted in the future to assess potential bias introduced this way.

Using ESTRO guidelines [4] on MRI, up to 8 LNs per patient were located outside the axillary level delineations (but within 5-mm distance), commonly cranial to levels III/IV or dorsolateral to level I. MacDonald *et al.* [20] also found LNs outside axillary levels. The question is whether these LNs should be irradiated. An approach to cover these in the target is to extend the axillary contours, leading to more treated normal tissue. Addition of MRI information to standard CT-based RT planning could lead to redefinition of standard target volumes, by localizing individual LNs. Therefore, we explored individual LN target delineations and calculated LN-based volumes. Even with a 5-mm expansion for each LN delineation, encompassing volumes are considerably smaller than the respective axillary levels, which are delineated based on vessels and musculature. Consequently, for elective CT-based RT strategies, adding information from dedicated MRI scans could lead to smaller treated volumes, while still effectively covering the individual LNs. This could be enabled by co-registration of MRI with the RT-planning CT scan. However, this procedure is prone to set-up variations. Furthermore, nowadays, RT of LNs is performed after axillary surgery. Since the presence of postoperative artifacts could obscure LNs, new approaches may focus on preoperative RT instead.

On-line MRI guidance could open further possibilities of treatment of individual LNs, as achieved by the UMC Utrecht MRI/linear accelerator and other MRI/RT modalities [26–29]. Using these hybrid modalities, delivery of a stereotactic high dose to tumour-positive LNs may be possible. For such advanced stereotactic RT techniques, the use of additional methods for identifying metastatic LNs on MRI is necessary [11]. Such novel approaches may lead to lower RT-related toxicity, shorter

RT treatment schedules, or omission of surgery for selected breast-cancer patients. Feasibility of MRI-guided RT, specifically targeting individual LNs, is currently under investigation at UMC Utrecht.

Conclusions

MRI of LNs in supine RT position in breast cancer patients is feasible. LN detection rate on MRI is reproducible before and after SNB. Implementation of MRI in RT planning may lead to more accurate target definition, compared to CT-based regional RT planning. LN-based delineation using MRI may result in a reduction in standard regional RT target volumes. Furthermore, this may enable new regional RT approaches in breast-cancer patients targeting individual LNs.

References

- [1] Donker M, van Tienhoven G, Straver ME, Meijnen P, van de Velde CJH, Mansel RE, et al. Radiotherapy or surgery of the axilla after a positive sentinel node in breast cancer (EORTC 10981-22023 AMAROS): a randomised, multicentre, open-label, phase 3 non-inferiority trial. *Lancet Oncol* 2014;15:1303–10. doi:10.1016/S1470-2045(14)70460-7.
- [2] Galimberti V, Cole BF, Zurrada S, Viale G, Luini A, Veronesi P, et al. Axillary dissection versus no axillary dissection in patients with sentinel-node micrometastases (IBCSG 23-01): a phase 3 randomised controlled trial. *Lancet Oncol* 2013;14:297–305. doi:10.1016/S1470-2045(13)70035-4.
- [3] Giuliano AE, McCall L, Beitsch P, Whitworth PW, Blumencranz P, Leitch AM, et al. Locoregional recurrence after sentinel lymph node dissection with or without axillary dissection in patients with sentinel lymph node metastases: the American College of Surgeons Oncology Group Z0011 randomized trial. *Ann Surg* 2010;252:426–32; discussion 432–3. doi:10.1097/SLA.0b013e3181f08f32.
- [4] Offersen B V, Boersma LJ, Kirkove C, Hol S, Aznar MC, Biete Sola A, et al. ESTRO consensus guideline on target volume delineation for elective radiation therapy of early stage breast cancer. *Radiother Oncol* 2015;114:3–10. doi:10.1016/j.radonc.2014.11.030.
- [5] Dijkema IM, Hofman P, Raaijmakers CPJ, Lagendijk JJ, Battermann JJ, Hillen B. Loco-regional conformal radiotherapy of the breast: delineation of the regional lymph node clinical target volumes in treatment position. *Radiother Oncol* 2004;71:287–95. doi:10.1016/j.radonc.2004.02.017.
- [6] Kuijjs VJL, Moosdorff M, Schipper RJ, Beets-Tan RGH, Heuts EM, Keymeulen KBMI, et al. The role of MRI in axillary lymph node imaging in breast cancer patients: a systematic review. *Insights Imaging* 2015;6:203–15. doi:10.1007/s13244-015-0404-2.
- [7] Lernevall A. Imaging of Axillary Lymph Nodes. *Acta Oncol (Madr)* 2000;39:277–81. doi:10.1080/028418600750013014.
- [8] Rahbar H, Partridge SC, Javid SH, Lehman CD. Imaging axillary lymph nodes in patients with newly diagnosed breast cancer. *Curr Probl Diagn Radiol* 2012;41:149–58. doi:10.1067/j.cpradiol.2011.08.002.
- [9] Li C, Meng S, Yang X, Wang J, Hu J. The value of T2* in differentiating metastatic from benign axillary lymph nodes in patients with breast cancer—a preliminary in vivo study. *PLoS One* 2014;9:e84038. doi:10.1371/journal.pone.0084038.
- [10] Menezes GL, Knuttel FM, Stehouwer BL, Pijnappel RM, van den Bosch MA. Magnetic resonance imaging in breast cancer: A literature review and future perspectives. *World J Clin Oncol* 2014;5:61–70. doi:10.5306/wjco.v5.i2.61.
- [11] Harnan SE, Cooper KL, Meng Y, Ward SE, Fitzgerald P, Papaioannou D, et al. Magnetic resonance for assessment of axillary lymph node status in early breast cancer: A systematic review and meta-analysis. *Eur J Surg Oncol* 2011;37:928–36.
- [12] Ahmed M, Usiskin SI, Hall-Craggs MA, Douek M. Is imaging the future of axillary staging in breast cancer? *Eur Radiol* 2014;24:288–93. doi:10.1007/s00330-013-3009-5.
- [13] van Heijst TCF, van Asselen B, Pijnappel RM, Cloos-van Balen M, Lagendijk JJW, van den Bongard HJGD, et al. MRI sequences for the detection of individual lymph nodes in regional breast radiotherapy planning. *Br J Radiol* 2016;20160072. doi:10.1259/bjr.20160072.
- [14] Hadamitzky C, Spohr H, Debertin AS, Guddat S, Tsokos M, Pabst R. Age-dependent histoarchitectural changes in human lymph nodes: an underestimated process with clinical relevance? *J Anat* 2010;216:556–62. doi:10.1111/j.1469-7580.2010.01213.x.

- [15] Luscieti P, Hubschmid T, Cottier H, Hess MW, Sobin LH. Human lymph node morphology as a function of age and site. *J Clin Pathol* 1980;33:454–61.
- [16] Srivastava V, Basu S, Shukla VK. Seroma formation after breast cancer surgery: what we have learned in the last two decades. *J Breast Cancer* 2012;15:373–80. doi:10.4048/jbc.2012.15.4.373.
- [17] Eggers H, Brendel B, Duijndam A, Herigault G. Dual-echo Dixon imaging with flexible choice of echo times. *Magn Reson Med* 2011;65:96–107. doi:10.1002/mrm.22578.
- [18] R Core Team. R: A Language and Environment for Statistical Computing. R Found Stat Comput Vienna Austria 2014;0:[ISBN] 3–900051 – 07–0.
- [19] Luciani A, Pigneur F, Ghozali F, Dao T-H, Cunin P, Meyblum E, et al. Ex vivo MRI of axillary lymph nodes in breast cancer. *Eur J Radiol* 2009;69:59–66. doi:10.1016/j.ejrad.2008.07.040.
- [20] MacDonald SM, Harisinghani MG, Katkar A, Napolitano B, Wolfgang J, Taghian AG. Nanoparticle-enhanced MRI to evaluate radiation delivery to the regional lymphatics for patients with breast cancer. *Int J Radiat Oncol Biol Phys* 2010;77:1098–104. doi:10.1016/j.ijrobp.2009.06.002.
- [21] Korteweg MA, Zwanenburg JJM, Hoogduin JM, van den Bosch MAAJ, van Diest PJ, van Hillegerberg R, et al. Dissected sentinel lymph nodes of breast cancer patients: characterization with high-spatial-resolution 7-T MR imaging. *Radiology* 2011;261:127–35. doi:10.1148/radiol.11103535.
- [22] Jiang J, He Q, Yang X, Liang Y, Fan L, Zhang Y, et al. Contribution of minute axillary lymph nodes to accurate staging for patients with breast cancer. *Chin Med J (Engl)* 2007;120:1762–5.
- [23] Nakai G, Matsuki M, Harada T, Tanigawa N, Yamada T, Barentsz J, et al. Evaluation of axillary lymph nodes by diffusion-weighted MRI using ultrasmall superparamagnetic iron oxide in patients with breast cancer: initial clinical experience. *J Magn Reson Imaging* 2011;34:557–62. doi:10.1002/jmri.22651.
- [24] Hong Y, Xiang L, Hu Y, Zhou Z, Yu H, Zhu B. Interstitial magnetic resonance lymphography is an effective diagnostic tool for the detection of lymph node metastases in patients with cervical cancer. *BMC Cancer* 2012;12:360. doi:10.1186/1471-2407-12-360.
- [25] Ying M, Ahuja A. Sonography of Neck Lymph Nodes. Part I: Normal Lymph Nodes. *Clin Radiol* 2003;58:351–8. doi:10.1016/S0009-9260(02)00584-6.
- [26] Raaymakers BW, Legendijk JJW, Overweg J, Kok JGM, Raaijmakers AJE, Kerkhof EM, et al. Integrating a 1.5 T MRI scanner with a 6 MV accelerator: proof of concept. *Phys Med Biol* 2009;54:N229–37. doi:10.1088/0031-9155/54/12/N01.
- [27] Dempsey J, Dionne B, Fitzsimmons J, Haghigat A, Li J, Low D, et al. WE-E-ValA-06: A Real-Time MRI Guided External Beam Radiotherapy Delivery System. *Med Phys* 2006;33:2254. doi:10.1118/1.2241803.
- [28] Fallone BG, Murray B, Rathee S, Stanescu T, Steciw S, Vidakovic S, et al. First MR images obtained during megavoltage photon irradiation from a prototype integrated linac-MR system. *Med Phys* 2009;36:2084–8.
- [29] Legendijk JJW, Raaymakers BW, Raaijmakers AJE, Overweg J, Brown KJ, Kerkhof EM, et al. MRI/linac integration. *Radiother Oncol* 2008;86:25–9. doi:10.1016/j.radonc.2007.10.034.

“See it? Zap it!”

Jean-Philippe Pignol



MRI-guided single-fraction boost delivery on individual axillary lymph nodes

Tristan C. F. van Heijst
Nienke Hoekstra
Marielle E. P. Philippens
Debora Eschbach-Zandbergen
Jan J. W. Lagendijk
H. J. G. Desirée van den Bongard
Bram van Asselen

Manuscript submitted

Abstract

In standard regional radiotherapy (RT) for breast cancer patients, target volumes are contoured on computed tomography scans (CT) based on anatomical boundaries, since lymph node (LN) visualization of CT is limited. Magnetic resonance imaging (MRI) offers direct delineation of individual LNs. MRI/RT modalities, including the Utrecht MRI linear accelerator (MRL), make new regional RT strategies for breast cancer patients possible. The aim of this study was to explore the concept of a single-fraction high dose (boost) to a single LN in the MRL, additional to elective loco-regional RT. Five early-stage cN0 patients were scanned with MRI in supine position. Standard axillary levels and organs-at-risk (OARs), including brachial plexus, neurovascular bundle (NVB) and chest wall, were delineated. Per patient, four LNs were delineated with 2-mm PTV margin, throughout the axillary levels. Pseudo-CT (pCT) scans were generated by bulk assignment. Elective loco-regional RT, consisting of 16 x 2.66 Gy to the whole breast and axillary levels, was planned on pCT scans using Monaco software. Single-fraction RT of 9 Gy, 11 Gy, and 13 Gy (ablative dose), with dose escalation within the PTV, were simulated for each selected LN, using MRL treatment planning software. Addition of dose plans was performed voxel-by-voxel, after conversion of both dose plans into EQD₂, to obtain total dose plans. Clinical constraints were evaluated on total dose, and extra dose to OARs and unspecified tissue was calculated on boost plans. Target coverage was excellent, while additional dose to OARs was limited or negligible. Dose parameters were all within clinical constraints. Concluding, additional LN boosting is feasible up to ablative dose levels, regardless of LN location. This enables possibilities for MRI-guided RT of individual LNs. In selected breast cancer patients, this may lead to omission of axillary surgery, or reduction of conventional fractionated RT schedules, and possibly reduction of treatment-induced toxicity.

Introduction

The introduction of novel hybrid modalities enables on-line magnetic resonance imaging (MRI) guidance for delivery of external beam radiation therapy (RT) [1–4]. One such design is the MRI/linear accelerator (MRL), developed at University Medical Center (UMC) Utrecht, The Netherlands, which combines a 1.5 T MRI scanner (Philips, Best, Netherlands) and a fully integrated 7 MV photon linear accelerator (linac) (AB Elekta, Stockholm, Sweden). Since MRI has superior soft-tissue contrast over conventional imaging modalities, this allows for accurate target definition and precise RT delivery.

Breast cancer patients could benefit from MRI guidance in the MRL. Elective axillary RT (AxRT) is increasingly performed in patients with a limited number of tumour-positive sentinel nodes (SNs) [5,6]. AxRT is usually delivered in conventional or hypo-fractionated schedules, often combined with whole-breast irradiation (WBI) after breast-conserving surgery (BCS), or chest-wall RT after mastectomy [7,8]. Patients with clinically tumour-positive lymph nodes (cN+) before primary surgery or after primary systemic therapy can be treated by axillary lymph node dissection (ALND) and/or AxRT. Furthermore, in case of irresectable lymph node (LN) metastasis in the periclavicular region, a conventionally fractionated RT boost dose of 10-20 Gy can be currently delivered, sequentially to elective AxRT. Both sequential axillary RT (with/without boost on involved LNs) and ALND are associated with high morbidity [9,10]. Imaging of individual LNs could enable new image-guided RT treatments with decreased risk of treatment-induced arm morbidity.

Target delineation in AxRT planning is performed on computed tomography (CT) scans, based on guidelines that focus on anatomical boundaries [11–14]. However, LN visualization of CT is limited. As a consequence, AxRT target volumes are relatively large. In contrast, MRI can visualize individual regional LNs [15]. We showed that individual LN delineation with MRI is feasible and highly reproducible in breast cancer patients, and that LN-based volumes on MRI are considerably smaller than standard AxRT target volumes (described in chapter 5). Moreover, MRI can visualize organs-at-risk (OARs) that can be located close to LNs, including the brachial plexus, chest wall, shoulder joint, and lungs

[16–18]. High dose to those structures can induce brachial plexopathy, rib pain, reduced arm mobility and/or pain, and radiation pneumonitis, respectively [8,19,20].

For patients who have tumour-positive LNs, MRI guidance enables new RT approaches that precisely target individual LNs and dose escalation, while sparing surrounding OARs. This could provide a minimally invasive alternative to ALND or conventionally fractionated boosts. The first step for more advanced regional RT is to deliver an additional RT boost, on top of standard elective loco-regional RT by WBI/AxRT. However, loco-regional RT is not likely to be delivered on the MRL due to the magnetic field that can raise the skin dose [21]. In this study we test whether tumour-positive LNs can be treated by a single LN boost (up to ablative) dose on the MRL, sequential to WBI/AxRT on a conventional accelerator. The purpose of this study is to evaluate the dosimetric feasibility of such an approach.

Methods and materials

Patient characteristics

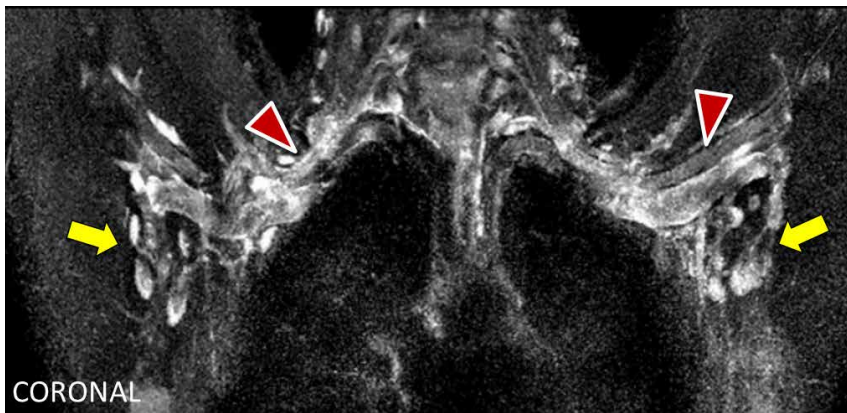
The Internal Review Board of UMC Utrecht approved the *MRI of regional lymph nodes in cT1-3N0 breast cancer and cTisN0 DCIS patients (MILANO)* trial, which is registered under trial number NL50046.041.14. Written informed consent was obtained from 26 patients. For the current study, five female participants were selected. All patients had early-stage breast cancer, or ductal carcinoma *in situ* (DCIS), without pathologically involved LNs (cTis-2N0) and were scheduled for BCS with sentinel-node biopsy (SNB). Two participants had right-sided breast cancer, while three patients had left-sided breast cancer or DCIS. Median age of the five patients was 58 yr (range: 40 – 68 yr). Their median body-mass-index (BMI) was 24 kg/m² (range: 18 – 35 kg/m²).

MRI and CT acquisition

Participants were scanned at RT Department of UMC Utrecht, from February - November 2015, on a 1.5 T wide-bore MRI scanner (Philips Ingenia, Best, The Netherlands) after BCS and SNB. Scanning was

performed in supine treatment position, i.e. with both arms abducted and supported by a 10° board (CIVCO, Reeuwijk, The Netherlands). An anterior receive coil was placed on top of two adjustable perspex bridges to prevent deformation of the outer body contour. A posterior receive coil was located in the scanner table. The acquired MRI scans included T1-weighted (T1w) spoiled gradient echo (SPGR), T2w (figure 1), and diffusion-weighted imaging (DWI) techniques. The T1w scan was acquired in the transverse plane, encompassing the body contour. The field-of-view (FOV) in caudo-cranial direction ranged from the mandible to below the ribs. Acquired resolution of the T1w scan was 1 x 1 x 1 mm³. The other MRI scans were acquired in the coronal plane, and their FOVs covered the axillary areas. Other relevant scanning parameters are described previously (chapters 4 and 5, and [15]).

Additional to MRI, all patients underwent standard postoperative CT imaging for RT planning. CT was acquired in supine treatment position, and on the same day as the postoperative MRI, with 3-mm slice thickness. For the current study, CT scans were only used to extract the mean value of Hounsfield Units (HU) in each lung.



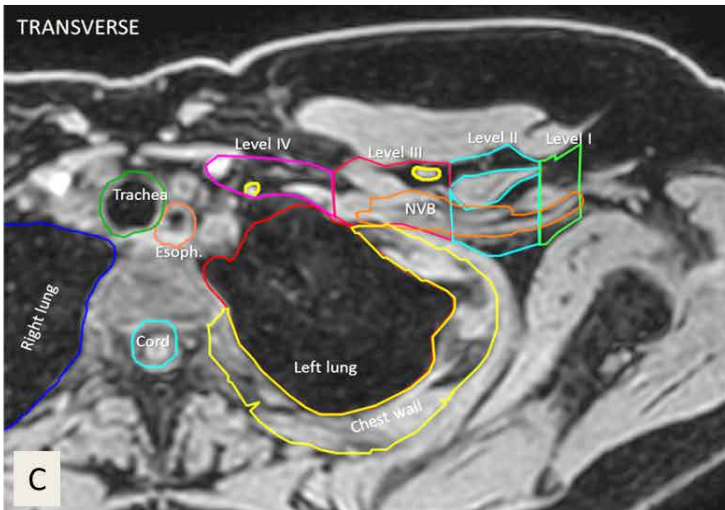
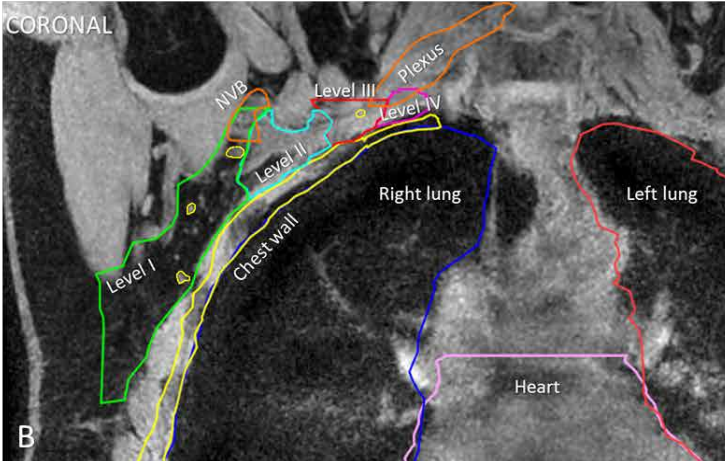
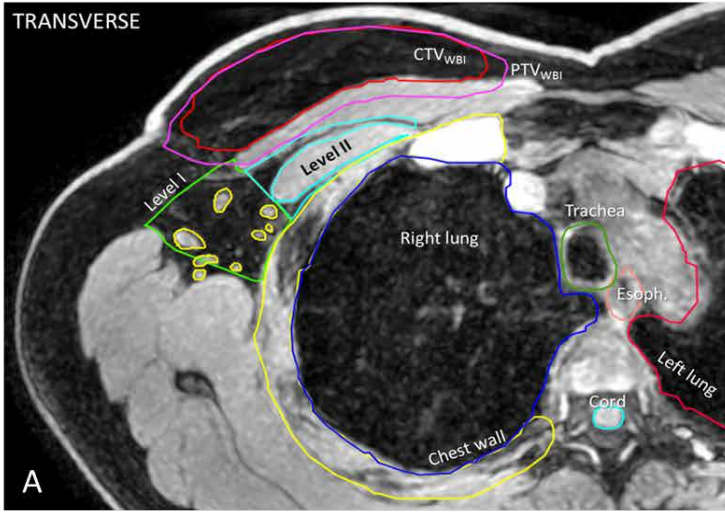
● *Figure 1 Example of a coronal MRI scan, acquired in supine treatment position, i.e. with both arms in abduction, at 1.5 T. Depicted is the water-only image of mDixon water-fat separation from a T2-w fast spin echo sequence, as optimized previously [15]. Individual LNs are seen in both axillae, which are indicated by the arrows. The brachial plexus can be identified on both sides (indicated by the arrowheads). Nerves spring from the spinal cord, converge into a bundle, which continues along the axillary artery and vein, and into the arm.*

OARs and target volumes on MRI

The T1w scan, with the largest FOV, was used as reference scan. The other MRI scans were registered to the reference scan for anatomical reference and structure identification. All volumes of interest (VOIs), i.e. OARs and target volumes, were delineated on the reference MRI scan by a radiation oncologist (figure 2), according to the European Society for Radiotherapy and Oncology (ESTRO) delineation guidelines [11]. These were developed for CT, but are also applicable for use on MRI. Minor adaptations were performed due to differences in soft-tissue visibility. Delineation was performed with contouring software Volumetool® [22]. The OARs included the body contour, heart, ipsilateral and contralateral breasts, lungs, oesophagus, trachea, spinal cord, chest wall, and brachial plexus. We defined the part of the brachial plexus that is medial to the lateral border of the m. scalenus anterior as *plexus*, and the part lateral to the lateral border of m. scalenus anterior as the *neurovascular bundle* (NVB).

In each patient, four LNs were selected on MRI for a total of twenty boost locations, distributed over the axillary levels, and possibly located close to OARs (table 1). In patients 3 and 4, no LNs were detected in level IV. Therefore, an additional boost LN was chosen in level I or II. Each selected LN was delineated to create a gross target volume (GTV_{boost}). All GTV_{boost} contours were then expanded by a 2-mm isotropic margin to generate the corresponding boost planning target volume (PTV_{boost}). The median of all PTV_{boost} volumes was 1.0 cc (range: 0.5 – 3.5 cc).

►► *Figure 2 Example of reference MRI scans (water-only images of mDixon in a T1w SPGR) with delineations. MRI is acquired in supine treatment position, i.e. with both arms in abduction. Transverse (A, C) and coronal (B) images are shown. Standard right-sided (A,B), and left-sided (C) axillary delineations are depicted: levels I, II, III, and IV (green, sky blue, red, and purple). Furthermore, OARs including the chest wall (yellow), spinal cord (sky blue), right/left lungs (blue/red), trachea (dark green), oesophagus (salmon), and plexus/NVB (orange) are depicted. Several individual LNs are delineated in yellow. OARs not indicated in the picture are the contralateral breast and body contour.*



Loco-regional RT consisted of whole-breast irradiation (WBI) and AxRT. For WBI, the clinical target volume (CTV_{WBI}) was delineated. A 5-mm margin was applied to the CTV_{WBI} to generate the planning target volume (PTV_{WBI}) of WBI, where the first 5 mm under the skin surface was excluded. The median volume of the PTV_{WBI} was 640 cc (range: 262 – 1045 cc). Furthermore, standard clinical target volumes for AxRT (CTV_{AxRT}) were delineated. We will refer to the axillary target contours, defined as levels I-IV, as axillary levels. The inter-pectoral level was incorporated in level II for our study. For the planning target volume in AxRT (PTV_{AxRT}), two AxRT scenarios were considered:

(AxRT-A) AxRT on levels I and II;

(AxRT-B) AxRT on levels I, II, III, and IV.

The choice for A or B depends on the location of the LN that is to receive an RT boost dose. If the LN is located in level I or II, scenario A was chosen. Then, the total CTV_{AxRT} is the union of level I and II. If the boost is in levels III or IV, scenario B was selected, and the total CTV_{AxRT} encompasses levels I-IV. A 5-mm margin was applied to the total CTV_{AxRT} for both scenarios, thereby generating the total PTV_{AxRT} , where the chest wall and the first 5 mm under the skin surface were excluded. For all five patients, PTV_{AxRT} of both scenarios A and B were delineated. The median volumes of axillary levels I, II, III, and IV were 117 cc (range: 90 - 200 cc), 129 cc (range: 63 – 169 cc), 48 cc (range: 33 – 51 cc), and 33 cc (range: 18 – 39.3 cc), respectively.

Pseudo-CT scans

Electron density (ED) values were attributed to each voxel in the reference MRI scans. This was done by bulk assignment of water (0 HU) to the body, and air (-1000 HU) to voxels outside the body. A bulk value was attributed to all voxels in each lung that was equal to the mean HU value from the RT-planning CT (median right lung: -786 HU; median left lung: -779 HU). Thereby, a pseudo-CT (pCT) scan was generated for each patient. All delineations from the reference MRI scan were transferred onto the pCT scans for treatment planning of both WBI/AxRT and boost delivery.

● *Table 1 Locations of all four boosts (a, b, c, d) per patient, relative to axillary levels, and to OARs nearby. The corresponding AxRT scenarios (A or B) are listed in the last column.*

<i>Boosts per patient (side)</i>	<i>Axillary level</i>	<i>Relative location of LN</i>	<i>AxRT scenario</i>
<i>Patient 1 (Left)</i>			
a	Level I	Near lateral border	A
b	Level II	Near medial border; < 5mm to chest wall	A
c	Level III	Near lateral border; < 5mm to plexus	B
d	Level IV	Near superior border; < 10 mm to plexus	B
<i>Patient 2 (Right)</i>			
a	Level I	Central	A
b	Level II	Near medial border; < 10 mm to chest wall and NVB	A
c	Level III	Near lateral border; < 10 mm to NVB	B
d	Level IV	Near medial border; < 15 mm to plexus	B
<i>Patient 3 (Left)</i>			
a	Level I	Near inferior border; < 5 mm to chest wall	A
b	Level II	Near medial border; < 5 mm to chest wall and NVB	A
c	Level III	Near lateral border; < 5 mm to chest wall; < 10 mm to plexus	B
d	Level II	Near superior border; < 5 mm to NVB	A
<i>Patient 4 (Right)</i>			
a	Level I	Near superior/lateral border	A
b	Level II	Interpectoral	A
c	Level III	Central; < 10 mm to chest wall	B
d	Level I	Near superior border; < 10 mm to NVB	A
<i>Patient 5 (Left)</i>			
a	Level I	Near inferior border; < 10 mm to chest wall	A
b	Level II	Near lateral border; < 5 mm to chest wall	A
c	Level III	Near superior/lateral border; < 5 mm to NVB	B
d	Level IV	Near medial border	B

AxRT = axillary radiotherapy; NVB = neurovascular bundle.

Boost dose: 9, 11, and 13 Gy

Our aim was to investigate the dosimetric effect of a boost dose for safe RT delivery. We used the linear-quadratic (LQ) model to recalculate dose into EQD₂, i.e. equivalent to dose delivered in 2-Gy fractions [23,24], according to:

$$\text{EQD}_2 = nd \left(\frac{d + \alpha/\beta}{2 \text{ Gy} + \alpha/\beta} \right), \quad (1)$$

where n is the number of fractions, d is the fraction dose, and the α/β ratio is specific for each delineated structure. For target volumes, we take $\alpha/\beta = 3.5$ Gy [7]. A WBI/AxRT prescription of $16 \times 2.66 \text{ Gy} = 42.56 \text{ Gy}$ is therefore equivalent to 47.67 Gy in EQD₂. Currently, most sequential boost doses are prescribed to deliver up to 66-70 Gy in EQD₂. This implies, additional to WBI/AxRT, a boost dose of 18.3-22.3 Gy in EQD₂. If this is delivered in a single fraction, that amounts to 8.4-9.5 Gy. Therefore, we investigated a minimal boost dose of $1 \times 9 \text{ Gy}$ to each LN. Secondly, we consider $1 \times 20 \text{ Gy} = 85.5 \text{ Gy}$ in EQD₂ to be an ablative dose [25–27]. This is equivalent to an additional 37.8 Gy in EQD₂ after WBI/AxRT, or 12.8 Gy in a single fraction. Thus, we investigated a $1 \times 13 \text{ Gy}$ boost dose as an upper limit. Thirdly, we considered the intermediate dose of $1 \times 11 \text{ Gy}$. Dose escalation within the PTV_{boost} was allowed up to 160% of the prescribed boost dose in order to enable a more conformal dose distribution around the target volume.

WBI and AxRT treatment planning

Treatment planning for simultaneous WBI/AxRT was performed on the pCT scans using Monaco software, version 5.1 (Elekta AB, Sweden), which is based on X-Ray Voxel Monte Carlo (XVMC) dose calculations [28]. Dose prescription for WBI/AxRT was $16 \times 2.66 \text{ Gy} = 42.56 \text{ Gy}$, delivered by volumetric modulated arc therapy (VMAT) with an Elekta Agility 6 MV photon beam. The VMAT set-up consisted of two partial arcs going clockwise and counter-clockwise over 210° on the ipsilateral side of the patient. For each patient, scenarios A and B were planned. Thus, in total ten WBI/AxRT plans were created, obeying clinical constraints (table 2). All VMAT dose plans were fully sequenced after fluence optimization, and were obtained in $2 \times 2 \times 2 \text{ mm}^3$ resolution.

● Table 2 Clinical constraints for the loco-regional RT plans, consisting of simultaneous WBI/AxRT, delivered by VMAT. The prescribed target dose is $16 \times 2.66 \text{ Gy} = 42.56 \text{ Gy}$.

Volume of interest	Constraint (EQD ₂)
PTV (breast and axillary levels)	$D_{95\%} > 95\%$
	$D_{107\%} < 2\text{cc}$
Lungs	MLD < 7 Gy
	Ipsilateral lung $V_{20\text{Gy}} < 35\%$
Heart	$V_{5\text{Gy}} < 10\%$
	$V_{10\text{Gy}} < 5\%$
	MHD < 3Gy
Contralateral breast	Mean < 5 Gy

PTV = planning target volume; $D_{95\%}$ = relative volume receiving at least 95% of the prescribed dose, or 40.43 Gy; $D_{107\%}$ = absolute volume receiving at least 107% of the prescribed dose, or 45.54 Gy; MLD = mean lung dose, averaged over both lungs; $V_{x\text{Gy}}$ = fraction of volume receiving at least X Gy; MHD = mean heart dose.

Boost treatment planning

Specially developed MRL treatment planning software (MRLTP) was used to generate boost plans on the pCT scans. MRLTP is the combination of a graphics processing unit (GPU)-oriented Monte Carlo dose calculation algorithm [29], and a central processing unit (CPU)-based iterative intensity-modulated RT (IMRT) optimization method using precalculated beamlet data [30]. A more detailed description of this set-up is reported by Kontaxis *et al.* (2015). A distinct advantage of this system is that it provides optimization of the fluence in a very short time-frame.

The characteristics of the MRL are incorporated in MRLTP, including the presence of the 1.5 T magnetic field. Furthermore, the patient table in the MRL does not move during dose delivery. As a consequence, the isocentre is fixed. The 7 MV photon beam is flattening-filter free and can rotate in full 360° around the patient. The field sizes are limited to 24 cm in caudo-cranial direction, and 56 cm in anterior-posterior direction. Boosts were simulated to be delivered by 11 IMRT fields, ranging over 220°. For all right-sided boosts, the beams ranged from -50° to 170° with

22° intervals. Left-sided beam angles were mirrored. All boost treatment plan optimizations were planned individually, so no class solution was applied. The final boost plans were based on the optimized fluence maps with 5-mm resolution, and the boost dose distributions consisted of $2 \times 2 \times 2 \text{ mm}^3$ voxels.

Evaluation of dose plans

Several dose parameters were calculated to evaluate dosimetric feasibility of additional boosts. The starting point for the boost was sufficient $\text{PTV}_{\text{boost}}$ coverage. Dose coverage parameters reported are $V_{90\%}$ and $V_{95\%}$, i.e. the relative volume of the $\text{PTV}_{\text{boost}}$ receiving at least 90% and 95% of the prescribed boost dose, respectively. Goal was to achieve $V_{90\text{Gy}} = 100\%$ and a minimum of at least $V_{95\%} > 95\%$, with the aim for $V_{95\%} > 99\%$. For a local maximum dose, we report the $D_{1\%}$, i.e. the maximum physical dose in 1% of the $\text{PTV}_{\text{boost}}$ volume. Extra dose to non-target tissue, i.e. all tissue excluding $\text{PTV}_{\text{boost}}$ volume, is described by parameters $V_{50\%}$ and $V_{95\%}$ in absolute volumes on the boost dose plans.

Physical dose plans of WBI/AxRT and boosts were converted to EQD_2 with specific α/β ratios for each VOI [26,32–34] (table 4). Total dose in EQD_2 was determined by a voxel-by-voxel addition of EQD_2 values of both boost dose plans and corresponding WBI/AxRT plans. Dose volume histograms (DVHs) were calculated for WBI/AxRT, boost dose, and total dose.

Clinical dose constraints for the contralateral breast, heart, lungs, oesophagus, spinal cord, plexus, NVB, and chest wall were evaluated on the total dose plans. These are derived from previous lung stereotactic body RT (SBRT) and single-fraction breast RT studies [20,27,35,36] (table 3). We used $D_{1\text{cc}}$, i.e. the maximum dose to 1 cc of the structure, for the brachial plexus as indication of maximum dose. Other relevant dosimetric parameters for the OARs were also derived, but not used as feasibility constraints. These parameters included the mean heart dose, and $D_{2\text{cc}}$, i.e. the dose to 2 cc of the structure, for the trachea.

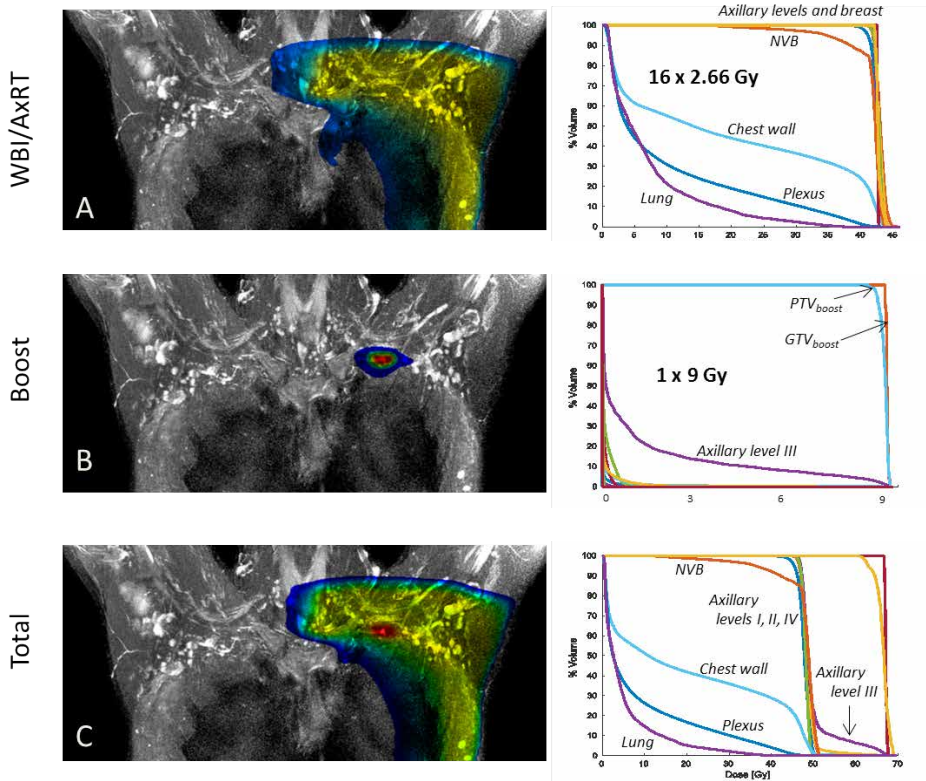
● Table 3 Per delineated structure, all α/β ratios are listed that are used to convert dose into EQD_2 with the LQ model. Clinical constraints in EQD_2 are also listed for radiosensitive OARs.

VOI	α/β ratio (Gy)	Clinical dose constraint (EQD_2)
Axillary levels	3.5	-
Ipsilateral breast	3.5	-
Contralateral breast	3	Mean < 5 Gy
Heart	3	V5Gy < 10% V10Gy < 5% MHD < 3 Gy
Lungs	3	MLD < 7 Gy
Oesophagus	3	Mean < 45 Gy
Spinal cord	2	D2cc < 50 Gy
Trachea	3	-
Plexus	2	D1cc < 66 Gy
NVB	2	D1cc < 66 Gy
Chest wall	3	D_{2cc} < 60 Gy

VOI = volume of interest; EQD_2 = dose equivalent to 2-Gy fractions; V_{xGy} = fraction of volume receiving at least X Gy; MHD = mean heart dose; MLD = mean lung dose, averaged over both lungs; D_{Ycc} = maximum dose given to Y cc of the volume; NVB = neurovascular bundle.

Results

Boost dose was successfully simulated for all 4 boost locations in 5 patients, for the delivery of 9 Gy, 11 Gy, and 13 Gy. This resulted in 60 boost plans. Addition of boost dose plans and corresponding AxRT/WBI plans resulted in 60 total dose plans. Figure 3 indicates an example.



● *Figure 3 An example of a WBI/AxRT dose plan, boost dose, and total dose plans, projected on a supine T2w MRI scan, on which individual axillary LNs can be distinguished. The corresponding DVHs are found right of the dose plan projections. Here, a LN boost in level III is selected. Accordingly, WBI/AxRT scenario B (levels I-IV) is planned for this boost (A), with a prescription of $16 \times 2.66 = 42.56$ Gy. The middle row (B) indicates the boost plan of 1×9 Gy. Excellent target coverage is achieved. The lower row (C) shows the total dose plan, acquired by adding the other two dose plans in EQD₂. OARs are indicated, including the ipsilateral lung, plexus, chest wall, and neurovascular bundle (NVB).*

Boost target coverage

The $V_{90\%}$ was 100% for all three boost dose scenarios and all PTV_{boost} locations (table 4). The median $V_{95\%}$ for PTV_{boost} was 99.0%, 98.3%, and 97.8%, respectively, for 9 Gy, 11 Gy and 13 Gy boost prescriptions. Dose escalation within the target raises the dose locally, as is reflected by the mean dose of the PTV_{boost} ranging between 103% and 144% of the prescribed boost dose, and the $D_{1\%}$ that ranged up to a maximum of 147%, 160%, and 153% of the prescribed boosts for 9 Gy, 11 Gy, and 13 Gy, respectively.

Dosimetric parameters for OARs

Clinical constraints for OARs were evaluated on the total dose plans (table 5; heart, trachea, contralateral breast not listed). All constraints on total OARs dose were obeyed. Generally, differences between 9 Gy, 11 Gy, 13 Gy boosts for the median $D_{1\text{cc}}$ values of the plexus and NVB were limited to 1 or 2 Gy and below the defined constraint of 66 Gy. One boosted LN close to the NVB caused the maximum $D_{1\text{cc}}$ of NVB to be raised from 60.4 Gy up to 63.2 Gy, between 9 Gy and 13 Gy prescribed boosts. For the chest wall, the $D_{2\text{cc}}$ did not go higher than 57.0 Gy at the 13-Gy boost level, which is under the clinical limit of 60 Gy. The $V_{63\text{Gy}}$ for the chest wall was always zero.

The extra dose to the heart was negligible in case of boosts up to 13 Gy. Moreover, the maximum extra MLD was 0.1 Gy. The additional mean contralateral breast dose was at most 0.2 Gy per boost dose. Thus, for the heart, lungs and contralateral breast, the clinical constraints (table 1) are still obeyed on the total dose plans. Dose increase to the trachea and oesophagus due to the boost was negligible, and independent of the boost dose. The median $D_{2\text{cc}}$ of the spinal cord was limited to 1.5 Gy at 9 Gy prescription, and was only raised by 0.1 Gy when boost dose went up to 13 Gy. Furthermore, the highest maximum $D_{2\text{cc}}$ was 10.4 Gy at maximum boost dose.

Extra dose to unspecified tissue

As indication of extra dose and conformality of plans, the $V_{50\%}$ and $V_{95\%}$ of unspecified tissue outside the PTVboost were calculated on the physical boost plans. For the 9-Gy boost dose, median $V_{4.5\text{Gy}}$ and $V_{8.6\text{Gy}}$ were 6.6 cc and 0.3 cc, respectively, with maximum values being 11.4 cc and 1.4 cc, respectively. For the 11-Gy boost plans, median $V_{5.5\text{Gy}}$ and $V_{10.5\text{Gy}}$ were 5.7 cc (maximum 12.6 cc) and 1.1 cc (maximum 1.4), respectively. For the highest boost level, 13 Gy, the median $V_{6.5\text{Gy}}$ and $V_{12.4\text{Gy}}$ were 5.2 cc (maximum 7.6 cc) and 0.4 cc (maximum 0.9 cc).

● *Table 4 Dosimetric target parameters for all 20 PTV_{boost} locations, throughout the four axillary levels, for planned boosts of 9 Gy, 11 Gy, and 13 Gy. Dose is derived from physical boost dose plans. Dose escalation was allowed in the PTV of up to 160% of the prescribed boost. Values are denoted as 'median (range)'.*

Dose parameters (Physical dose)	PTV _{boost} $V_{90\%}$ (%)	$V_{95\%}$ (%)	Mean (Gy)	$D_{1\%}$ (Gy)
Boost dose				
9 Gy	100 (99.9 – 100)	99.0 (96.2 - 100)	10.8 (9.3 – 12.8)	12.9 (9.9 – 14.3)
11 Gy	100 (99.9 -100)	98.3 (95.4 – 100)	13.3 (12.3 – 15.9)	16.1 (14.3 – 17.7)
13 Gy	99.8 (99.7 – 100)	97.8 (96.2 – 100)	15.5 (13.7 – 17.3)	18.3 (15.8 – 20.9)

PTV = *planning target volume*; $V_{x\%}$ = *relative volume receiving X% of the prescribed boost dose*; $D_y\%$ = *maximum dose given to Y% of the volume*.

● **Table 5** Dosimetric parameters of the most critical OARs, from all 20 boost locations throughout the axillary levels, for planned boosts of 9 Gy, 11 Gy, and 13 Gy, additional to WBI/AxRT. Dose is derived from the total dose plans (in EQD₂), i.e. after addition of WBI/AxRT and boost plans. Values are denoted as 'median (maximum)'.

Boost dose	Critical OARs		Chest wall D _{2cc} (Gy)	V _{50Gy} (cc)	Plexus D _{1cc} (Gy)	NVB D _{1cc} (Gy)	Lungs MLD (Gy)	Oesophagus Mean (Gy)	Spinal cord D _{2cc} (Gy)
	Dose parameters (EQD ₂ , total dose)	D _{2cc} (Gy)							
9 Gy	51.4 (53.5)	0 (0)	51.4 (53.5)	0 (0)	7.7 (54.6)	52.2 (60.4)	5.3 (6.1)	1.42 (4.7)	1.5 (8.2)
11 Gy	52.4 (54.7)	0 (0)	52.4 (54.7)	0 (0)	7.7 (55.4)	52.3 (62.2)	5.3 (6.1)	1.42 (4.7)	1.6 (8.3)
13 Gy	52.5 (57.0)	0 (0)	52.5 (57.0)	0 (0)	7.7 (56.6)	52.4 (63.2)	5.3 (6.1)	1.42 (4.7)	1.6 (10.2)
Constraint	< 60 Gy	< 16.3 cc	< 60 Gy	< 16.3 cc	< 66 Gy	< 66 Gy	< 7 Gy	< 45 Gy	< 50 Gy

OAR = organ at risk; NVB = neurovascular bundle; EQD₂ = equivalent to dose in 2-Gy fractions; DXcc = maximum dose given to X cc of the volume; V_{50Gy} = volume receiving at least Y Gy; MLD = mean lung dose, averaged over both lungs.

Discussion

The introduction of hybrid MRI/RT modalities enables new RT approaches aiming at individual LNs. Our work is, to our knowledge, the first to simulate axillary single-dose LN boosting. We investigated a single RT dose on the MRL, up to ablative dose levels, additional to elective loco-regional RT treatment for breast cancer patients on a conventional linac.

It is dosimetrically feasible to deliver an additional RT boost to individual LNs, up to potentially ablative dose in a single fraction. This was calculated in an MRL setting, thereby also incorporating 1.5-T magnetic-field effects. Dose increase to OARs due to higher boost dose was generally very limited, or negligible. This was true regardless of LN location in the axilla. Although LNs were located close to critical structures, such as the chest wall, NVB, and brachial plexus, all clinical constraints were obeyed. Clinical data on dose and dose constraints for one fraction is sparse. Therefore, we derived several clinical dose constraints from previous studies on single-fraction partial-breast RT, and hyper-fractionated lung SBRT treatments. In our study, the heart, lungs and contralateral breast received negligible extra dose due to the single-fraction dose. This is similar to what was found in other studies [27,37,38]. Maximum spinal cord dose, oesophagus dose, and mean lung dose were lower, and maximum dose to plexus/NVB was comparable to axillary boosts delivered with a conventionally fractionated schedule [39,40]. Chest wall dose in our study was very low compared to lung SBRT studies [32]. Absolute volumes of unspecified tissue outside the boost volumes receiving 95% of prescribed dose were kept low, especially compared to current axillary boost techniques [39,40]. In the study by Charaghvandi *et al.* (2015), associated dose to unspecified tissue outside the targets was similar, with higher maximum values.

The starting point of our study was standard loco-regional RT treatment by WBI/AxRT, as currently performed on a conventional linac. On the MRL, electrons exiting the skin are bent back towards the skin surface due to the magnetic field. This electron return effect (ERE) leads to higher skin dose for WBI on the MRL [21], due to presence of large and superficial targets. We therefore planned the WBI/AxRT in the setting of a standard linac, and the additional boost RT on the MRL.

Delineations were performed on the reference MRI scan, a T1w SPGR, which has an inherently high geometric fidelity [41] and a high 1-mm isotropic resolution. Most LNs are at most a few mm in diameter, which is in the order of several voxels in one spatial direction. A small PTV margin of 2 mm was chosen for each PTV_{boost} , in order to take into account errors attributed to delineation uncertainty, and to incorporate any uncertainties due to intra-fraction motion. Since PTV_{boost} volumes were small, at a median of 1.0 cc, the target DVH parameters in the treatment planning are very sensitive. Due to this, it was difficult to always achieve target $V_{95\%}$ coverage of 99% or higher. Furthermore, since Monte Carlo dose calculations may induce inaccuracies on individual voxels, we chose $D_{1\%}$ as maximum dose indication of the boost volumes, instead of the maximum dose in one voxel.

There are several limitations to our study. A simplification of HU values into three classes was performed to obtain pCT scans. Assignment by bulk density may lead to dosimetric differences compared to using ED from actual CT scans. When complex bony structures are involved, pCT creation by bulk density assignment becomes substantially inaccurate [42,43]. However, for RT in tumour sites with an abundance of soft tissue, e.g. prostate and pancreas, differences are small [44,45]. This is also expected for the breast and axillary LNs, where the ribs and humeral head are the only bony structures potentially involved. Dedicated methods are in development to directly obtain CT substitutes from MRI acquisition [42,46].

In our study we used the LQ model, where overall treatment time was not taken into account. The LQ model estimates the effect of changing fractionation schemes [23,24]. However, the reliability of the model for high fraction dose is contested [47]. The model could overestimate the effectiveness of cell killing by a single high dose, and α/β parameters may no longer be valid for high-dose (>10 Gy) fractions. While using the LQ model, potential overestimation of dose response in the current set-up should be kept in mind. Effects of high dose *in vivo* could therefore be smaller than expected. A generalized LQ (gLQ) model could provide more accurate estimations for high dose [47,48]. However, radiobiological parameters used in proposed gLQ models, other than α/β ratios, are generally not available for breast RT.

In our simulation study, only cN0 patients were included, i.e. patients without pathologically involved LNs. Since sensitivity of MRI for detection of tumour-positive LNs is low, identification of involved LNs was not possible. Consequently, virtual boosts were planned on benign LNs. Malignant LNs in reality can show differences on MRI, including varying morphology and difference in T2 values, compared to benign LNs. Current diagnostic MRI techniques show greatly varying specificity and sensitivity for LN staging [49]. In clinical practice, dedicated MRI-only methods with high specificity and sensitivity will be essential for the development of MRI-guided RT. Very good results have been shown with ultra-small superparamagnetic iron oxide (USPIO)-enhanced T2*-weighted (T2*w) imaging, where the most promising is a combination of T1w/T2w and USPIO-enhanced T2*w imaging [50]. It may also be possible to combine MRI with positron emission tomography (PET) scans for accurate LN staging [51]. For RT target definition, LNs that show fludeoxyglucose (FDG) uptake on PET/CT scans could be merged with MRI.

The PTV_{boost} volumes in our study were small, at median of 1.0 cc, ranging between 0.5 cc and 3.5 cc. In case of macrometastasis, a LN can be enlarged, and the corresponding PTV_{boost} volume will on average be larger. However, LN size alone is not related to metastatic involvement with high specificity and sensitivity [52]. Also non-enlarged LNs can be metastatic. Most patients who have involved LNs are treated with neoadjuvant systemic therapy, and the majority of these patients have no bulky involved LNs after neoadjuvant treatment. FDG-PET/CT shows a high specificity, and if LNs show FDG uptake, this is an indication for a conventionally fractionated RT boost. Therefore, volumes of these non- or slightly enlarged tumour-positive LNs are similar to the LN volumes in our study.

On-line MRI guidance secures accurate target definition, directly adjusted to the actual patient anatomy. Since the MRL is primarily designed for target tracking and dynamic RT planning, any associated uncertainty margins are minimized and the need for (fiducial) markers is omitted. With successful MRI-based identification of benign and malignant LNs, there are possibilities of highly precise RT of tumour-positive LNs. The first step is to deliver a boost additional to WBI/AxRT, which our study showed is

dosimetrically feasible regardless of LN location. An RT boost to single LNs with an ablative dose, on the MRL, may serve as an alternative strategy for patients with tumour-positive LNs, who are currently treated by ALND with/without AxRT, or a fractionated 16-20 Gy boost on the involved LNs after AxRT. MRI-guided boost delivery could effectively omit the need of axillary surgery, reduce fractionation schedules, which might lead to decreased toxicity and better quality of life. The next step is to initiate a clinical trial to investigate the therapeutic effectiveness and related toxicity of a single-fraction boost approach. Moreover, at UMC Utrecht, various other RT approaches are under investigation, including simultaneous boost of several LNs on the MRL. In the future, on-line MRI guidance may be fully exploited for highly effective, minimally burdening regional RT in breast cancer patients.

Conclusions

It is dosimetrically feasible to deliver single-fraction RT boosts to single LNs, in the MRL, additional to elective conventional loco-regional RT. Boosts up to ablative dose can be delivered, regardless of axillary LN location. This enables further possibilities for MRI-guided RT aiming at individual LNs. This may lead to omission of axillary surgery, reduction of RT fractionation schedules, and decreased risk of treatment-induced toxicity in selected breast cancer patients, while will be investigated in future clinical studies.

Acknowledgements

The authors hereby thank Vincent Scholten for his input.

References

- [1] Dempsey J, Dionne B, Fitzsimmons J, Haghigat A, Li J, Low D, et al. WE-E-ValA-06: A Real-Time MRI Guided External Beam Radiotherapy Delivery System. *Med Phys* 2006;33:2254. doi:10.1118/1.2241803.
- [2] Fallone BG, Murray B, Rathee S, Stanescu T, Steciw S, Vidakovic S, et al. First MR images obtained during megavoltage photon irradiation from a prototype integrated linac-MR system. *Med Phys* 2009;36:2084–8.
- [3] Raaymakers BW, Lagendijk JJW, Overweg J, Kok JGM, Raaijmakers AJE, Kerkhof EM, et al. Integrating a 1.5 T MRI scanner with a 6 MV accelerator: proof of concept. *Phys Med Biol* 2009;54:N229–37. doi:10.1088/0031-9155/54/12/N01.
- [4] Lagendijk JJW, Raaymakers BW, Raaijmakers AJE, Overweg J, Brown KJ, Kerkhof EM, et al. MRI/linac integration. *Radiother Oncol* 2008;86:25–9. doi:10.1016/j.radonc.2007.10.034.
- [5] Donker M, Litière S, Werutsky G, Julien J-P, Fentiman IS, Agresti R, et al. Breast-conserving treatment with or without radiotherapy in ductal carcinoma In Situ: 15-year recurrence rates and outcome after a recurrence, from the EORTC 10853 randomized phase III trial. *J Clin Oncol* 2013;31:4054–9. doi:10.1200/JCO.2013.49.5077.
- [6] Whelan TJ, Olivotto IA, Parulekar WR, Ackerman I, Chua BH, Nabid A, et al. Regional Nodal Irradiation in Early-Stage Breast Cancer. *N Engl J Med* 2015;373:307–16. doi:10.1056/NEJMoa1415340.
- [7] Haviland JS, Owen JR, Dewar JA, Agrawal RK, Barrett J, Barrett-Lee PJ, et al. The UK Standardisation of Breast Radiotherapy (START) trials of radiotherapy hypofractionation for treatment of early breast cancer: 10-year follow-up results of two randomised controlled trials. *Lancet Oncol* 2013;14:1086–94. doi:10.1016/S1470-2045(13)70386-3.
- [8] Badiyan SN, Shah C, Arthur D, Khan AJ, Freedman G, Poppe MM, et al. Hypofractionated regional nodal irradiation for breast cancer: Examining the data and potential for future studies. *Radiother Oncol* 2014;110:39–44. doi:10.1016/j.radonc.2013.12.006.
- [9] Ivens D, Hoe AL, Podd TJ, Hamilton CR, Taylor I, Royle GT. Assessment of morbidity from complete axillary dissection. *Br J Cancer* 1992;66:136–8.
- [10] Chandra RA, Miller CL, Skolny MN, Warren LEG, Horick N, Jammallo LS, et al. Radiation therapy risk factors for development of lymphedema in patients treated with regional lymph node irradiation for breast cancer. *Int J Radiat Oncol Biol Phys* 2015;91:760–4. doi:10.1016/j.ijrobp.2014.12.029.
- [11] Offersen B V, Boersma LJ, Kirkove C, Hol S, Aznar MC, Biete Sola A, et al. ESTRO consensus guideline on target volume delineation for elective radiation therapy of early stage breast cancer. *Radiother Oncol* 2015;114:3–10. doi:10.1016/j.radonc.2014.11.030.
- [12] Verhoeven K, Weltens C, Remouchamps V, Mahjoubi K, Veldeman L, Lengele B, et al. Vessel based delineation guidelines for the elective lymph node regions in breast cancer radiation therapy - PROCAB guidelines. *Radiother Oncol* 2015;114:11–6. doi:10.1016/j.radonc.2014.11.008.
- [13] Nielsen MH, Berg M, Pedersen AN, Andersen K, Glavicic V, Jakobsen EH, et al. Delineation of target volumes and organs at risk in adjuvant radiotherapy of early breast cancer: national guidelines and contouring atlas by the Danish Breast Cancer Cooperative Group. *Acta Oncol* 2013;52:703–10. doi:10.3109/0284186X.2013.765064.

- [14] Gentile MS, Usman AA, Neuschler EI, Sathiaseelan V, Hayes JP, Small W. Contouring Guidelines for the Axillary Lymph Nodes for the Delivery of Radiation Therapy in Breast Cancer: Evaluation of the RTOG Breast Cancer Atlas. *Int J Radiat Oncol* 2015;93:257–65. doi:10.1016/j.ijrobp.2015.07.002.
- [15] van Heijst TCF, van Asselen B, Pijnappel RM, Cloos-van Balen M, Lagendijk JJW, van den Bongard HJGD, et al. MRI sequences for the detection of individual lymph nodes in regional breast radiotherapy planning. *Br J Radiol* 2016;20160072. doi:10.1259/bjr.20160072.
- [16] Grayev A, Reeder S, Hanna A. Use of chemical shift encoded magnetic resonance imaging (CSE-MRI) for high resolution fat-suppressed imaging of the brachial and lumbosacral plexuses. *Eur J Radiol* 2016;85:1199–207. doi:10.1016/j.ejrad.2016.04.002.
- [17] Lecouvet FE. Whole-Body MR Imaging: Musculoskeletal Applications. *Radiology* 2016;279:345–65. doi:10.1148/radiol.2016142084.
- [18] Neumann H, Neurath MF, Vieth M, Lever FM, Meijer GJ, Lips IM, et al. Innovative techniques in evaluating the esophagus; imaging of esophageal morphology and function; and drugs for esophageal disease. *Ann N Y Acad Sci* 2013;1300:11–28. doi:10.1111/nyas.12233.
- [19] Guenzi M, Blandino G, Vidili MG, Aloï D, Configliacco E, Verzanini E, et al. Hypofractionated irradiation of infra-supraclavicular lymph nodes after axillary dissection in patients with breast cancer post-conservative surgery: impact on late toxicity. *Radiat Oncol* 2015;10:177. doi:10.1186/s13014-015-0480-y.
- [20] Creach KM, El Naqa I, Bradley JD, Olsen JR, Parikh PJ, Drzymala RE, et al. Dosimetric predictors of chest wall pain after lung stereotactic body radiotherapy. *Radiother Oncol* 2012;104:23–7. doi:10.1016/j.radonc.2012.01.014.
- [21] van Heijst TCF, den Hartogh MD, Lagendijk JJW, van den Bongard HJGD, van Asselen B. MR-guided breast radiotherapy: feasibility and magnetic-field impact on skin dose. *Phys Med Biol* 2013;58:5917–30. doi:10.1088/0031-9155/58/17/5917.
- [22] Bol GH, Kotte ANTJ, van der Heide UA, Lagendijk JJW. Simultaneous multi-modality ROI delineation in clinical practice. *Comput Methods Programs Biomed* 2009;96:133–40. doi:10.1016/j.cmpb.2009.04.008.
- [23] Barendsen G. Dose fractionation, dose rate and iso-effect relationships for normal tissue responses. *Int J Radiat Oncol* 1982;8:1981–97. doi:10.1016/0360-3016(82)90459-X.
- [24] Fowler JF. The linear-quadratic formula and progress in fractionated radiotherapy. *Br J Radiol* 1989;62:679–94. doi:10.1259/0007-1285-62-740-679.
- [25] Van Limbergen E, Van der Schueren E, Van den Bogaert W, Van Wing J. Local control of operable breast cancer after radiotherapy alone. *Eur J Cancer Clin Oncol* 1990;26:674–9. doi:10.1016/0277-5379(90)90115-A.
- [26] Marks LB, Yorke ED, Jackson A, Ten Haken RK, Constine LS, Eisbruch A, et al. Use of Normal Tissue Complication Probability Models in the Clinic. *Int J Radiat Oncol* 2010;76:S10–9. doi:10.1016/j.ijrobp.2009.07.1754.
- [27] Charaghvandi RK, den Hartogh MD, van Ommen A-MLN, de Vries WJH, Scholten V, Moerland MA, et al. MRI-guided single fraction ablative radiotherapy for early-stage breast cancer: a brachytherapy versus volumetric modulated arc therapy dosimetry study. *Radiother Oncol* 2015;117:477–82. doi:10.1016/j.radonc.2015.09.023.
- [28] Fippel M. Fast Monte Carlo dose calculation for photon beams based on the VMC electron algorithm. *Med Phys* 1999;26:1466–75. doi:10.1118/1.598676.
- [29] Hissoiny S, Ozell B, Bouchard H, Després P. GPUMCD: A new GPU-oriented Monte Carlo dose calculation platform. *Med Phys* 2011;38:754–64. doi:10.1118/1.3539725.

- [30] Ziegenhein P, Kamerling CP, Bangert M, Kunkel J, Oelfke U. Performance-optimized clinical IMRT planning on modern CPUs. *Phys Med Biol* 2013;58:3705–15. doi:10.1088/0031-9155/58/11/3705.
- [31] Kontaxis C, Bol GH, Lagendijk JJW, Raaymakers BW. Towards adaptive IMRT sequencing for the MR-linac. *Phys Med Biol* 2015;60:2493–509. doi:10.1088/0031-9155/60/6/2493.
- [32] Thibault I, Chiang A, Erler D, Yeung L, Poon I, Kim A, et al. Predictors of Chest Wall Toxicity after Lung Stereotactic Ablative Radiotherapy. *Clin Oncol* 2016;28:28–35. doi:10.1016/j.clon.2015.06.009.
- [33] Yarnold J, Bentzen SM, Coles C, Haviland J. Hypofractionated Whole-Breast Radiotherapy for Women With Early Breast Cancer: Myths and Realities. *Int J Radiat Oncol* 2011;79:1–9. doi:10.1016/j.ijrobp.2010.08.035.
- [34] Hadziahmetovic M, Loo BW, Timmerman RD, Mayr NA, Wang JZ, Huang Z, et al. Stereotactic body radiation therapy (stereotactic ablative radiotherapy) for stage I non-small cell lung cancer--updates of radiobiology, techniques, and clinical outcomes. *Discov Med* 2010;9:411–7.
- [35] Grimm J, LaCouture T, Croce R, Yeo I, Zhu Y, Xue J. Dose tolerance limits and dose volume histogram evaluation for stereotactic body radiotherapy. *J Appl Clin Med Phys* 2011;12:3368.
- [36] Mulryan K, Leech M, Forde E. Effect of stereotactic dosimetric end points on overall survival for Stage I non-small cell lung cancer: A critical review. *Med Dosim* 2015;40:340–6. doi:10.1016/j.meddos.2015.04.005.
- [37] Palta M, Yoo S, Adamson JD, Prosnitz LR, Horton JK. Preoperative single fraction partial breast radiotherapy for early-stage breast cancer. *Int J Radiat Oncol Biol Phys* 2012;82:37–42. doi:10.1016/j.ijrobp.2010.09.041.
- [38] Horton JK, Blitzblau RC, Yoo S, Geradts J, Chang Z, Baker JA, et al. Preoperative Single-Fraction Partial Breast Radiation Therapy: A Novel Phase 1, Dose-Escalation Protocol With Radiation Response Biomarkers. *Int J Radiat Oncol* 2015;92:846–55. doi:10.1016/j.ijrobp.2015.03.007.
- [39] Wang X, Yu TK, Salehpour M, Zhang SX, Sun TL, Buchholz T a. Breast cancer regional radiation fields for supraclavicular and axillary lymph node treatment: is a posterior axillary boost field technique optimal? *Int J Radiat Oncol Biol Phys* 2009;74:86–91. doi:10.1016/j.ijrobp.2008.07.016.
- [40] Hernandez V, Arenas M, Müller K, Gomez D, Bonet M. An optimized posterior axillary boost technique in radiation therapy to supraclavicular and axillary lymph nodes: A comparative study. *Med Dosim* 2013;38:413–7. doi:10.1016/j.meddos.2013.05.003.
- [41] Torfeh T, Hammoud R, Perkins G, McGarry M, Aouadi S, Celik A, et al. Characterization of 3D geometric distortion of magnetic resonance imaging scanners commissioned for radiation therapy planning. *Magn Reson Imaging* 2016;34:645–53. doi:10.1016/j.mri.2016.01.001.
- [42] Korhonen J, Kapanen M, Keyriläinen J, Seppälä T, Tuomikoski L, Tenhunen M. Absorbed doses behind bones with MR image-based dose calculations for radiotherapy treatment planning. *Med Phys* 2013;40:011701. doi:10.1118/1.4769407.
- [43] Hoogcarspel SJ, Van der Velden JM, Lagendijk JJW, van Vulpen M, Raaymakers BW. The feasibility of utilizing pseudo CT-data for online MRI based treatment plan adaptation for a stereotactic radiotherapy treatment of spinal bone metastases. *Phys Med Biol* 2014;59:7383–91. doi:10.1088/0031-9155/59/23/7383.

- [44] Prior P, Chen X, Botros M, Paulson ES, Lawton C, Erickson B, et al. MRI-based IMRT planning for MR-linac : comparison between CT- and MRI-based plans for pancreatic and prostate cancers *. *Phys Med Biol* 2016;3819:3819. doi:10.1088/0031-9155/61/10/3819.
- [45] Chen L, Price RA, Wang L, Li J, Qin L, McNeeley S, et al. MRI-based treatment planning for radiotherapy: Dosimetric verification for prostate IMRT. *Int J Radiat Oncol* 2004;60:636–47. doi:10.1016/j.ijrobp.2004.05.068.
- [46] Johansson A, Karlsson M, Nyholm T. CT substitute derived from MRI sequences with ultrashort echo time. *Med Phys* 2011;38:2708. doi:10.1118/1.3578928.
- [47] Wang JZ, Huang Z, Lo SS, Yuh WTC, Mayr N a. A generalized linear-quadratic model for radiosurgery, stereotactic body radiation therapy, and high-dose rate brachytherapy. *Sci Transl Med* 2010;2:39ra48–39ra48. doi:10.1126/scitranslmed.3000864.
- [48] Zhang C, Mayr NA, Lo SS, Lu L, Li K, Zheng Y, et al. The α/β ratio dose-range independent: application of the generalized linear-quadratic (gLQ) model. *J Radiat Oncol* 2015;4:309–14. doi:10.1007/s13566-015-0207-6.
- [49] Harnan SE, Cooper KL, Meng Y, Ward SE, Fitzgerald P, Papaioannou D, et al. Magnetic resonance for assessment of axillary lymph node status in early breast cancer: a systematic review and meta-analysis. *Eur J Surg Oncol* 2011;37:928–36. doi:10.1016/j.ejso.2011.07.007.
- [50] Kuijs VJL, Moosdorff M, Schipper RJ, Beets-Tan RGH, Heuts EM, Keymeulen KBMI, et al. The role of MRI in axillary lymph node imaging in breast cancer patients: a systematic review. *Insights Imaging* 2015;6:203–15. doi:10.1007/s13244-015-0404-2.
- [51] Cooper KL, Meng Y, Harnan S, Ward SE, Fitzgerald P, Papaioannou D, et al. Positron emission tomography (PET) and magnetic resonance imaging (MRI) for the assessment of axillary lymph node metastases in early breast cancer: systematic review and economic evaluation. *Health Technol Assess* 2011;15:iii – iv, 1–134. doi:10.3310/hta15040.
- [52] Obwegeser R, Lorenz K, Hohlagschwandtner M, Czerwenka K, Schneider B, Kubista E. Axillary Lymph Nodes in Breast Cancer: Is Size Related to Metastatic Involvement? *World J Surg* 2000;24:546–50. doi:10.1007/s002689910088.

“The important thing is not to stop questioning;
never lose a holy curiosity.”

Albert Einstein



Chapter 7

Summary and general discussion



Summary

With the introduction of the University Medical Center (UMC) Utrecht magnetic resonance imaging (MRI) linear accelerator (MRL), on-line MRI guidance for radiation therapy (RT) treatments is possible. The MRL enables very precise and localized RT treatments for a wide range of tumour sites. This thesis explores implementation of the MRL for local and regional breast-cancer RT treatments.

Chapters 2 and 3 focus on physical aspects concerning local breast RT treatments, i.e. whole-breast irradiation (WBI) and accelerated partial-breast irradiation (APBI). The 1.5 T magnetic field has an influence on the dosimetry, and most prominently near tissue interfaces such as the skin. As a consequence, the skin dose can be raised by the magnetic field in breast RT treatments. In **chapter 2** we describe a treatment-planning study on computed tomography (CT) scans from 10 early-stage breast-cancer patients, scanned in supine treatment position, after breast-conserving surgery (BCS). Target volumes and relevant organs-at-risk (OARs) were delineated, including the skin, defined as the first 5 mm under the surface. We investigated three intensity-modulated RT (IMRT) scenarios: a traditional tangential WBI set-up (16 x 2.66 Gy), a 7-field WBI scenario (16 x 2.66 Gy), and an APBI set-up with 7 fields (10 x 3.85 Gy). Dedicated MRL treatment planning software was employed, thereby taking into account the MRL's characteristics, including the magnetic field, fixed isocentre, and field sizes. Dose was calculated with zero magnetic field, and in presence of a 0.35 T and 1.5 T magnetic field. Skin dose was increased significantly in both WBI set-ups in presence of a non-zero magnetic field. This is a potential drawback. Conversely, no significant dosimetric effects were observed for the APBI approach. This opens possibilities for developing MRI-guided APBI approaches in the MRL.

For safe and effective APBI treatments on the MRL, the influence of intra-fraction motion, i.e. motion during RT delivery is becoming more relevant, as targets are smaller and geometric miss is more likely. We assessed intra-fraction motion with MRI, as described in **chapter 3**. Analysis was performed on scans from 21 early-stage breast-cancer patients who were scanned both before and after BCS in supine RT position. Motion on two time-scales was inferred, in order to ascertain effects due to respiration

and whole-body shifts. High-temporal 2-dimensional (2D) cinematic MRI (cine-MRI) series, acquired every 0.3 s during 2 min, and three 3D MRI scans, acquired over 20 min, were performed. Motion in sub-second time-scale was generally regular and limited to a median of 2 mm. Infrequently, large but temporary deviations were observed (up to 13 mm), induced by deep inspiration. Motion over multi-minute time-scales varied more, although medians were restricted to 2.2 mm or lower. Large whole-body shifts (up to 15 mm over 19 min) were sparsely found. No differences were observed in motion before and after BCS. The impact of intra-fraction motion may affect adequate RT delivery for longer treatment durations. On the MRL, the focus is on new (ablative) techniques (as in **chapter 6**) requiring high fraction doses and resulting in longer treatment times. Therefore, some form of motion management may be necessary on the MRL.

Chapters 4, 5, and 6 focus on MRI-guided RT of regional lymph nodes (LNs). In conventional regional RT for breast-cancer patients, target volumes are contoured on CT, defined by anatomical boundaries. More accurate target delineation could be achieved by MRI, which can potentially visualize regional LNs directly in relation to their surrounding OARs.

We optimized several MRI methods for the purpose of regional RT planning, as described in **chapter 4**. The scans were first optimized in 10, and then evaluated in another 12 healthy female volunteers. They included a T1-weighted (T1w), three T2-weighted (T2w), and a diffusion-weighted MRI (DWI) technique. Qualitatively, they were assessed on several aspects for RT planning suitability. Quantitative evaluation was performed by scoring numbers of LNs per scan per volunteer. Two T2w fast spin echo (FSE) methods showed the highest LN numbers (median 24 axillary LNs, $p < 0.05$ compared to all other methods), high contrast, excellent fat suppression and insensitivity to motion during acquisition. A third T2w sequence and DWI showed fewer LNs (14 and 10 LNs) and were unsuitable for RT planning due to motion sensitivity and geometrical distortions. The T1w MRI showed an intermediate number of LNs (17 LNs), and provided valuable anatomical reference information, but lacked LN contrast to surrounding tissues. The two T2w FSE techniques and T1w MRI could be excellent complementary tools for LN visualization in RT planning.

Both anatomy and endurance for undergoing MRI may differ between healthy female volunteers (**chapter 4**) and patients. Axillary surgery, including sentinel-node biopsy (SNB), may also influence the anatomy and posture endurance for undergoing MRI. Finally, reproducibility of LN detection using these MRI methods is of utmost importance for RT planning. Therefore, the feasibility of MRI in patients should be evaluated. In **chapter 5** we describe results from the NL50046.041.14 (*MILANO*) patient study, for which we scanned 23 cTis-2N0M0 breast-cancer patients before and after BCS with SNB, with MRI in supine treatment position, additional to postoperative RT-planning CT. Endurance for undergoing MRI was good, and unaffected by SNB. Individual LNs were identified by a multidisciplinary team of observers on both pre- and post-SNB MRI scans, and on postoperative CT. Although post-surgery effects were visible on MRI, numbers of LNs identified on postoperative MRI (median 26 LNs per patient) were highly reproducible ($p = 1.00$) compared to preoperative MRI, when adding the number of excised sentinel LNs (SNs). LN detection on MRI was significantly higher than on CT (median 11 LNs, $p < 0.001$). The majority of LNs, including all 33 SNs, were found in axillary level I. Up to 8 LNs per patient were located exterior to the axillary contours (within 5 mm). Volumes of LN-based delineations on MRI were considerably smaller than the standard axillary contours (at most 3% per respective axillary level), even after expansion by a 5-mm margin (at most 46% per axillary level). Thus, MRI of regional LNs is feasible and reproducible in breast-cancer patients, before and after SNB. This may enable personalized MRI-guided RT strategies on individual LNs and lead to reduced irradiated volume, compared to standard target volumes.

MRI techniques as presented in **chapters 4 and 5** may further introduce alternative treatments for breast-cancer patients with tumour-positive LNs. In **chapter 6** we describe a treatment-planning study which aims to deliver a single-fraction boost dose to individual LNs on the MRL, additional to standard loco-regional RT, consisting of WBI and elective axillary RT (AxRT). A sequential approach was chosen due to the possibly induced skin dose increase for large fields (**chapter 2**). MRI scans from five patients in the aforementioned *MILANO* trial were used for delineation of standard axillary targets, the whole breast, and OARs, including the brachial plexus, heart, trachea, lungs and chest wall. Per patient, four LNs were selected, throughout the axillary levels, and delineated. A 2-mm

planning target volume (PTV) margin was used. WBI with simultaneous AxRT delivering $16 \times 2.66 \text{ Gy} = 42.56 \text{ Gy}$ was simulated for a conventional linear accelerator. Single-fraction RT boosts of 9 Gy, 11 Gy, and 13 Gy (ablative dose), with dose escalation within the PTV, were simulated for each LN using MRL treatment planning software. Addition of dose plans was performed voxel-by-voxel, after conversion of both dose plans into dose equivalent to 2-Gy fractions, in order to obtain total dose. In all plans, high target coverage was achieved, while additional OAR dose was limited or negligible and within all clinical constraints. Thus, LN boosting up to ablative RT dose is feasible in the MRL, regardless of LN location, additional to standard loco-regional RT. In selected breast-cancer patients this may lead to omission of axillary surgery, or reduction of conventional fractionated RT schedules, and possibly reduction of treatment-induced toxicity.

General discussion

Breast radiotherapy in a magnetic field

Compared to RT in conventional linacs, dosimetry of breast-RT treatments will change in the MRL under influence of the magnetic field. Due to the ERE, the skin dose can be raised significantly for WBI, for both a traditional tangential two-field set-up and a seven-field approach (**chapter 2**). Although detailed clinical data on high skin dose is unavailable, it can be associated with increased toxicity and impaired cosmetic results. This may be prohibitive for performing WBI treatments on the MRL. In contrast, magnetic-field-induced dosimetric effects for APBI treatments are negligible due to smaller target volumes which are usually located deeper under the skin surface. For local breast RT treatments performed on the MRL, the focus will therefore be on partial-breast techniques. Regional breast RT is most often performed simultaneously with local treatment by WBI. Similarly to WBI, unwanted skin dose increase is expected for standard regional RT due to the large fields and superficial target volumes. On the MRL, regional RT will therefore be performed on smaller targets compared to standard axillary target volumes, and which are less superficial. This may be achieved by the use of dedicated MRI scans that visualize individual axillary LNs (**chapters 4, 5, and 6**).

Magnetic-field effects on skin dose may vary for different hybrid MRI/RT designs. Both the Australian MRI-linac project and the Fallone group (Cross Cancer Institute, Edmonton, Alberta, Canada) have developed an MRI/RT system with a photon linac irradiating parallel through a split-bore MRI scanner [1,2]. In MRI/RT designs with parallel orientation, there is no ERE. However, an effect that becomes prominent is electron contamination, which can cause significant skin dose increase at the beam central axis on the entry side of the patient [3]. In the various hybrid MRI/RT systems that are in development, different magnetic-field strengths are employed, ranging from 0.2 T to 1.5 T [2,4–8]. As described in **chapter 2**, the ERE is expected to elevate the skin dose significantly at lower magnetic-field strength of 0.35 T in case of large radiation fields, e.g. in WBI and standard regional RT.

Before implementation of new breast RT techniques on hybrid MRI/RT modalities, dosimetry should be validated thoroughly in presence of the magnetic field.

Intra-fraction motion on the MRI-linac

The influence of intra-fraction motion in breast RT is increasingly important for accuracy in more sophisticated techniques. Local treatments on the MRL will be concentrated on partial-breast RT approaches (**chapter 2**) as described above. In breast RT, the two main sources of intra-fraction motion are respiration and whole-body displacements. Generally, breathing motion is not expected to have a strong influence on accuracy of partial-breast RT due to small amplitudes (**chapter 3**). Exceptionally large deviations, due to sudden in- and exhalation, can occur infrequently, and could lead to (temporary) target miss. A method for restricting respiratory motion is to use a breath-hold technique. However, due to increasing treatment durations, this will be infeasible. Large, permanent whole-body displacements over longer periods of time – up to 15 mm (**chapter 3**) – have a considerable impact on accuracy of APBI approaches, due to increasing fraction dose and increasing fraction durations. If the RT plan is not adequately adapted, this may lead to geometric miss of the target. This will result in an inadequate RT dose to the tumour and increased dose to the normal tissues. This has been shown for other tumour sites as well [9–12]. Whole-body displacements could be reduced by immobilizing the

patient. The use of various immobilization devices has been investigated, albeit with largely varying results [13–15].

In the *ABLATIVE* trial that is currently ongoing at UMC Utrecht, single-fraction APBI is performed on a conventional linac. In order to prevent target miss due to whole-body motion over longer periods of time, an additional CBCT scan is acquired halfway through the treatment, which is used to evaluate displacements that may have occurred.

On the MRL, daily set-up variations, i.e. anatomical differences between fractions, can be handled by pre-beam imaging, i.e. MRI acquisition before start of RT. For intra-fraction motion, other MRI-based methods can be employed. A strategy to account for movement due to deep in- and exhalation could be gating by use of MRI navigators [16,17]. As soon as the target moves out of a predefined window, dose delivery is suspended, until it moves back into the window, and irradiation is continued. This method has been shown to be feasible for renal tumours [18]. For whole-body shifts over longer treatment durations, a possible approach is an intermediate re-planning strategy. One or more additional anatomical MRI scan(s) are acquired during a fraction, similarly to the multi-minute motion analysis in **chapter 3**. The treatment plan is adapted according to these MRI scan(s), after which RT delivery is continued.

Since regional RT on the MRL will possibly be based on individual LNs (**chapters 4, 5, and 6**), target volumes are smaller compared to standard CT-based regional RT. Thus, analogously to APBI techniques, intra-fraction motion becomes increasingly relevant. Similarly, the impact of respiratory motion will be limited. More important for regional RT accuracy are permanent and/or irregular displacements over longer periods of time. In particular, the location of axillary LNs and surrounding structures is dependent on the position of the arms [19]. If the arms are not in a stable position, this could lead to geometric shifts of LNs and OARs during RT delivery. An on-line motion management strategy for regional RT on the MRL is in development in the *Towards implementation of on-line MRI-guided radiation therapy in breast cancer patients (TIMBRE, NLS6683.041.16)* study currently ongoing at UMC Utrecht.

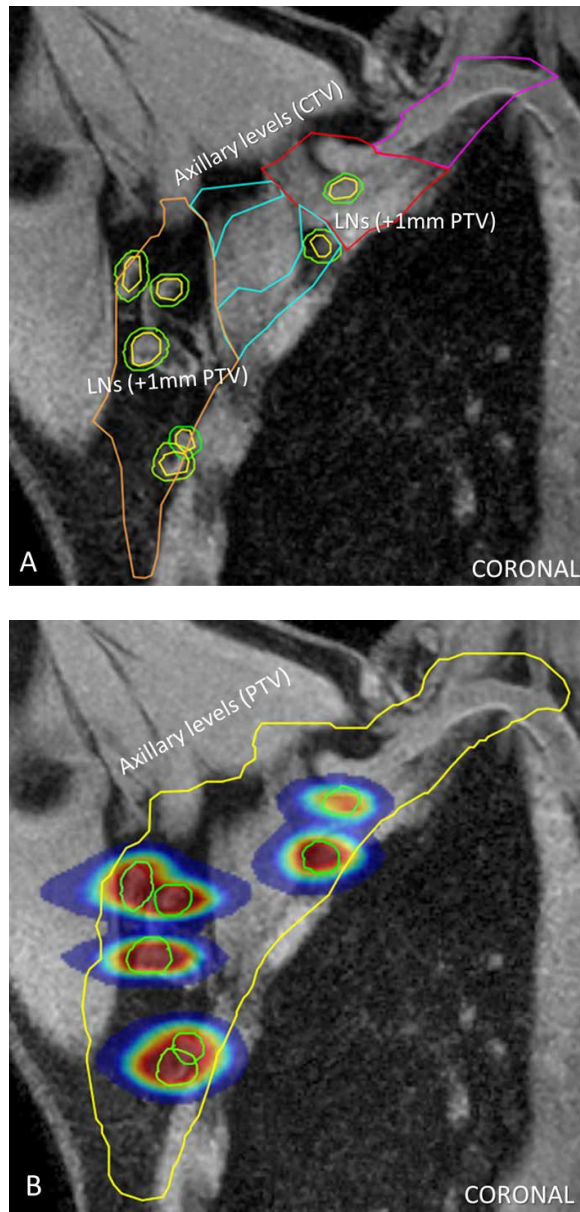
A more sophisticated method would be on-line target tracking and dynamic planning, performed during dose delivery on the MRL. The RT plan is adapted in (near) real-time, taking into account all types of motion, without requiring the dose delivery to be suspended. This ideally enables dose escalation in the target, while normal tissue is minimally compromised. While real-time plan adaptation on the MRL is still in development, recent results are very promising [20–25]. The added value for breast RT has to be investigated.

Another important issue to keep in mind when developing an on-line motion management strategy is that total fraction time is restricted due to supine posture endurance for undergoing MRI (**chapters 4 and 5**). Most breast-cancer patients are not able to maintain both arms in abduction for longer than 30 minutes, due to pain in the shoulders and arms. An alternate approach altogether is to perform local breast RT treatments in prone position. In general, prone positioning can result in less stability and increased movement during RT delivery [26–28]. However, this may be less relevant on the MRL due to on-line motion management. This is under investigation in the aforementioned *TIMBRE* trial. Patient endurance for a prone posture may be better than for the supine position. Due to a different anatomy in prone position compared to supine, dose to normal tissue, including the chest wall, lungs, and – especially for left-sided breast RT – to the heart and coronary arteries could change [29,30]. By direct visualization of these structures, MRI guidance may play a role in sparing of normal tissue for new RT treatments.

MRI-guided radiotherapy of individual lymph nodes

De-escalated lymph node based radiotherapy

Visualization of LNs with CT is generally limited. Therefore, conventional target delineation in regional RT is based on anatomical boundaries, and target volumes are consequently large. On the MRL, with MRI guidance (**chapters 4, 5 and 6**), an alternative approach to standard elective regional RT could be to concentrate irradiation more on individual LNs instead of entire axillary levels. Separate LNs delineated on MRI occupy at most 3% of the respective axillary levels (**chapter 5**). As an indication of adding uncertainty margins which are required in RT planning, all LN delineations were expanded (figure 1(A)). Even after an isotropic expansion of 5 mm,



● *Figure 1 Delineations on a coronal MRI scan (water-only image of mDixon water-fat separation, T1w spoiled gradient echo) from the MILANO patient study. In (A), standard axillary target volumes (CTV) are indicated in orange, blue, red, and purple. Individual lymph nodes (LNs) are delineated in yellow. The green indicates volumes after 1-mm expansion, which occupy considerably smaller volume than the axillary levels. In (B), the planning target volume (PTV) is indicated for the axillary levels (yellow), which is a 5-mm expansion of the CTVs. A dose plan is shown, where $16 \times 2.66 \text{ Gy} = 42.56 \text{ Gy}$ is delivered on the individual LN-based PTVs (green). The potential reduction of dose to healthy tissue on LN-based targets, compared to dose to standard regional target volumes, is apparent.*

the encompassing volume occupies at most half of the respective axillary level volumes. Thus, for RT treatments aimed at LN-based volumes, total target volume is considerably smaller than the standard regional targets. The MRL secures on-line LN visualization and facilitates target tracking, which minimizes any uncertainty margins. Moreover, direct identification and delineation of OARs is possible. As a result, dose can be delivered very precisely to the LNs, which can result in better sparing of normal tissue. In elective RT, a novel strategy could be a de-escalated approach, in which the dose prescribed to the axillary levels is lowered everywhere, except to the individual LNs. A step further would be to limit dose delivery to only the LNs (figure 1(B)). Thus, on-line MRI guidance may result in a highly personalized target volume, leading to lower integral dose, optimal sparing of healthy tissue, and possibly reduced toxicity. Both steps in this process should be investigated further in clinical studies.

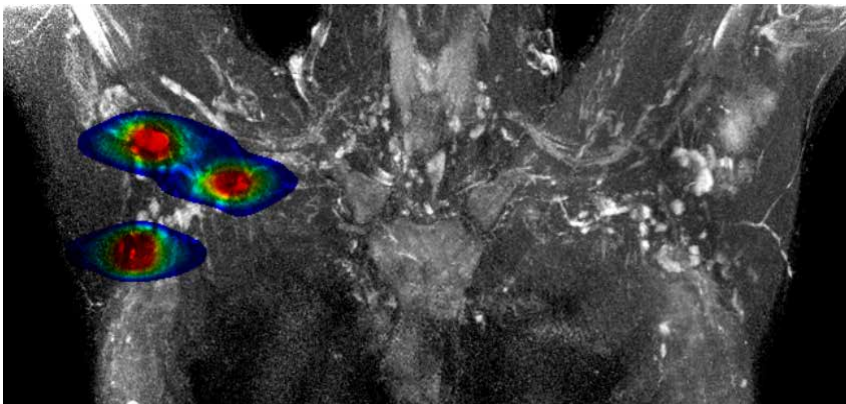
Our work (chapters 4 and 5) showed the feasibility of imaging LNs for RT planning. Accuracy of LN detection remains an issue, since there is no gold standard *in vivo* available. Furthermore, the inter-human variation of numbers and locations of LNs is large [19]. Axillary LN numbers can range between 6 and 45, and between 1 and 10 in the supraclavicular region [31–38]. The *ex-vivo* gold standard is histopathology, but information on LNs in all axillary regions is generally unavailable. In order to assess sensitivity for LN detection, MRI could be performed in cadavers, and subsequently correlated with histopathological information. However, exact numbers of LNs in actual patients will still be uncertain. In our study, numbers of regional LNs detected on MRI were within the expected ranges, and LN detection was highly reproducible. We used information from several MRI techniques that were complementary on several aspects, including contrast of LNs and presence of anatomical reference structures, and this was validated by a multidisciplinary team of observers. Even minute LNs were identified this way. It may therefore be feasible to investigate the effectiveness of MRI-guided LN-based RT treatments.

Indication for current elective RT treatments is determined by results from clinical studies investigating locations of regional recurrences [39]. Delineation guidelines used for regional RT are based on this [40–43]. The MRI techniques presented in this thesis aimed at the highest LN detection rate in the axillary regions, but the question remains whether all LNs

should receive radiation dose. Axillary LNs are connected by an intricate network of lymphatic vessels that ensure transport of lymphatic fluid from one LN to the other. With the explicit visualization of the vessels it may be possible to establish – on an individual level – which LNs have higher (or lower) risk for regional recurrence. This may further aid in the target definition for LN-based RT techniques.

Single-fraction radiotherapy of tumour-positive lymph nodes

Due to on-line visualization of LNs and surrounding OARs, RT dose escalation of involved LNs can be explored instead of axillary surgery or conventionally fractionated regional RT boost. Due to minimized uncertainty margins, even a single-fraction high dose (boost) on tumour-positive LNs may be achievable on the MRL. A first step is to deliver a boost dose to a single LN, additional to conventional loco-regional RT. **Chapter 6** showed that regardless of LN location, an additional LN boost is dosimetrically feasible, up to ablative dose (1 x 13 Gy prescription). This type of treatments could serve as a non-invasive alternative to ALND or a sequential fractionated boost for patients with tumour-positive LNs, both of which are associated with increased toxicity and patient burden [44–46]. An ablative LN boost can lead to omission of axillary surgery, reduction in number of RT fractionations, decreased risk of treatment-induced toxicity, and thereby a better quality of life for the patient. This opens the way to more elaborate boost set-ups on the MRL, such as an ablative boost to several LNs simultaneously (figure 2), and boost RT techniques performed before any axillary surgery.



● *Figure 2 Simulation of a simultaneous boost delivery on several LNs on the MRL.*

For novel RT treatments of tumour-positive LNs, the ability to distinguish malignant from benign LNs will be essential. LN staging could be performed pre-treatment, which does not necessarily require MRI. With pre-beam MRI acquisition, the LNs of interest could then be identified, e.g. using on-line image registration. Ultimately, the goal would be to stage the LNs on-line, using MRI. However, MRI sequences presented in **chapters 4 and 5** were not optimized for LN staging, and current diagnostic MRI techniques show varying specificity/sensitivity for LN staging [31,47–51]. Therefore, other methods for LN staging are required, with a very high sensitivity and specificity. The most promising results have been obtained with ultra-small super-paramagnetic iron oxide (USPIO)-enhanced T2*-weighted imaging, in combination with T1w/T2w MRI sequences [52]. Another method to accurately stage LNs is to merge MRI with PET scans [53].

MRI guidance for current clinical practice

MRI guidance may improve accuracy of the standard RT target definition on CT. Significantly more axillary LNs are identified on MRI than on RT-planning CT (**chapter 5**). If fused with CT, MRI could provide anatomical information on exact LN locations, in relation to surrounding anatomical structures. In current RT planning this knowledge may lead to adaptation of standard targets, such that more normal tissue can be spared. The added value of MRI to CT in RT planning is an important topic of further clinical investigation. For patients who currently receive a sequential fractionated RT boost [46,54,55], target delineation is performed on RT-planning CT. If a fludeoxyglucose (FDG)-PET/CT scan is performed, it is merged with the RT-planning CT. Addition of dedicated MRI scans in the current contouring process may further improve the target definition. This is under investigation in the aforementioned *TIMBRE* patient study at UMC Utrecht.

A drawback is that registering MRI with CT induces extra uncertainties and registration errors. As a consequence, treated volumes will increase. On-line MRI guidance, with minimal uncertainty margins, may be required to ensure accurate and safe dose delivery for new RT techniques, particularly with high fraction doses.

Concluding remarks

The MRL is a potentially powerful treatment modality that offers on-line target visualization in close relation to the surrounding healthy structures. When combined with methods accounting for intra-fraction motion, a new range of RT techniques is achievable. As a next step towards a *dose painted* scenario, novel MRI-guided RT will focus on the primary tumour and individual LNs, with increasing target dose, and in fewer fractions. MRI methods for explicit LN visualization, presented in this thesis, can facilitate LN-based RT as an alternative to current regional RT. Due to significantly smaller targets, this will result in optimal sparing of healthy tissue and toxicity reduction, and a better quality of life. Patients with tumour-positive LNs can be treated with an additional single-fraction ablative LN boost. In the future, MRL-based RT may fully or partly replace currently standard local and regional treatments. Examples of this are a very high dose to the primary tumour, or an ablative RT boost to tumour-positive LNs. Ideally these are performed in a single fraction, all without the need of any surgery. This way, the MRL could provide highly efficient and minimally invasive treatments for breast-cancer patients.

References

- [1] Keall PJ, Barton M, Crozier S, Australian MRI-Linac Program, including contributors from Ingham Institute, Illawarra Cancer Care Centre, Liverpool Hospital, Stanford University, Universities of Newcastle, Queensland, Sydney, Western Sydney, and Wollongong. The Australian magnetic resonance imaging-linac program. *Semin Radiat Oncol* 2014;24:203–6. doi:10.1016/j.semradonc.2014.02.015.
- [2] Fallone BG. The rotating biplanar linac-magnetic resonance imaging system. *Semin Radiat Oncol* 2014;24:200–2. doi:10.1016/j.semradonc.2014.02.011.
- [3] Oborn BM, Metcalfe PE, Butson MJ, Rosenfeld AB, Keall PJ. Electron contamination modeling and skin dose in 6 MV longitudinal field MRIgRT: Impact of the MRI and MRI fringe field. *Med Phys* 2012;39:874–90. doi:10.1118/1.3676181.
- [4] Fallone BG, Murray B, Rathee S, Stanescu T, Steciw S, Vidakovic S, et al. First MR images obtained during megavoltage photon irradiation from a prototype integrated linac-MR system. *Med Phys* 2009;36:2084–8.
- [5] Keall PJ, Barton M, Crozier S. The Australian Magnetic Resonance Imaging-Linac Program. *Semin Radiat Oncol* 2014;24:203–6.
- [6] Lagendijk JJW, Raaymakers BW, Raaijmakers AJE, Overweg J, Brown KJ, Kerkhof EM, et al. MRI/linac integration. *Radiother Oncol* 2008;86:25–9. doi:10.1016/j.radonc.2007.10.034.
- [7] Lagendijk JJW, van Vulpen M, Raaymakers BW. The development of the MRI linac system for online MRI-guided radiotherapy: a clinical update. *J Intern Med* 2016;280:203–8. doi:10.1111/joim.12516.
- [8] Mutic S, Dempsey JF. The ViewRay system: magnetic resonance-guided and controlled radiotherapy. *Semin Radiat Oncol* 2014;24:196–9. doi:10.1016/j.semradonc.2014.02.008.
- [9] Josipovic M, Persson GF, Logadottir A, Smulders B, Westmann G, Bangsgaard JP. Translational and rotational intra- and inter-fractional errors in patient and target position during a short course of frameless stereotactic body radiotherapy. *Acta Oncol* 2012;51:610–7. doi:10.3109/0284186X.2011.626448.
- [10] Schippers MGA, Bol GH, de Leeuw AAC, van der Heide UA, Raaymakers BW, Verkooijen HM, et al. Position shifts and volume changes of pelvic and para-aortic nodes during IMRT for patients with cervical cancer. *Radiother Oncol* 2014;111:442–5. doi:10.1016/j.radonc.2014.05.013.
- [11] Navarro-Martin A, Cacicedo J, Leaman O, Sancho I, García E, Navarro V, et al. Comparative analysis of thermoplastic masks versus vacuum cushions in stereotactic body radiotherapy. *Radiat Oncol* 2015;10:176. doi:10.1186/s13014-015-0484-7.
- [12] Fatunase T, Wang Z, Yoo S, Hubbs JL, Prosnitz RG, Yin F-F, et al. Assessment of the residual error in soft tissue setup in patients undergoing partial breast irradiation: results of a prospective study using cone-beam computed tomography. *Int J Radiat Oncol Biol Phys* 2008;70:1025–34. doi:10.1016/j.ijrobp.2007.07.2344.
- [13] Mitine C, Dutreix A, van der Schueren E. Tangential breast irradiation: influence of technique of set-up on transfer errors and reproducibility. *Radiother Oncol* 1991;22:308–10.
- [14] Thilmann C, Adamietz IA, Saran F, Mose S, Kostka A, Böttcher H. The Use of a Standardized Positioning Support Cushion During Daily Routine of Breast Irradiation. *Int J Radiat Oncol* 1998;41:459–63. doi:10.1016/S0360-3016(98)00022-4.

- [15] Nalder CA, Bidmead AM, Mubata CD, Tait D, Beardmore C. Influence of a vac-fix immobilization device on the accuracy of patient positioning during routine breast radiotherapy. *Br J Radiol* 2001;74:249–54. doi:10.1259/bjr.74.879.740249.
- [16] Ehman RL, Felmlee JP. Adaptive technique for high-definition MR imaging of moving structures. *Radiology* 1989;173:255–63. doi:10.1148/radiology.173.1.2781017.
- [17] Crijns SPM, Kok JGM, Lagendijk JJW, Raaymakers BW. Towards MRI-guided linear accelerator control: gating on an MRI accelerator. *Phys Med Biol* 2011;56:4815–25. doi:10.1088/0031-9155/56/15/012.
- [18] Stam MK, van Vulpen M, Barendrecht MM, Zonnenberg BA, Crijns SPM, Lagendijk JJW, et al. Dosimetric feasibility of MRI-guided external beam radiotherapy of the kidney. *Phys Med Biol* 2013;58:4933–41. doi:10.1088/0031-9155/58/14/4933.
- [19] Dijkema IM, Hofman P, Raaijmakers CPJ, Lagendijk JJ, Battermann JJ, Hillen B. Loco-regional conformal radiotherapy of the breast: delineation of the regional lymph node clinical target volumes in treatment position. *Radiother Oncol* 2004;71:287–95. doi:10.1016/j.radonc.2004.02.017.
- [20] Glitzner M, Crijns SPM, de Senneville BD, Kontaxis C, Prins FM, Lagendijk JJW, et al. On-line MR imaging for dose validation of abdominal radiotherapy. *Phys Med Biol* 2015;60:8869–83. doi:10.1088/0031-9155/60/22/8869.
- [21] Kontaxis C, Bol GH, Lagendijk JJW, Raaymakers BW. Towards adaptive IMRT sequencing for the MR-linac. *Phys Med Biol* 2015;60:2493–509. doi:10.1088/0031-9155/60/6/2493.
- [22] Bjerre T, Crijns S, af Rosenschöld PM, Aznar M, Specht L, Larsen R, et al. Three-dimensional MRI-linac intra-fraction guidance using multiple orthogonal cine-MRI planes. *Phys Med Biol* 2013;58:4943–50. doi:10.1088/0031-9155/58/14/4943.
- [23] Glitzner M, Crijns SPM, de Senneville BD, Lagendijk JJW, Raaymakers BW. On the suitability of Elekta's Agility 160 MLC for tracked radiation delivery: closed-loop machine performance. *Phys Med Biol* 2015;60:2005–17. doi:10.1088/0031-9155/60/5/2005.
- [24] Crijns SPM, Raaymakers BW, Lagendijk JJW. Proof of concept of MRI-guided tracked radiation delivery: tracking one-dimensional motion. *Phys Med Biol* 2012;57:7863–72. doi:10.1088/0031-9155/57/23/7863.
- [25] Glitzner M, de Senneville BD, Lagendijk JJW, Raaymakers BW, Crijns SPM. On-line 3D motion estimation using low resolution MRI. *Phys Med Biol* 2015;60:N301–10. doi:10.1088/0031-9155/60/16/N301.
- [26] Kirby AM, Evans PM, Donovan EM, Convery HM, Haviland JS, Yarnold JR. Prone versus supine positioning for whole and partial-breast radiotherapy: a comparison of non-target tissue dosimetry. *Radiother Oncol* 2010;96:178–84. doi:10.1016/j.radonc.2010.05.014.
- [27] Kirby AM, Evans PM, Helyer SJ, Donovan EM, Convery HM, Yarnold JR. A randomised trial of supine versus prone breast radiotherapy (SuPr study): comparing set-up errors and respiratory motion. *Radiother Oncol* 2011;100:221–6. doi:10.1016/j.radonc.2010.11.005.
- [28] Veldeman L, De Gerssem W, Speleers B, Truyens B, Van Greveling A, Van den Broecke R, et al. Alternated prone and supine whole-breast irradiation using IMRT: setup precision, respiratory movement and treatment time. *Int J Radiat Oncol Biol Phys* 2012;82:2055–64. doi:10.1016/j.ijrobp.2010.10.070.
- [29] Lakosi F, Gulyban A, Janvary L, Simoni SB-M, Jansen N, Seidel L, et al. Respiratory Motion, Anterior Heart Displacement and Heart Dosimetry: Comparison Between Prone (Pr) and Supine (Su) Whole Breast Irradiation. *Pathol Oncol Res* 2015;21:1051–8. doi:10.1007/s12253-015-9932-9.

- [30] Würschmidt F, Stoltenberg S, Kretschmer M, Petersen C. Incidental dose to coronary arteries is higher in prone than in supine whole breast irradiation. A dosimetric comparison in adjuvant radiotherapy of early stage breast cancer. *Strahlentherapie Und Onkol Organ Der Dtsch Röntgengesellschaft*. [et Al] 2014;190:563–8. doi:10.1007/s00066-014-0606-4.
- [31] Luciani A, Pigneur F, Ghozali F, Dao T-H, Cunin P, Meyblum E, et al. Ex vivo MRI of axillary lymph nodes in breast cancer. *Eur J Radiol* 2009;69:59–66. doi:10.1016/j.ejrad.2008.07.040.
- [32] MacDonald SM, Harisinghani MG, Katkar A, Napolitano B, Wolfgang J, Taghian AG. Nanoparticle-enhanced MRI to evaluate radiation delivery to the regional lymphatics for patients with breast cancer. *Int J Radiat Oncol Biol Phys* 2010;77:1098–104. doi:10.1016/j.ijrobp.2009.06.002.
- [33] Korteweg MA, Zwanenburg JJM, van Diest PJ, van den Bosch MAAJ, Luijten PR, van Hillegersberg R, et al. Characterization of ex vivo healthy human axillary lymph nodes with high resolution 7 Tesla MRI. *Eur Radiol* 2011;21:310–7. doi:10.1007/s00330-010-1915-3.
- [34] Korteweg MA, Zwanenburg JJM, Hoogduin JM, van den Bosch MAAJ, van Diest PJ, van Hillegersberg R, et al. Dissected sentinel lymph nodes of breast cancer patients: characterization with high-spatial-resolution 7-T MR imaging. *Radiology* 2011;261:127–35. doi:10.1148/radiol.11103535.
- [35] Jiang J, He Q, Yang X, Liang Y, Fan L, Zhang Y, et al. Contribution of minute axillary lymph nodes to accurate staging for patients with breast cancer. *Chin Med J (Engl)* 2007;120:1762–5.
- [36] Nakai G, Matsuki M, Harada T, Tanigawa N, Yamada T, Barentsz J, et al. Evaluation of axillary lymph nodes by diffusion-weighted MRI using ultrasmall superparamagnetic iron oxide in patients with breast cancer: initial clinical experience. *J Magn Reson Imaging* 2011;34:557–62. doi:10.1002/jmri.22651.
- [37] Ying M, Ahuja A. Sonography of Neck Lymph Nodes. Part I: Normal Lymph Nodes. *Clin Radiol* 2003;58:351–8. doi:10.1016/S0009-9260(02)00584-6.
- [38] Baltzer PAT, Dietzel M, Burmeister HP, Zoubi R, Gajda M, Camara O, et al. Application of MR mammography beyond local staging: is there a potential to accurately assess axillary lymph nodes? evaluation of an extended protocol in an initial prospective study. *AJR Am J Roentgenol* 2011;196:W641–7. doi:10.2214/AJR.10.4889.
- [39] Offersen BV, Nielsen HM, Overgaard M, Overgaard J. Is regional nodes radiotherapy an alternative to surgery? *Breast* 2013;22 Suppl 2:S118–28. doi:10.1016/j.breast.2013.07.023.
- [40] Offersen B V, Boersma LJ, Kirkove C, Hol S, Aznar MC, Biete Sola A, et al. ESTRO consensus guideline on target volume delineation for elective radiation therapy of early stage breast cancer. *Radiother Oncol* 2015;114:3–10. doi:10.1016/j.radonc.2014.11.030.
- [41] Verhoeven K, Weltens C, Remouchamps V, Mahjoubi K, Veldeman L, Lengele B, et al. Vessel based delineation guidelines for the elective lymph node regions in breast cancer radiation therapy - PROCAB guidelines. *Radiother Oncol* 2015;114:11–6. doi:10.1016/j.radonc.2014.11.008.
- [42] Nielsen MH, Berg M, Pedersen AN, Andersen K, Glavicic V, Jakobsen EH, et al. Delineation of target volumes and organs at risk in adjuvant radiotherapy of early breast cancer: national guidelines and contouring atlas by the Danish Breast Cancer Cooperative Group. *Acta Oncol* 2013;52:703–10. doi:10.3109/0284186X.2013.765064.
- [43] Gentile MS, Usman AA, Neuschler EI, Sathiaseelan V, Hayes JP, Small W. Contouring Guidelines for the Axillary Lymph Nodes for the Delivery of Radiation Therapy in Breast Cancer: Evaluation of the RTOG Breast Cancer Atlas. *Int J Radiat Oncol* 2015;93:257–65. doi:10.1016/j.ijrobp.2015.07.002.

- [44] Ivens D, Hoe AL, Podd TJ, Hamilton CR, Taylor I, Royle GT. Assessment of morbidity from complete axillary dissection. *Br J Cancer* 1992;66:136–8.
- [45] Kakuda JT, Stuntz M, Trivedi V, Klein SR, Vargas HI. Objective assessment of axillary morbidity in breast cancer treatment. *Am Surg* 1999;65:995–8.
- [46] Chandra RA, Miller CL, Skolny MN, Warren LEG, Horick N, Jammallo LS, et al. Radiation therapy risk factors for development of lymphedema in patients treated with regional lymph node irradiation for breast cancer. *Int J Radiat Oncol Biol Phys* 2015;91:760–4. doi:10.1016/j.ijrobp.2014.12.029.
- [47] Harnan SE, Cooper KL, Meng Y, Ward SE, Fitzgerald P, Papaioannou D, et al. Magnetic resonance for assessment of axillary lymph node status in early breast cancer: a systematic review and meta-analysis. *Eur J Surg Oncol* 2011;37:928–36. doi:10.1016/j.ejso.2011.07.007.
- [48] He N, Xie C, Wei W, Pan C, Wang W, Lv N, et al. A new, preoperative, MRI-based scoring system for diagnosing malignant axillary lymph nodes in women evaluated for breast cancer. *Eur J Radiol* 2012;81:2602–12. doi:10.1016/j.ejrad.2012.03.019.
- [49] de Felice C, Cipolla V, Stagnitti A, Porfiri LM, Guerrieri D, Musella A, et al. Diagnostic accuracy of 1.5 Tesla breast magnetic resonance imaging in the pre-operative assessment of axillary lymph nodes. *Eur J Gynaecol Oncol* 2015;36:447–51.
- [50] Arslan G, Altintoprak KM, Yirgin IK, Atasoy MM, Celik L. Diagnostic accuracy of metastatic axillary lymph nodes in breast MRI. *Springerplus* 2016;5:735. doi:10.1186/s40064-016-2419-7.
- [51] Chung J, Youk JH, Kim J-A, Gweon HM, Kim E-K, Ryu YH, et al. Role of diffusion-weighted MRI: predicting axillary lymph node metastases in breast cancer. *Acta Radiol* 2014;55:909–16. doi:10.1177/0284185113509094.
- [52] Harnan SE, Cooper KL, Meng Y, Ward SE, Fitzgerald P, Papaioannou D, et al. Magnetic resonance for assessment of axillary lymph node status in early breast cancer: A systematic review and meta-analysis. *Eur J Surg Oncol* 2011;37:928–36.
- [53] Cooper KL, Meng Y, Harnan S, Ward SE, Fitzgerald P, Papaioannou D, et al. Positron emission tomography (PET) and magnetic resonance imaging (MRI) for the assessment of axillary lymph node metastases in early breast cancer: systematic review and economic evaluation. *Health Technol Assess* 2011;15:iii – iv, 1–134. doi:10.3310/hta15040.
- [54] Wang X, Yu TK, Salehpour M, Zhang SX, Sun TL, Buchholz T a. Breast cancer regional radiation fields for supraclavicular and axillary lymph node treatment: is a posterior axillary boost field technique optimal? *Int J Radiat Oncol Biol Phys* 2009;74:86–91. doi:10.1016/j.ijrobp.2008.07.016.
- [55] Hernandez V, Arenas M, Müller K, Gomez D, Bonet M. An optimized posterior axillary boost technique in radiation therapy to supraclavicular and axillary lymph nodes: A comparative study. *Med Dosim* 2013;38:413–7. doi:10.1016/j.meddos.2013.05.003.

“Nothing shocks me. I’m a scientist.”

Indiana Jones



Addenda

Addendum

Samenvatting

De MRI-linac (MRL), die is ontwikkeld in het UMC Utrecht, maakt het mogelijk om zeer precieze en gelokaliseerde radiotherapiebehandelingen uit te voeren. Dit gebeurt aan de hand van MRI-geleiding, *terwijl* de patiënt op de behandelafel ligt. Dit proefschrift beschrijft voorbereidend werk voor de implementatie van zowel lokale als regionale radiotherapie (RT) voor patiënten met borstkanker op de MRL.

Hoofdstukken 2 en 3 beschrijven belangrijke fysische aspecten voor lokale RT van de borst, d.w.z. hele-borstbestraling (*whole-breast irradiation*, WBI), en versnelde partiële-borstbestraling (*accelerated partial breast irradiation*, APBI). Het magnetisch veld in de MRL heeft invloed op de dosisverdeling door de Lorentz-kracht die loodrecht werkt op bewegende elektronen. De effecten hiervan zijn het meest prominent rond weefselovergangen met sterke dichtheidsverschillen, zoals de overgang tussen lucht en huid, wat kan leiden tot een verhoogde huiddosis. De gevolgen voor RT-behandelingen van borstkanker kunnen hierdoor aanzienlijk zijn.

In **hoofdstuk 2** wordt een planningstudie voor een RT-behandeling beschreven. Deze is gedaan aan de hand van computed tomography (CT)-scans van 10 vroegstadium borstkankerpatiënten. Deze patiënten werden gescand in rugligging met beide armen omhoog - analoog aan de positionering voor RT-behandeling- en na borstsparende chirurgie (BSC). De doelvolumina en belangrijke risico-organen, of *organs-at-risk* (OAR's), zijn daarna ingetekend, waaronder de huid, die specifiek gedefinieerd is als de eerste 5 mm vanaf het huidoppervlak. Drie RT-scenario's zijn onderzocht: een traditionele WBI-benadering (16 x 2.66 Gy) met twee schampvelden, een WBI-benadering met zeven velden (16 x 2.66 Gy), en een APBI-scenario, ook met zeven stralingsvelden (10 x 3.85 Gy). Hiervoor is speciaal ontwikkelde software voor RT-behandelingen gebruikt. De software houdt rekening met de specifieke aspecten van de MRL, waaronder het 1.5-T magnetisch veld, het vaste isocentrum, en de veldafmetingen. De dosis is berekend bij magnetische veldsterkten van zowel 0 T, 0.35 T, als 1.5 T. In beide WBI-benaderingen nam de huiddosis significant toe in aanwezigheid van een magnetisch veld. Dit is een potentieel nadeel want een hoge huiddosis kan tot bijwerkingen leiden. Voor de APBI-benadering waren er, in tegenstelling tot de WBI-situaties, geen significante effecten te zien door het magnetisch veld. Dit biedt daarom mogelijkheden voor MRI-geleide APBI-benaderingen in de MRL.

Voor veilige en effectieve APBI-behandelingen in de MRL wordt de invloed van intrafractiebeweging, d.w.z. beweging *gedurende* het afgeven van de dosis, steeds relevanter. Doelgebieden worden immers kleiner en daarmee wordt het (gedeeltelijk) missen van het doel steeds waarschijnlijker. Met MRI is de intrafractiebeweging in kaart gebracht voor borst-RT. Dit staat beschreven in **hoofdstuk 3**. De analyse is verricht op scans van 21 vroegstadium borstkankerpatiënten die gescand zijn zowel voor als na BSC, in rugligging en met beide armen omhoog. Om de effecten van ademhaling en lichaamsverplaatsingen te bepalen, is de intrafractiebeweging berekend over twee tijdschalen. Hiervoor zijn hoog-temporele, tweedimensionale (2D) cinematische MRI (cine-MRI) – elke 0.3 s opgenomen gedurende 2 min – en laag-temporele 3D MRI-scans gemaakt, geacquireerd over 20 min. Beweging op een subseconde-tijdschaal, gedurende 2 min, was over het algemeen regelmatig, en de amplitude bleef beperkt tot een mediaan van 2 mm. Verder kwamen grote, maar tijdelijke afwijkingen (tot 13 mm), slechts sporadisch voor. Deze werden geïnduceerd door diepe ademhaling. Beweging over een langere periode varieerde meer, maar de mediane amplitude bleef beperkt tot 2.2 mm. Grote lichaamsverplaatsingen (tot 15 mm gedurende 19 min) waren ook zichtbaar, maar dit gebeurde niet vaak. Voor en na BSC was er geen verschil tussen bewegingswaarden, op beide tijdschalen. Aangezien de focus voor de MRL zal liggen op nieuwe (potentieel ablatieve) technieken (zoals in **hoofdstuk 6** te lezen valt), met een hoge fractioneringsdosis, zal de behandelingstijd omhoog gaan. Intrafractiebeweging zou adequate RT kunnen beïnvloeden voor lange behandelingsduren. Het is dus noodzakelijk dat een strategie wordt ontwikkeld op de MRL om rekening te houden met beweging.

In **hoofdstukken 4, 5, en 6** wordt MRI-geleide RT van regionale lymfeklieren beschreven. Voor huidige regionale RT-behandelingen bij borstkankerpatiënten worden de doelvolumina op CT-scans ingetekend aan de hand van anatomische grenzen. MRI kan voor een meer accurate definitie van het doelvolume zorgen. Met MRI zouden de klieren *direct* kunnen worden afgebeeld, samen met de omliggende OAR's. We hebben verschillende MRI-methoden ontwikkeld voor regionale RT-planning, zoals **hoofdstuk 4** laat zien. MRI is eerst geoptimaliseerd in tien gezonde vrouwelijke vrijwilligers, en daarna geëvalueerd in nog eens twaalf vrijwilligers. De methoden bestonden uit een T1-gewogen (T1w), drie T2-gewogen (T2w), en een diffusie-gewogen MRI (DWI)-techniek. De scans

zijn kwalitatief beoordeeld op een aantal aspecten, gelet op de geschiktheid voor gebruik in regionale RT-planning. Daarnaast is een kwantitatieve evaluatie gedaan, door het aantal lymfeklieren per scan en per vrijwilligster te tellen. Twee T2w *fast spin echo* (FSE)-methoden lieten het hoogste aantal klieren zien (mediaan 24 okselklieren, $p < 0.05$ vergeleken met de andere drie methoden), alsook een hoog contrast van de lymfeklieren, uitstekende vetsuppressie, en ongevoeligheid voor beweging gedurende scanacquisitie. De derde T2w-sequentie, alsook DWI, liet aanzienlijk minder klieren zien (14, 10 in de oksel, resp.). Beiden waren ongeschikt voor regionale RT-planning door een hoge bewegingsgevoeligheid tijdens het scannen en geometrische verstoringen. Op de T1w MRI-scan vonden we dan weer iets meer klieren (17 in de oksel). De T1w methode bevatte waardevolle anatomische informatie, maar het contrast tussen klieren en omliggende weefsels bleek laag. De twee T2w FSE-technieken en de T1w MRI-techniek zouden, door hun complementaire eigenschappen, uitstekend kunnen helpen bij het visualiseren van afzonderlijke lymfeklieren in regionale RT-planning.

Zowel de anatomie als het uithoudingsvermogen voor MRI kan bij patiënten verschillen ten opzichte van gezonde vrijwilligsters (**hoofdstuk 4**). Chirurgische ingrepen in de oksel, zoals de schildwachtklierprocedure (SWKP), kunnen de anatomie en het uithoudingsvermogen voor een MRI-sessie ook aantasten. Bovenal is reproduceerbaarheid van het detecteren van afzonderlijke lymfeklieren met deze MRI-methoden van groot belang voor regionale RT-planning. Om deze redenen hebben we de haalbaarheid van MRI in patiënten onderzocht in de *MILANO* patiëntenstudie (NL50046.041.14). In deze studie hebben we 23 cTis-2N0M0 borstkankerpatiënten gescand, zowel voor als na BSC, met SWKP, zoals beschreven in **hoofdstuk 5**. Op beide momenten is MRI in rugligging gemaakt. De standaard plannings-CT na de operatie werd ook gemaakt. Het uithoudingsvermogen om MRI te ondergaan was goed, en voor/na de operatie was daar geen verschil in. De afzonderlijke klieren en andere structuren zijn door een multidisciplinair team geïdentificeerd op MRI-scans van zowel voor als na de SWKP, alsook op de postoperatieve plannings-CT. Hoewel er postoperatieve effecten zichtbaar waren op MRI (mediaan 26 lymfeklieren), waren de aantallen klieren zeer reproduceerbaar ($p = 1.00$) ten opzichte van de preoperatieve aantallen, daarbij rekening houdend met het aantal geëxcideerde lymfeklieren tijdens

de SWKP. Detectie van lymfeklieren was significant hoger met MRI dan met CT (mediaan van 11, $p < 0.001$). Het merendeel van de lymfeklieren, inclusief alle 33 schildwachtklieren, bevond zich in axillair level I. Per patiënt bevonden zich maximaal 8 lymfeklieren buiten de standaard axillaire contouren (binnen 5 mm daarvan). Verder hebben we bestudeerd hoeveel het regionale doelvolumen potentieel kan afnemen, op basis van de afzonderlijke klieren. De volumina van intekeningen, als men kijkt naar individuele klieren, bleken aanzienlijk kleiner dan de standaard axillaire intekeningen (maximaal 3% per axillair level), zelfs na 5-mm uitbreiding per klier (maximaal 46% per axillair level). We concluderen aan de hand van deze resultaten dat MRI van regionale lymfeklieren haalbaar en reproduceerbaar is, voor en na SWKP. Dit kan in de toekomst leiden tot MRI-gestuurde RT-strategieën gericht op individuele klieren, en met potentiaal aanzienlijk minder bestraald volume dan bij huidige regionale RT-benaderingen.

Gebruik van MRI-technieken zoals beschreven in **hoofdstukken 4 en 5** zouden verder kunnen leiden tot alternatieve behandelingen voor borstkankerpatiënten, bijvoorbeeld de groep met tumorpositieve lymfeklieren. In **hoofdstuk 6** beschrijven we een planning van een RT-behandeling waarbij het doel was om in één fractie een hoge dosis op afzonderlijke klieren te geven (boost), bovenop conventionele locoregionale RT – bestaande uit WBI en axillaire RT (AxRT). Hierbij hebben we gekozen voor een sequentiële benadering, omdat grote velden op de MRL zouden kunnen leiden tot een hogere huiddosis (**hoofdstuk 2**). Hiervoor hebben we scans van vijf *MILANO*-patiënten gebruikt voor intekening van de axillaire levels, de hele borst, en OAR's. De OAR's bestonden uit de brachiale plexus, het hart, de slokdarm, de luchtpijp, de longen, en de borstwand. Per patiënt werden vier verschillende lymfeklieren uitgekozen, met variërende locaties in de vier axillaire gebieden. Deze zijn vervolgens ingetekend, met een *planning target volume* (PTV)-marge van 2 mm. Vervolgens hebben we WBI met gelijktijdige AxRT, met een fractionering van $16 \times 2.66 \text{ Gy} = 42.56 \text{ Gy}$, gesimuleerd voor een conventionele lineaire versneller. Met behulp van speciale MRL-software hebben we los daarvan simulaties gedaan voor boosts van 9 Gy, 11 Gy, en 13 Gy (ablatief), met een toegestane dosisescalatie in het PTV. De boostplannen en de bijbehorende WBI/AxRT-plannen zijn daarna voxel voor voxel opgeteld, nadat eerst beide plannen waren omgezet naar dosis in 2-Gy-fracties (EQD₂). Voor

alle plannen was de dekking van de dosis in het PTV van de boost hoog, terwijl de extra dosis op OAR's beperkt bleef of zelfs verwaarloosbaar klein. Hieruit concluderen we dat het extra boosten van lymfeklieren – bovenop locoregionale RT – tot zelfs ablatieve RT-dosis, haalbaar is in de MRL. Dit is ongeacht de locatie van de boost. Voor geselecteerde borstkankerpatiënten zou dit in de toekomst kunnen leiden tot het weglaten van een chirurgische ingreep in de oksel, of een verkorting van huidige gefractioneerde RT-schema's. Verder kan dit mogelijk tot verlaging van de toxiciteit door huidige behandeling leiden.

Addendum

Dankwoord

Eindelijk de ruimte om iedereen die mij geholpen heeft de afgelopen vijf jaar te bedanken! *Was ich noch zu sagen hätte, dauert eine Zigarette...*

Allereerst mijn promotor: Jan, dank je wel voor je onmisbare input. Jouw onverzettelijke geloof in de MR-linac, en je eigen(wijze) visie op het vakgebied – dat natuurlijk niet meer zonder MRI kan – werkt enorm inspirerend. Het doet me een genoegen aan het MR-linac-project te hebben bijgedragen. Nu alleen die lymph vessels nog...

Ten tweede gaat mijn dank uit naar mijn begeleiders: Bram, Desirée en Mariëlle. Ik kijk met trots terug op wat we bereikt hebben de afgelopen vijf jaar. Bram, dank je wel voor alle (sub)wekelijkse overleggen over een weer eens herschreven manuscript, of gewoon over wat we nu weer in het weekend hebben gedaan. Onze samenwerking vond ik erg prettig! Desirée, bedankt voor onze goede samenwerking gedurende de jaren en je input vanuit klinisch oogpunt, waar ik heel veel van heb geleerd. Ik sta vaak versteld van je parate kennis over relevante literatuur en lopende onderzoeken, en je niet-aflatende drive om de patiënt toch echt op nummer één te zetten en te blijven houden. Mariëlle, dank je wel voor je input en de fijne samenwerking. Als theoretisch fysicus (er staat toch echt maar één formule in dit proefschrift!) *hands on* experimenten doen was voor mij nieuw, maar je hebt me de eerste kneepjes van het vak geleerd. Inclusief de noodzakelijke dropjes. Dank je voor je tegengeluid dat soms nodig was en je commentaar op mijn stukjes ('kan het wat minder wollig?'). Ook je peptalks heb ik erg gewaardeerd.

I hereby convey my sincere gratitude to the review committee members and opponents for my defense ceremony: Ben Slotman, Harry Bartelink, Chrit Moonen, Peter Luijten, Remco de Bree, and Anna Kirby. Thank you for your time and effort for participating in the committee and/or being an opponent at my defense ceremony.

Alle *MILANO*-patiënten, die geheel belangeloos aan de studie hebben deelgenomen, ben ik ontzettend dankbaar. Het persoonlijk contact met hen heeft indruk op mij gemaakt en onderstreept voor mij het belang van al het werk op de afdeling.

Een groot deel van mijn onderzoek en daarmee de inhoud van dit proefschrift is te danken aan de vele vrijwilligsters die al die uren voor mij de MRI in gegaan zijn...om er vervolgens vaak met gevoelloze armen en pijnlijke schouders weer uit te komen. Waarvoor excuses! Al zullen de VVV-bonnen vast wat goedgemaakt hebben. Zonder jullie waren de mooie mamma- en okselplaatjes er nooit van gekomen. En denk maar zo: de wetenschap had niet zonder jullie gekund.

De andere (arts-)onderzoekers – Mariska, Danny, Madelijn, Nienke, Debora, Ramona – en andere leden van de mammagroep met wie ik intensief of minder intensief heb samengewerkt en overlegd: met jullie werken was ontzettend leuk! Ramona, je hebt wel wat te verduren gehad als ik weer eens onverwacht binnen kwam stormen (*ik hier?*), en met woordgrappen begon te strooien, of gewoon even kwam praten. Ik heb het altijd gewaardeerd hoe je dingen in een positief licht kunt blijven zien. Binnenkort drinken we er de Draquila op.

Max, een speciale vermelding voor jou mag natuurlijk niet ontbreken. Vanaf het moment dat jij op de afdeling kwam was het hek in feite van de dam, en daar zullen de collega's over mee kunnen praten. Het hoogte- of dieptepunt was toch wel de ESTRO in Barcelona. De humor, alle Jiskefet-citaten, de vele woordgrappen, knatsmomenten, maar ook vele goede gesprekken heb ik erg gewaardeerd. Ik beschouw je niet voor niets als goede vriend. Zo ken ik je weer. Mocht je ooit hulp met e-machten nodig hebben...

Thanks to my office mates and all other PhD students – many of whom I consider to be friends! You were virtually all victims of my jokes and ever-repeating puns, for which I was and still am very thankful. In non-specific order: Markus (ni!), Charis (we should *definitely* play Battlefield), Jean-Paul (Koning Kantoornumor en plaatsvervangend secretaresse), Stan (baas!), Matteo (ciao bello, grazie mille for proofreading the first drafts), Bjorn, Michaela, Maxence (dr. Borot de Battisti sends his regards), Ellis, Tim, Tom, Christel, Alie, Kimmy, Frank (F.A. Stoett himself), Mariska, Dennis, Mette, Hans, Filipa, Soraya, Robin, Joris, Sophie, and Joana. The moments we shared during conferences, parties, Australia/USA road trips, lunch breaks, coffee talks, squash sessions, beer occasions, ImagO nights out, OiO-uitjes, etc., have been truly invaluable. *Koffie?*

Uiteraard ook alle andere (arts-)onderzoekers op de gang en aan de andere kant van het Q-gebouw, en van de 7 T, met jullie heb ik het altijd erg gezellig gehad! Hetzelfde geldt voor de ImagO-leden met wie ik samen een paar jaar lang succesvol (?) de ImagO-dagen en –middagen heb georganiseerd. De overleggen met jullie waren een leuke afwisseling van ons toch vaak zware bestaan als onderzoekers!

Aan iedereen op de afdeling Radiotherapie die ik heb leren kennen, en met wie ik heb samengewerkt: dank voor de hulp, uitleg, input, steun, koffiepraat, en de lol tijdens dagjes uit, zeilweekenden, uit de hand gelopen (kerst) borrels, en gezellige/productieve congressen. Ik bedoel hiermee natuurlijk ook de secretaresses, ICT'ers (Erwin – mag ik daar een bordje bij?), artsen, technici, klinisch fysici, dames van de administratie, unithoofden, stafleden en natuurlijk de laboranten. De MRI-laboranten – onder aanvoering van Ellart en Tuan – met jullie heb ik altijd geweldig samengewerkt. Bedankt voor al jullie hulp! Ook dank aan Shanta van ons trialbureau: dankzij onze vele (gezellige) overleggen heb ik de hele papierwinkel rondom de studie mooi op orde gekregen en liep het als een trein. De medewerkers van de andere afdelingen die betrokken waren bij mijn onderzoek, en alle co-auteurs van de artikelen en abstracts (in het bijzonder Ruud Pijnappel, Stephanie de Waard, Lenny Verkooijen, en Arjen Witkamp) ben ik erg dankbaar. Dit geldt zeker voor Marianne Deelen, Anne Kuijer, Thijs van Dalen, researchverpleegkundigen en alle andere betrokkenen, in het Diaconessenhuis. Dankzij jullie is de *MILANO* in recordtempo vol geraakt! Wie niet mag ontbreken is Eveline Alberts: je hebt ons echt verder geholpen richting de MRI-linac. Ik heb veel van je geleerd, op gebied van MRI, maar ook mijn Twents vocabulair is uitgebreid.

Ik had de afgelopen jaren nooit volgehouden zonder de wekelijkse nerd-lunches met Pim, Ronald en Marcel. Lunch, koffie, bijpraten, woordgrappen en gaan. Oftewel, snor baard bril alles. Ook de battle blob-sessies met speciaalbier en/of whisky zijn voor mij onvergetelijk geweest en ik ben ervan overtuigd dat we die er nog wel even inhouden... *Is that a whale?* Dit geldt natuurlijk ook voor de legendarische Derrick-avondjes, Saboteur-potjes en epische NGL-weekenden, met alle andere natuurkundenerds (Harry, Jerfey, Vincent, Martijn, Marco, Stefanie, Joost, Bart, Floor, Hans), waar ik ontzettend van heb genoten.

To my former house mates at Lange Nieuwstraat 72-76 and all regulars there: the three years with you were awesome!

Simon, bedankt voor je vele uren werk, geduld en zeer professionele input voor het design en drukken van dit proefschrift. Het is fantastisch geworden.

Andere mensen die mij gesteund hebben, en die het proces van Tristan de student naar Tristan de serieuze onderzoeker (!?) van dichtbij meegemaakt hebben zijn er eigenlijk te veel om op te noemen. Toch noem ik een aantal van jullie specifiek: Ypma, Jochem, Sergino, Tom, Jesse, Jeroen, Iris, Elmer, en natuurlijk al jullie consorten. Vaak al sinds de middelbare school zijn jullie vrienden met wie ik vele mooie momenten, goede gesprekken, pokersessies, reizen, spellen, feestjes en geweldige avonden heb meegemaakt. Ik waardeer jullie vriendschappen enorm.

Lidwien, ik kan wel zeggen dat ik door je pianolessen gegroeid ben, als musicus en als persoon. Ik ben heel blij dat we nog een paar jaar samen door kunnen! En wie weet ontdek ik nog wel wat mooie muziek als ik in de scanner lig.

Michelle, je kent me als bijna geen ander en bent er altijd voor me geweest. Ik vind het daarom geweldig dat je mijn paranimf wil zijn.

Papa, en Olga, dank jullie wel voor jullie hulp vanuit Diessen. Papa, als de professor in de familie, de echte wetenschapper, ben je mijn grote voorbeeld. Je hebt me nooit gedwongen om natuurkunde te gaan doen of te promoveren maar ik heb altijd je steun ervaren in wat ik deed. Ik hoop dat we deze momenten nog vaak samen zullen vieren, onder het genot van een rakkèr blonde of twee.

Mama, jij bent altijd overal bij geweest en je hebt me overal in gesteund, en je was altijd een luisterend oor. Dit heeft mij voor een groot deel gemaakt tot wie ik ben, en mij gebracht waar ik ben. Dank je wel voor alles.

Christiaan, grote broer, waar moet ik beginnen, haha (U mad?). Ik waardeer je gedeelde absurdistische humor, liefde voor lolcats, memes, games, whisky, films, cultuur, science fiction, woordgrappen, en vooral je relativiseringsvermogen, steun en persoonlijke gesprekken, enorm. Het betekent daarom veel voor me dat je mijn paranimf wil zijn.

Lieve oma Gerda, de gesprekken die ik heb gehad met u over mijn onderzoek, dat voor u toch dichtbij komt, hebben veel indruk gemaakt op me. U was altijd in mijn gedachten bij het schrijven van dit proefschrift. Het is voor mij als uw kleinzoon heel bijzonder dat u er op de dag van de verdediging als eregast bij kunt zijn. Ik hoop dat ik u trots heb gemaakt.

Lieve Ana, je hebt bijna twee jaar lang samen met mij de diepe dalen, maar ook de hoge pieken meegemaakt die bij mijn promotie hoorden, en alles daaromheen. Je bent in die tijd bij me geweest om me te steunen en om naar het gezeur te luisteren van deze directe, nuchtere en soms minder nuchtere Hollander, wat voor mij heel erg belangrijk is geweest, en nog steeds is. Je hebt me ongelooflijk veel geholpen, soms door gewoon naar me te luisteren, of door oplossingen te zoeken. Ook al is je Nederlands al heel goed, ik eindig toch in het Portugees (de eerste zin die ik ooit geleerd heb): *Eu acho que nós estamos bem juntos!*

Tristan

In memoriam

Cees van Weerd (26 mei 1931 – 26 maart 2013)

Sara van Heijst-Louwerse (26 januari 1933 – 24 maart 2016)

Addendum

List of publications

Published papers

Tristan C. F. van Heijst, Bram van Asselen, Ruud M. Pijnappel, Marissa Cloos-van Balen, Jan J. W. Lagendijk, H. J. G. Desirée van den Bongard, Marielle E. P. Philippens. *MRI sequences for the detection of individual lymph nodes in regional breast radiotherapy planning*. British Journal of Radiology **89** (2016) 20160072.

Tristan C. F. van Heijst, Marielle E. P. Philippens, Ramona K. Charaghvandi, Mariska D. den Hartogh, Jan J. W. Lagendijk, H. J. G. Desirée van den Bongard, Bram van Asselen. *Quantification of intra-fraction motion in breast radiotherapy using supine magnetic resonance imaging*. Physics in Medicine and Biology, **61** (2016) 1352-1370.

Tristan C. F. van Heijst, Mariska D. den Hartogh, Jan J. W. Lagendijk, H. J. G. Desirée van den Bongard, Bram van Asselen. *MR-guided breast radiotherapy: feasibility and magnetic-field impact on skin dose*. Physics in Medicine and Biology **58** (2013) 6917-5930.

Submitted papers

Tristan C. F. van Heijst, Nienke Hoekstra, Marielle E. P. Philippens, Debora Eschbach-Zandbergen, Jan J. W. Lagendijk, H. J. G. Desirée van den Bongard, Bram van Asselen. *MRI-guided single-fraction boost delivery on individual axillary lymph nodes in breast cancer patients*.

Tristan C. F. van Heijst, Debora Eschbach-Zandbergen*, Nienke Hoekstra*, Bram van Asselen, Jan J. W. Lagendijk, Helena M. Verkooijen, Ruud M. Pijnappel, Stephanie N. de Waard, Arjen J. Witkamp, Thijs van Dalen, H. J. G. Desirée van den Bongard, Marielle E. P. Philippens. *Supine MRI of individual axillary lymph nodes before and after sentinel-node biopsy*.
* Authors contributed equally

Other papers

Jeroen M. Diederix, Tristan C. F. van Heijst, Henk T. C. Stoof. *Ground state of a resonantly interacting Bose gas*. Physical Review A **84** (2011) 3: 033618.

Abstracts and conference proceedings

Tristan C. F. van Heijst, Ellart M. Aalbers, Eveline Alberts, H. J. G. Desirée van den Bongard, Jan J. W. Lagendijk, Bram van Asselen, Marielle E. P. Philippens. *MR imaging of internal mammary lymph nodes and organs at risk in supine breast radiotherapy*. Abstract submitted for ESTRO 36, 2017.

Tristan C. F. van Heijst, H. J. G. Desirée van den Bongard, Nienke Hoekstra, Marielle E. P. Philippens, Marielle E. P. Philippens, Jan J. W. Lagendijk, B. van Asselen. *Lymph node MRI in regional breast radiotherapy leads to smaller target volumes and lower OAR dose*. Abstract submitted for ESTRO 36, 2017.

Tristan C. F. van Heijst, Nienke Hoekstra, Marielle E. P. Philippens, Debora Eschbach-Zandbergen, Jan J. W. Lagendijk, H. J. G. Desirée van den Bongard, Bram van Asselen. *MRI-guided single-fraction boost delivery on individual axillary lymph nodes*. Campus presentation at AAPM Meeting, 2016.

Tristan C. F. van Heijst, Debora Eschbach-Zandbergen, Bram van Asselen, Jan J. W. Lagendijk, M. van Vulpen, Helena M. Verkooijen, Ruud M. Pijnappel, Arjen J. Witkamp, Thijs van Dalen, H. J. G. Desirée van den Bongard, Marielle E. P. Philippens. *Does sentinel-node biopsy affect the use of supine MRI for regional breast radiotherapy?* Electronic poster at ESTRO 35, 2016.

Tristan C. F. van Heijst, N. Hoekstra, Debora Eschbach-Zandbergen, Bram van Asselen, Jan J. W. Lagendijk, M. van Vulpen, Helena M. Verkooijen, Ruud M. Pijnappel, Arjen J. Witkamp, Thijs van Dalen, Marielle E. P. Philippens, H. J. G. Desirée van den Bongard. *Supine MRI for regional breast radiotherapy: Visualization of individual axillary lymph nodes before and after sentinel-node biopsy*. Poster presentation at 14th Bossche Mamma Congress, 2016.

Debora Eschbach-Zandbergen, **Tristan C. F. van Heijst**, Bram van Asselen, Jan J. W. Lagendijk, M. van Vulpen, Helena M. Verkooijen, Ruud M. Pijnappel, Arjen J. Witkamp, Thijs van Dalen, Marielle E. P. Philippens, H. J. G. Desirée van den Bongard. *Does sentinel-node biopsy affect the use of supine MRI for regional radiotherapy in breast cancer patients?* Poster at EBCC-10, 2016.

Tristan C. F. van Heijst, Marielle E. P. Philippens, Mariska D. den Hartogh, Jan J. W. Lagendijk, H. J. G. Desirée van den Bongard, B. van Asselen. *Determining intra-fraction motion in breast radiotherapy using supine cine-MRI*. Poster at 3rd ESTRO Forum, 2015.

Tristan C. F. van Heijst, Bram van Asselen, Jan J. W. Lagendijk, H. J. G. Desirée van den Bongard, Marielle E. P. Philippens. *MRI of individual lymph nodes to guide regional breast radiotherapy*. Oral presentation at AAPM Meeting, 2014.

Tristan C. F. van Heijst, Marielle E. P. Philippens, H. J. G. Desirée van den Bongard, Bram van Asselen, Jan J. W. Lagendijk, Jean-Paul J. E. Kleijnen, Mariska D. den Hartogh. *Quantification of intra-fraction motion of breast tumors using cine-MRI*. Oral presentation at AAPM Meeting, 2014

Tristan C. F. van Heijst, Bram van Asselen, Ruud M. Pijnappel, Jan J. W. Lagendijk, H. J. G. Desirée van den Bongard, Marielle E. P. Philippens. *MRI of individual axillary and supraclavicular lymph nodes for MR-guided regional radiotherapy*. Oral presentation at NVRO Scientific Meeting, 2014.

Tristan C. F. van Heijst, H. J. G. Desirée van den Bongard, Jan J. W. Lagendijk, Bram van Asselen, Marielle E. P. Philippens. *MRI of individual axillary and periclavicular lymph nodes for MR-guided regional radiotherapy*. Electronic poster at ESTRO 33, 2014.

Tristan C. F. van Heijst, Bram van Asselen, Marissa van Balen, Bas W. Raaymakers, Gijsbert H. Bol, Jan J. W. Lagendijk, Marco van Vulpen, H. J. G. Desirée van den Bongard, Marielle E. P. Philippens. *Development of MRI-guided stereotactic radiotherapy of the axillary and periclavicular lymph nodes*. Oral presentation at 17th ICCR, 2013.

Tristan C. F. van Heijst, Mariska D. den Hartogh, Gijsbert H. Bol, Jan J. W. Lagendijk, H. J. G. Desirée van den Bongard, Bram van Asselen. *Magnetic field effects on the skin dose in MRI-guided breast radiotherapy*. Poster at 2nd ESTRO Forum, 2013 – Nominated for best physics poster award.

Miscellaneous

Tristan C. F. van Heijst, H. J. G. Desirée van den Bongard, Jan J. W. Lagendijk, Bram van Asselen, Marielle E. P. Philippens. *MRI of individual axillary and periclavicular lymph nodes for MR-guided regional radiotherapy*. Poster at SONCOS ‘Therapie op Maat’ Conference, 2015 – Best poster award

Tristan C. F. van Heijst. *Research in MRI-guided breast radiotherapy at UMC Utrecht*. Invited talk at Stereotaxiesymposium Lab NL, ARTI, 2014.

Addendum

Curriculum vitae auctoris



Tristan Constantijn Franciscus van Heijst was born in Nieuwegein, The Netherlands, on 23 December 1987. In 2005 he received his gymnasium diploma at Koningin Wilhelmina College in Culemborg, The Netherlands. He followed the bachelor's curriculum *Natuur- en Sterrenkunde* at Universiteit Utrecht, The Netherlands, which he completed with a thesis on *Static black holes and the Schwarzschild solution*. Tristan continued at Universiteit

Utrecht to follow the master programme Theoretical Physics. He conducted his final master research under supervision of Prof. Henk Stoof, which he completed in 2011. The title of his master thesis was *An HNC approximation to strongly interacting ultracold Bose gases*. In 2012, Tristan started his PhD at University Medical Center Utrecht, under supervision of Prof. Jan Lagendijk, Dr. Bram van Asselen, and Dr. Desirée van den Bongard. His research, the results of which are described in this thesis, focuses on MRI-guided radiotherapy for breast cancer patients on the MRI linear accelerator.

